**FACULTY
OF MATHEMATICS
AND PHYSICS**
Charles University

DOCTORAL THESIS

Helena Švihlová

Flow of biological fluids in patient specific geometries

Mathematical Institute of Charles University

Supervisor of the doctoral thesis: RNDr. Ing. Jaroslav Hron, Ph.D.

Study programme: Physics

Study branch: Mathematical and Computer Modelling

Prague 2017

I declare that I carried out this doctoral thesis independently, and only with the cited sources, literature and other professional sources.

I understand that my work relates to the rights and obligations under the Act No. 121/2000 Sb., the Copyright Act, as amended, in particular the fact that the Charles University has the right to conclude a license agreement on the use of this work as a school work pursuant to Section 60 subsection 1 of the Copyright Act.

In Prague

Helena Švihlová

Title: Flow of biological fluids in patient specific geometries.

Author: Helena Švihlová

Institute: Mathematical Institute of Charles University

Supervisor: RNDr. Ing. Jaroslav Hron, Ph.D., Mathematical Institute of Charles University

Abstract: Time-dependent and three-dimensional flow of Newtonian fluid is studied in context of two biomechanical applications, flow in cerebral aneurysms and flow in stenotic valves.
In the first part of the thesis, the computational meshes obtained from the medical imaging techniques are used for the computation of hemodynamic parameters associated with the rupture potency of the cerebral aneurysms. The main result is the computation within twenty geometries of aneurysms. It is shown that the aneurysm size has more important role in wall shear stress distribution than the fact whether the aneurysm is ruptured or unruptured.
The second part of the thesis is addressed to the flow in stenotic valves. It is shown that the method currently used in medical practice is based on assumptions which are too restrictive to be apply to blood flow in the real case. The full continuum mechanics model is presented with physiologically relevant boundary conditions and it is shown that results are consistent with measured data obtained from literature.
Then we focus on the obtaining the pressure field from the velocity field. The presented method provides more accurate pressure approximation than commonly used Pressure Poisson Equation. The last chapter of the thesis is dedicated to Nitsche's method for treating slip boundary condition. The numerical results are presented in comparison to the flow with no-slip boundary condition and the differences are significant.

Keywords: Patient specific geometries, Cerebral aneurysm, Stenotic valve, Pressure Poisson Equation, Nitsche's method.

Acknowledgment

I would like to express my deepest gratitude to the following people.

At the first place, my special thanks go to my supervisor, Dr. Jaroslav Hron, for the support and encouragement in all my studies. He had always answers for any questions and this thesis would never exist without him.

I greatly appreciate the opportunity to work with many inspiring people. I am grateful to Prof. Josef Málek for motivation and directions and I am specially grateful for all corrections addressed to the articles and the thesis. I would like to express my thanks to Prof. Rajagopal and Dr. Rajagopal to expand my horizons. This thesis would not start without Dr. Aleš Hejčl, whose optimism is contagious. I would like to thank Dr. Alena Sejkorová for the time spent on the mesh generation. My thanks are also addressed to the people in the Engineering Department at Mayo Clinic, especially Dr. Dan Dragomir-Daescu for correcting articles and Dr. Dennis Kendall for patience in software explanation.

I am also grateful for time spent with great people in the group of Mathematical modeling in the Mathematical Institute of Charles University.

Na tomto místě chci speciálně poděkovat svojí mamince Radmile Matěnové za její bezednou podporu a radost nad každým dílčím úspěchem v celém mém studiu.

Chci poděkovat svému životnímu partnerovi Petru Beilnerovi za to, že mě donutil dopsat dizertaci, a za největší dar mého života.

Contents

2

Abbreviations and notation

Abbreviations

CFD	computational fluid dynamics
HR	heart rate
AV	aortic valve
FSI	fluid structure interaction
ALE	arbitrary Lagrangian-Eulerian
NS	Navier-Stokes
CT	computed tomography
MR	magnetic resonance
wss	wall shear stress vector
WSS	wall shear stress (wall shear stress vector magnitude)
WSSG	gradient of wall shear stress vector
OSI	oscillatory shear index
RRT	relative residence time
P-	peak values
TA-	time averaged values (over a cardiac cycle)
AR	aspect ratio
EL	energy loss
PLc	pressure loss coefficient
LSA	low shear area
ICI	inflow concentration index
SCI	shear concentration index
VDR	viscous dissipation ratio
AS	aortic stenosis
AVA	aortic valve area
LV	left ventricle
SET, SEP	systolic ejection time, systolic ejection period
CO	cardiac output
r	correlation coefficient
SEE	standard error in estimation
SV	stroke volume
F	flow rate
PPE	Pressure Poisson Equation
STE	Stokes Equation

Abbreviations used for the main arteries in Willis circle are provided in Tab. 1.1.

Notation

$\mathbf{v}$	velocity
p	pressure
T	Cauchy stress tensor
$\mathbf{n}$	unit outer vector normal to the boundary
$\mathsf{T}\mathbf{n}$	surface-traction vector
t	time
T	maximal computational time
Ω	bounded fixed computational domain in $\mathcal{R}^3$
$\mathcal{R}^3$	three-dimensional Euclidean Space
$\partial\Omega$	boundary of the computational domain
$\Gamma_{in}, \Gamma_{out}, \Gamma_{wall}$	parts of the boundary
ρ_*	constant density
μ_*	constant dynamic viscosity
ν_*	constant kinematic viscosity
$\overline{V(t)}$	magnitude of the inlet velocity averaged over the inlet plane
$\overline{P(t)}$	prescribed pressure averaged over the otlet plane
D	symmetric part of the velocity gradient
$\mathbf{v}_{test}, p_{test}$	test functions
V, P	function spaces for the velocity and the pressure
V_h, P_h	discrete approximations of V, P spaces
$\mathbf{v}_h, p_h$	discrete approximations of functions $\mathbf{v}, p$
$\mathbf{v}_h^{test}, p_h^{test}$	discrete approximations of test functions $\mathbf{v}_{test}, p_{test}$

$C(\Omega)$	space of continuous functions on Ω
$\left[C(\Omega)\right]^3$	space of continuous vector functions on Ω
$L^2(\Omega), L^2(\partial\Omega)$	Lebesgue spaces
$\left[\mathrm{H}^1(\Omega)\right]^3$	Sobolev space $\mathrm{W}^{1,2}(\Omega)$ of vector functions on Ω
$(f, g)_\Omega$	scalar product in $L^2(\Omega)$; $f, g \in L^2(\Omega)$
$(f, g)_{\partial\Omega}$	scalar product in $L^2(\partial\Omega)$; $f, g \in L^2(\partial\Omega)$
$(\mathbf{u}, \mathbf{v})_\Omega$	scalar product in $\left[L^2(\Omega)\right]^3$; $\mathbf{u}, \mathbf{v} \in \left[L^2(\Omega)\right]^3$
K, E	tetrahedron, triangle
$P_1(K)$	space of linear functions on K
$P_1^+(K)$	space of linear functions on K with additional bubble function
I	time interval $[0, \mathrm{T}]$
$\mathrm{L}^p(\mathrm{I}, X)$	Bochner space

			vector magnitude or absolute value of the scalar value
g	standard acceleration due to gravity
h	height of fluid appearing in hydrostatic pressure $h\rho g$
$Ek, Edis$	kinetic energy, rate of energy dissipation
Q	flow rate
$\cdot$	scalar product
$\otimes$	dyadic product
p^{drop}	pressure difference $p^{in} - p^{out}$
D	diameter of the valve without stenosis
d	diameter of the stenotic valve
mmHg	millimeters of mercury; $1\,\mathrm{Pa} = 0.0075\,\mathrm{mmHg}$
$(f)_-$	negative part of function f;
	$\qquad (f)_- = f$ while $f < 0$, $(f)_- = 0$ while $f \geq 0$
Γ	cross-sectional area perpendicular to the centerline
L, l	length of the valve; length of the stenotic part of the valve
$\|f\|_{L^2}$	L^2- norm of function $f \in L^2(\Omega)$; $\|f\|_{L^2} = (f,f)_\Omega$
$\|f\|_{H^1}$	H^1- norm of function $f \in H^1(\Omega)$;
	$\qquad \|f\|_{H^1} = (f,f)_\Omega + (\nabla f, \nabla f)_\Omega$

1. Introduction - computational fluid dynamics

Analyzing fluid flow through the computational fluid dynamics has been used in many medical applications. The computational simulations have been performed on different medical topics including heart disease, ventricle function, cerebrovascular diseases, plaque formation in carotid bifurcation, air flow in lungs, artificial organ design and others (Cebral et al., 2010; He, 1996; Qi et al., 2014; Dasi et al., 2009). The problem consists of several parts including the problem definition, definition of the the patient specific geometry through the imaging techniques, problematic of boundary and initial conditions derivation, smooth fine volumetric mesh generation, model description with the proper choice of the numerical method and solver, and finally the visualization of the results and data interpretation. In all these steps one can work with only limited data accuracy and has to be careful to draw any conclusion relevant to medical practice. The thesis focuses on all of these aspects with respect to two applications, the flow in cerebral arteries affected by an aneurysm and the flow in aortic valves affected by a stenosis.

1.1 Heart anatomy and the cardiac cycle

The heart is an organ serving as a pump to the blood circulation. Heart is divided into four chambers, right atrium, right ventricle, left atrium and left ventricle, see Fig. 1.1. Deoxygenated blood goes through the right atrium and ventricle to the pulmonary valve and the lungs. Oxygenated blood goes back to the left atrium and, through the mitral valve, to the left ventricle.

Leaving the heart, blood goes to the ascending aorta and then to the rest of the body. Between all chambers there is a valve, highly deformable viscoelastic body which is opening and closing during a cardiac cycle, namely there is a mitral valve between the left atrium and left ventricle, and an aortic valve between the left ventricle and aorta. The stimulus for the movement is the pressure difference or so called pressure drop. The dependency of their movement on the pressure is described in Fig. 1.2.

The length of cardiac cycle depends on the number of heart beats per minute, it means that for heart rate (HR) 70 beats per minute the length of cardiac cycle can be calculated as $60/70 = 0.86$ s. A cardiac cycle has two phases, systole and diastole. From a left ventricle point of view, there is an ejection phase during the systole (systolic ejection period) and a filling phase during the diastole. The blood pressure in the left ventricle moves between 0 to about 110 mmHg, in contrary to the aorta where minimal pressure is about 75 mmHg. Volume of the blood going from the left ventricle per beat is about 100 ml for men and 85 ml for women (Maceira et al., 2006).
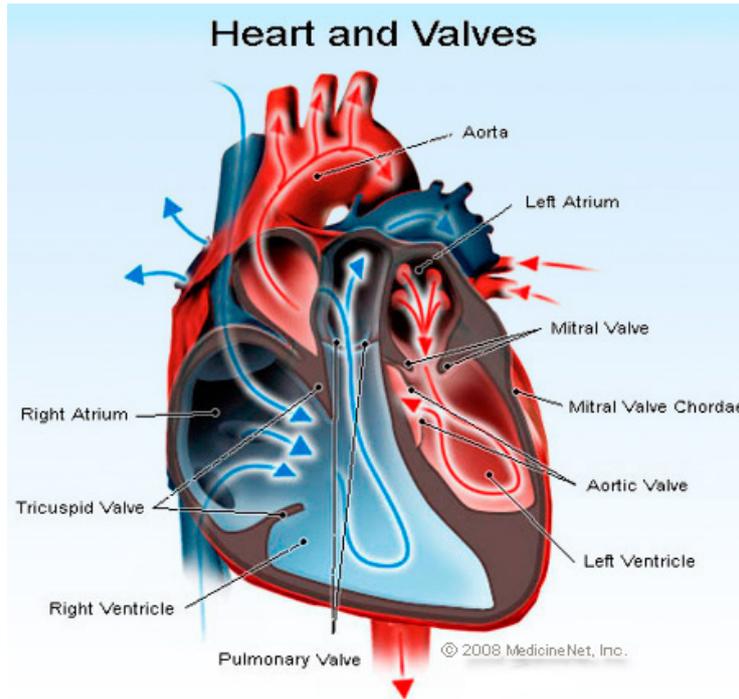
Figure 1.1: Heart. (from (MedicineNet, Inc., 2017))

1.2 Willis Circle

The cerebral aneurysms, pathologic extensions of the brain vessels, typically occur within the arteries of the Circle of Willis. The Willis circle is a system of arteries that sits at the base of the brain, see Fig. 1.3. In this thesis we will use the common abbreviations for arteries in Willis circle. The list of them is provided in Tab. 1.1.

short	name
ACA	anterior cerebral artery
AComA	anterior communicating artery
MCA	middle cerebral artery
OA	ophtalmic artery
ICA	internal carotid artery
PComA	posterior communicating artery
PCA	posterior cerebral artery
BA	basilar artery

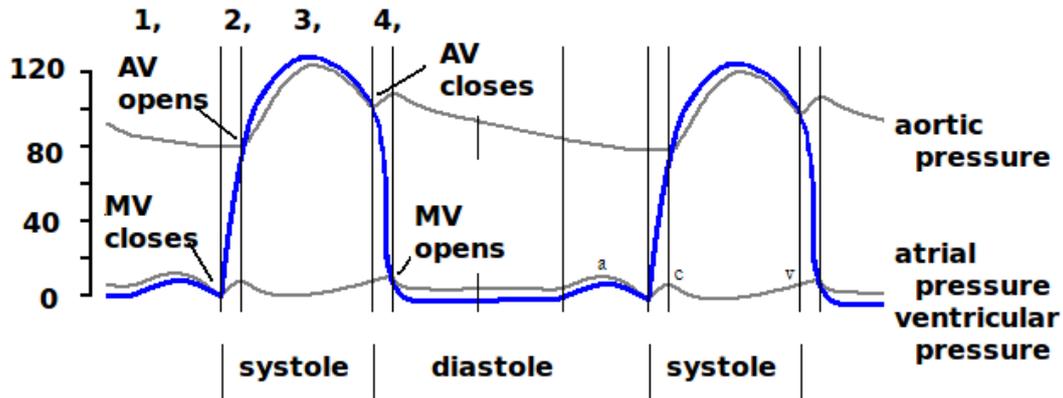Table 1.1: The abbreviations for main arteries in Willis circle.

Figure 1.2: **Blood pressure in the left ventricle during a cardiac cycle.** (from (Wikipedia, 2017a), modified.) **Phase 1,** left ventricle is filled by blood. Mitral valve (MV) is open, aortic valve (AV) is closed. The left ventricular pressure is almost 0. **Phase 2,** the pressure of the left atrium exceeds the left ventricular pressure and mitral valve closes. Aortic valve remains closed. There is isovolumic contraction, when pressure in the left ventricle increases up to exceed the aortic pressure. **Phase 3,** the pressure of the left ventricle exceeds the aortic pressure and aortic valve opens. This phase is called systolic ejection period while volume of the left ventricle blood is decreasing to its minimum value. **Phase 4,** ejecting the blood, left ventricular pressure is decreasing, aortic pressure exceeds the left ventricular pressure and aortic valve closes. This phase is called isovolumic relaxation. There is an increase in aortic valve pressure to ensure the blood would not go back (and down) to the heart.
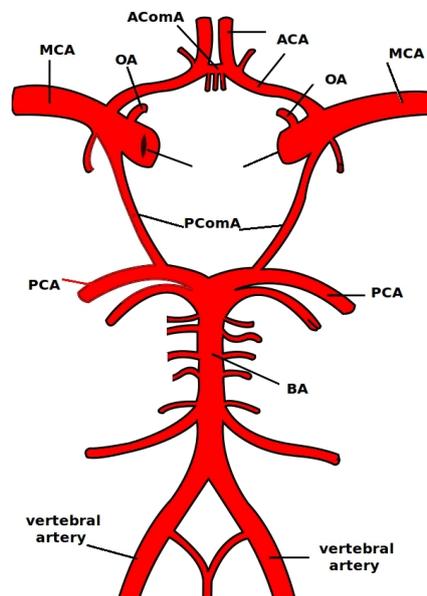

Figure 1.3: Willis circle. (from (Wikipedia, 2017b), modified.)

8

1.3   Structure and the main results of the thesis

The thesis consists of four chapters focusing on four different topics of biomechanical problems applied to the flow in cerebral arteries affected by an aneurysm (chapter 2) and the flow in aortic valves affected by a stenosis (chapters 3-5).

The chapter 2 is based on my research of the blood flow in the cerebral aneurysms with main focus on the patient specific geometries and flow conditions. All data were obtained in cooperation with three institutions: the *Department of Neurosurgery of Masaryk Hospital, J. E. Purkyně University* in Ústí nad Labem in Czech Republic, *International Clinical Research Center, St. Anne's University Hospital* in Brno in Czech Republic and *Division of Engineering, Mayo Clinic* in Rochester in Minnesota, United States. Two original articles, raising from this cooperation, have already been published. There is also a contribution to a CFD benchmark (Berg et al., 2015). The results presented there are used in sections 2.3, 2.4 and 2.5. An article concerning the hemodynamic parameters in ruptured and unruptured MCA aneurysms is to be published. It is modified for the purpose of this thesis and presented in section 2.6.

There are several contributions of this chapter. The process of obtaining computational meshes from medical imaging techniques is presented and the meshes are used for the calculation. The study of two inflow geometry of an ruptured aneurysm is provided showing that the peak values of wall shear stress and normal pressure have the same location for different prescribed ratios between the flow coming through the first and the second input plane. Moreover, this location corresponds to the point of aneurysm rupture. Then the hemodynamic parameters associated with the aneurysm rupture status (whether the aneurysm is unruptured or ruptured) are presented and discussed in context of the computation of the flow in twenty middle cerebral aneurysms. It is shown that the size of the aneurysm has more important role in wall shear stress distribution than the fact whether the aneurysm is ruptured or unruptured. The suggested approach is to compare the flow in volume matched pairs of ruptured and unruptured aneurysms.

The chapters 3 and 4 are based on two original articles presented as a study focusing on the application in cardiovascular mechanics of stenotic aortic valves. The second part of this study concerns on the direct computation of the energy dissipation and pressure loss in the narrowed pipes. The text of the article was modified in chapter 3 to eliminate the medical background and to provide more information about current approaches to the pressure drop and orifice area calculations. The chapter 4 is based on the first part of the study with small modifications. The study of the flow in stenotic aortic valves was prepared in cooperation with *the University of Texas-Houston/Memorial Hermann Texas Medical Center, Center for Advanced Heart Failure* in Houston in Texas, United States and with *Texas A&M University, Department of Mechanical Engineering* in College Station in Texas, United States.

The current methods used for stenosis evaluation (whether this is physiologically relevant or not) are based on comparing the value of the transvalvular pressure difference computed through the simplified Bernoulli equation. The assumptions leading to the conservation of mass, expressed by Bernoulli equation, are presented in chapter 3. Their oversimplification is demonstrated in section 5.3 where the surface integrals, neglected in this approach, are computed next to the values of transvalvular pressure difference and dissipated energy. In opposite to this method, the full time-dependent Newtonian model, using realistic three-dimensional geometry and physiologically relevant boundary conditions, is presented. The numerical quantities are then computed in the valvular geometries with severity up to 80%. The boundary condition preventing the recirculation on the outlet (and consequent numerical instability) is prescribed.

The chapter 4 is devoted to the determination of the pressure data from known (possibly measured) velocity data. Two methods are tested in idealized geometries of aortic stenotic valves with symmetric and non-symmetric obstacle. The verification of the methods on patient-specific geometries is added in section 4.3. The classical Pressure Poisson equation method is numerically compared with the method based on the Helmhholtz decomposition leading to the Stokes equation. This method allow us to compute the pressure under lower regularity requirements on the given velocity and it is shown that it provides more accurate pressure approximation.

The chapter 5 is related to chapter 3 as it concentrates on the same issues considering however slip boundary condition on the wall (instead of no-slip boundary condition considered in chapter 3). We presented the Nitsche's method for three-dimensional Navier-Stokes equations applied on the free (or perfect) slip boundary condition on the walls. The satisfaction of the condition $\mathbf{v} \cdot \mathbf{n}$ on Γ_{wall} is tested and numerical results are provided on the valvular geometries with symmetric stenoses up to 50% severity. The differences between the computations using free-slip and no-slip boundary conditions are remarkable. The other benefit of this chapter is computation of the integrals arising from the Navier-Stokes equations and appearing also in the Bernoulli equation. It is shown that the values of surface integrals, neglected in Bernoulli equation, are comparable next to the values of transvalvular pressure difference and dissipated energy.

Specifically, the thesis incorporates the following articles (parts of abstracts are provided):

1, Berg, et al. (2015): The computational fluid dynamics rupture challenge 2013 phase II: Variability of hemodynamic simulations in two intracranial aneurysms. In: *Journal of Biomechanical Engineering*, 137(12): 121008.
The International CFD Rupture Challenge 2013 seeked to comment on the sensitivity of the various CFD assumptions to predict the rupture by undertaking a comparison of the rupture and blood-flow predictions from a wide range of independent participants utilizing a range of CFD approaches. Twenty-six groups from 15 countries took part in the challenge.

Participants were provided with surface models of two intracranial aneurysms and asked to carry out the corresponding hemodynamics simulations, free to choose their own mesh, solver, and temporal discretization. They were requested to submit velocity and pressure predictions along the centerline and on specified planes. Participants were free to choose boundary conditions in the first phase, whereas they were prescribed in the second phase, described in this paper, but all other CFD modeling parameters were not prescribed.

2, Sejkorová, A., Dennis, K. D., Švihlová, H., Petr, O., Lanzino, G., Hejčl, A., and Dragomir-Daescu, D. (2016): Hemodynamic changes in a middle cerebral artery aneurysm at follow-up times before and after its rupture: a case report and a review of the literature. In: *Neurosurgical Review*, 40(2): 329338.
Hemodynamic parameters play a significant role in the development of cerebral aneurysms. Parameters such as wall shear stress or velocity could change in time and may contribute to aneurysm growth and rupture. However, the hemodynamic changes at the rupture location remain unclear because it is difficult to obtain data prior to rupture. We analyzed a case of a ruptured middle cerebral artery aneurysm for which we acquired imaging data at three time points, including at rupture. Imaging data from two visits before rupture and the 3D DSA images at the moment of aneurysm rerupture were acquired, and CFD simulations were performed.

3, Hejčl, A., Švihlová, H., Radovnický, T., Sejkorová, A., Adámek, D., Hron, J., Dragomir-Daescu, D., and Sameš, M. (2017): Computational fluid dynamics of a fatal ruptured anterior communicating artery aneurysm a case report. Submitted in: *Journal of Neurological Surgery Part A*.
Using CFD to model the hemodynamics in ruptured aneurysms may provide better insight into the rupture risk described by the hemodynamic parameters in light of the real rupture situation. Several studies have assessed the hemodynamic parameters in ruptured aneurysms, such as wall shear stress, flow velocity or flow characteristics. In this report we present the case of a patient operated on for a ruptured anterior communicating artery aneurysm. The CFD parameters were calculated and correlated to the site of the rupture.

4, Švihlová, H., Hron, J., Málek, J., Rajagopal, K. R., and Rajagopal, K. (2016): Determination of pressure data from velocity data with a view toward its application in cardiovascular mechanics. Part 1. Theoretical considerations. In: *International Journal of Engineering Science*, 105:108127.
In this paper we discuss a rigorous new mathematical procedure for the determination of the pressure (mean normal stress) field, from data for the velocity field that can be obtained through imaging procedures such as 4D magnetic resonance imaging or echocardiography. We then use the procedure to demonstrate its efficacy by considering flows in an idealized geometry with a symmetric and asymmetric obstruction. We delineate the superiority of the method with regard to the methods that are currently in place.

5, Švihlová, H., Hron, J., Málek, J., Rajagopal, K. R., and Rajagopal, K. (2017). De-

termination of pressure data from velocity data with a view towards its application in cardiovascular mechanics. Part 2: A study of aortic valve stenosis. In: *International Journal of Engineering Science*, 113:3750.

This paper is Part 2 of a study of blood flow across cardiovascular stenoses. In this Part, existing methods for quantifying stenoses, with specific reference to cardiac valves, are reviewed. Using the mathematically rigorous and physically accurate approach that we developed in Part 1, for a pre-specified flow velocity field proximal to the stenosis and pressure waveform field distal to the stenosis, we ascertain the intro-stenosis and distal flow velocity field, pressure field proximal and within the stenosis, and energy dissipation, all as function of position and time. The computed dissipation, kinetic energy and pressure are then presented in an idealized, but realistic, geometry, with a symmetric stenosis.

1.4 Simplifying assumptions

Several assumptions were taken into account in this thesis, more or less limiting the value of the results. They are listed below.

- The blood is taken as a Newtonian fluid. This can be considered in the case of flow in ascending thoracic aorta (diameter of the vessel about $24\,\mathrm{mm}$, time averaged velocity about $0.5\frac{\mathrm{m}}{\mathrm{s}}$) but it can be problematic in case of cerebral vessels (diameter of the vessel about $3\,\mathrm{mm}$, velocity about $0.5\frac{\mathrm{m}}{\mathrm{s}}$) or in case of stenotic valves (diameter of the 80% stenotic valve about $5.4\,\mathrm{mm}$, velocity up to $3\frac{\mathrm{m}}{\mathrm{s}}$).

  The presence of the Fahraeus-Lindqvist phenomenon (a decrease of the blood viscosity flowing through the capillaries) was verified in tubes of lower than $0.2\,\mathrm{mm}$ diameter. In two cases used in the thesis the ratio between the diameter of the red blood cell ($8\,\mu\mathrm{m}$) and the vessel diameters are about $0.3\cdot10^{-3}$ for healthy aortic valve and $1.5\cdot10^{-3}$ for 80% stenotic valve, and $2.7\cdot10^{-3}$ for cerebral vessel, so the diameter of the vessel should be high enough for this critical case. On the other hand, even a fluid showing Newtonian characteristics at changing shear rates but exhibiting increasing normal stress at increasing shear rate - even Newton-like plasma can exhibit normal stress differences (Dintenfass, 1985).

  Moreover, it was shown that Newtonian model underestimated blebs (an irregular bulge of aneurysm, see Fig. 2.1)) in comparison with Carreau viscosity model (Hippelheuser et al., 2014), more specifically blebs presence moves the wall shear stress histograms to the left. This was significant for non-Newtonian case but not in Newtonian case.

  The Newtonian fluid assumption may also underestimate the viscosity and overestimate WSS in regions of stasis, as was shown in comparison with Casson and

Herschel-Bulkley models (Xiang et al., 2011).

To the flow in the aorta (diameter of the vessel about $24\,\text{mm}$, time averaged velocity about $0.5\,\frac{\text{m}}{\text{s}}$), it was shown that overall velocity distributions and wall pressure distributions were similar in comparison with Casson model. On the other hand, the Newtonian model underestimated the wall shear stress values up to $8.121\,\text{Pa} \sim 0.061\,\text{mmHg}$ (Kumar et al., 2017) .

- The vessel walls were considered rigid in the thesis which is probably the most limiting assumption, especially for the modelling flow in aortic valves.

There are several studies concerning the fluid structure interaction (FSI) with hemodynamic applications and using the different approaches, i.e. Arbitrary Lagrangian-Eulerian (ALE) formulation with monolithic coupling approach (Mádlík, 2010) or with monolithic geometric multigrid solver (Richter, 2015). The FSI was computed in the 3D model of patient-specific aorta and in the 3D model representing abdominal aortic aneurysm in (Bertoglio, 2012) using the 3D-0D coupling on the outlets.

Aneurysm growth was neglected in this study, as the plaque growth in the stenotic valves. Both problems, interaction with the solid tissue and its growth, are more demanding for the computational time and efficient numerical methods. There is also a difficulty concerned to getting proper wall parameters.

- Only mechanical properties of the flow are considered, possible effects of the chemical and electrical properties are neglected. However, the blood flow exhibits also the thermal, and even the optical properties (Woodcock, 1976).

- Other limitations are related to wall compliance in patient-specific geometries and to the fact that small vessels are neglected, to outflow conditions used in chapter 2 (stress free) and to the limiting accuracy of the measurements of boundary conditions.

- Finally, the inflow and outflow conditions are simplified to Dirichlet or Neumann boundary conditions. The blood passes through the circulatory system and the choice of proper boundary conditions can be modeled by another technique such as 3D-0D coupling. However, there is a problem to identify proper coupling parameters in such a case.

2. Flow in patient specific geometries representing cerebral arteries affected by an aneurysm

A cerebral aneurysm can be defined as a local extension of the cerebral vessel, usually expressed by the outpouching. Its rupture can lead to a fatal situation as a stroke and a subanachroid hemorrhage.

With increasing popularity of modern imaging techniques an aneurysm is more often detected. This brings a question whether one can identify the factors leading to the aneurysm rupture.

An estimated 5% of the general population is affected by the cerebral aneurysms but the risk of rupture is only about 1.5-2% per year (Rinkel et al., 1998). On the other hand, in the case of aneurysm rupture, about one quarter of patients die, while roughly half of the survivors live with persistent neurological deficits (Meng et al., 2013).

Aneurysms can be divided according to their location, size, shape and rupture status. An aneurysm is usually formed as an aneurysm sac and a visible neck, see schema in Fig. 2.1. Usually only the arteries located on a Willis circle can be affected, see Fig. 1.3. Aneurysms can be saccular (located in the branching of the vessels) or sidewall (or fusiform). More than 80% of the aneurysms are saccular (Meng et al., 2013).
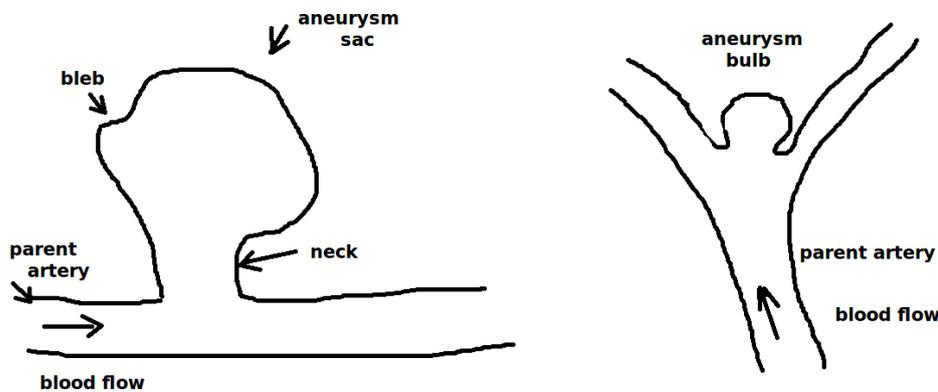

Figure 2.1: The scheme of an aneurysm: The blood goes from the parent artery to the aneurysm. The first picture shows the sidewall aneurysm with a visible neck, the second one shows the saccular aneurysm. The bleb, an irregular bulge, can be presented in both types of aneurysms.

Computational fluid dynamics (CFD) has been gaining increasing interest in the clinical community. The geometry for each case is unique as the flow condition. CFD studies are based on two patient specific inputs. Firstly, the 3D geometry, including the inflow

and outflow blood vessels and the aneurysm itself, and secondly, the inflow and outflow boundary conditions.

This chapter is divided into 7 sections. We briefly recall the process of obtaining the patient-specific geometry, as was described in (Švihlová, 2013). This is done in section 2.1. To see how the flow conditions can be derived from magnetic resonance, one can see i.e. (Rebergen et al., 1993). The numerical model is presented in section 2.2 and the hemodynamic parameters, describing the flow in the aneurysm and thought to be responsible for initiation, growth or rupture of the aneurysm, are described in section 2.3. The method is then applied to a geometry of the ruptured aneurysm with two inflows to describe the hemodynamics near the rupture location, see section 2.5, and to the 20 middle cerebral aneurysms, 10 ruptured and 10 unruptured, to show the hemodynamic parameters dependence on the aneurysm rupture status and volume, see section 2.6. A comparison of the computation with PIV model and other CFD groups, published as a numerical benchmark in (Janiga et al., 2014), is provided in section 2.4. The influence of hemodynamic parameters to the aneurysm rupture status is discussed in section 2.7.

2.1 Computational geometry for patient - specific modeling

Mesh quality has a big influence on an accuracy of the computations for solving partial differential equations. In this section we will briefly describe the process of obtaining computational mesh from the imaging techniques such as computed tomography. For better illustration, the process is shown in Fig. 2.2. We start with a description of getting the voxel representation of data from computer tomography. The process of obtaining smooth surface mesh from the voxel array follows. At the end, volumetric tetrahedral mesh is derived.

From CT scan to voxel segmentation

The result of an imaging technique is a set of 2D slices of pixels with different intensities and resolution in a range about $0.4 - 0.7\,\mathrm{mm}$. Each of them represents one thickness of the whole image. Scanning the brain, big amount of X rays passes through the tissue. Slices show the permeability of the tissue on each pixel expressed by the real number. This number measures the coefficient of the ray weakness passing through the tissue (Jovanović and Jovanović, 2010). A voxel, volumetric element, is a three-dimensional version of the pixel. The voxel resolution is specific for each machine. Voxel resolution is given by resolution of a pixel and by a distance between the slices. By voxel representation of the data we mean a three-dimensional binary array where 1 expresses the tissue presence and 0 expresses the tissue absence in particular voxel.

Defining what part of the CT scan belongs to the final image is not an automatic process. One can pass through each slice and define the region to be segmented. The

program itk-snap was used for the purpose of this work. Itk-snap is a tool for "3D active contour segmentation of anatomical structures" (Yushkevich et al., 2006). The other option is to prescribe the interval of real numbers representing image intensity. However, this process leads to both, to obtain the holes in the image and to add redundant tissue. The relevant image also has to be defined by a person. The advantage of this process is commercial software existence, i.e. Mimics 16.0 (Materialise, Leuven, Belgium). Both ways are challenging and demand the experienced neurosurgeon or neuroradiologist to decide whether the final geometry corresponds to the reality. Small arteries are usually neglected. The geometries used in this work were segmented in Department of Neurosurgery, Masaryk hospital, Ústí nad Labem and Department of Engineering, Mayo hospital, Rochester MN. Both methods and softwares were used.
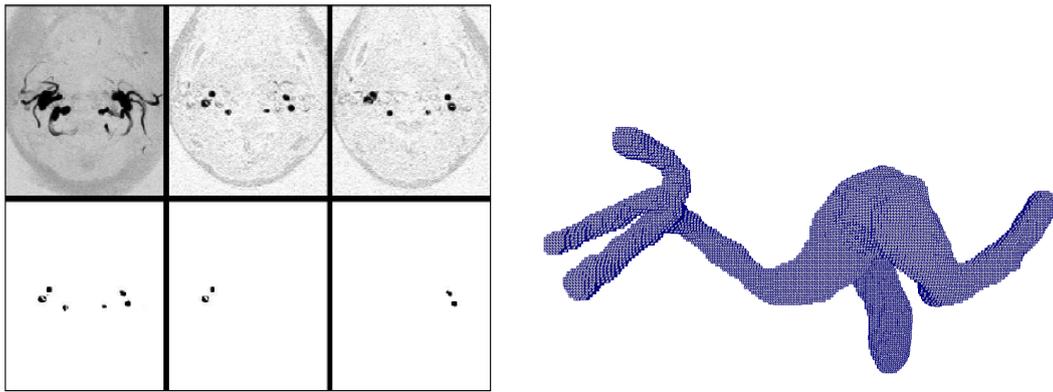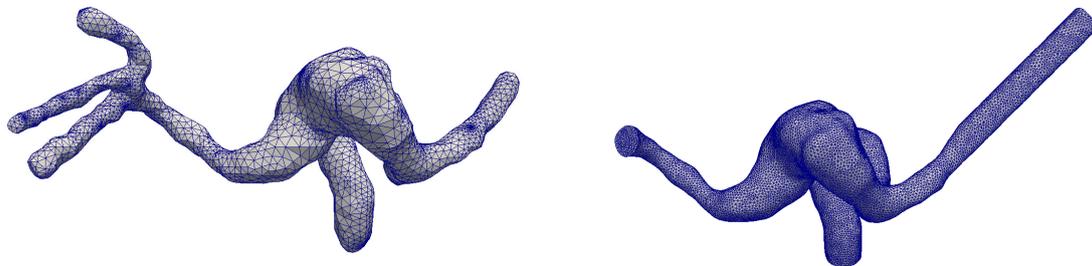

Figure 9: CT image processing.

Figure 2.2: The process of obtaining patient specific geometry includes the CT scan with high resolution, accurate voxel segmentation of the vessel, generating surface mesh and finally smoothing, generating volumetric mesh and prescribing inlets and outlets with possible shortening and elongating of the outputs.

From voxel segmentation to the computational mesh

We will describe the process of obtaining the surface mesh through the isosurface creating as is used in program iso2mesh (Fang and Boas, 2009) based on CGAL library (The CGAL Project, 2016). All meshes used in this chapter were obtained by the process described in the previous section.

An example of voxel segmentation is shown in the second part of Fig. 2.2. Usually, some voxels has to be interactively removed to prevent the surface intersection. Isosurfaces are surfaces with the same level of intensity. That is prescribed through the isovalue, the real number from the interval $[0, 1]$. Each voxel in the segmentation is divided into 6 tetrahedra and created mesh is a base to generating surface mesh. All vertices are numbered according to the number of tetrahedra they belonged to. The numbers are always taken from $[0, 1]$. Then the isosurface is generated according to the prescribed isovalue. For illustration, the schema for two-dimensional array is shown in Fig. 2.3.

Figure 2.3: Schema of isosurface method for two-dimensional array. The isosurface, in two dimensions isocurve, is prescribed by connecting the points with the same value of the intensity. This isovalue must be prescribed, it is 0.5 in this case.

The generated surface mesh must be smoothed. The goals of smoothing meshes for medical computations can be divided into two categories. The first is to visually improved the mesh, to reduce parts with sharp edges and with "stairs". The second category is to preserve the volume and distances in the image. This category also includes the problem of stopping criteria (Bade et al., 2006).

Smoothing filters can be used to improve the mesh. The backward Laplacian filter is used in this work. It is an iterative method. The position of each mesh vertex is

symbol	name	value
ρ_*	density	$1000 \, \frac{\text{kg}}{\text{m}^3}$
μ_*	dynamic viscosity	$3.71.10^{-3} \, \text{Pa} \, \text{s}$
ν_*	kinematic viscosity	$3.71.10^{-6} \, \frac{\text{m}^2}{\text{s}}$

Table 2.1: Constant parameters used in calculation.

recalculated from its current position and the position of its neighbors in each iteration.

The length of the input and output vessels can be prescribed. Finally, the tetrahedral volumetric mesh is computed by Delaunay triangulation. This algorithm is also part of iso2mesh program. The example of final computational mesh is shown in Fig. 2.2.

2.2 Numerical model

Problem formulation

In this section we will compute the fluid flow described by the non-stationary incompressible Navier-Stokes equations in bounded fixed domain $\Omega \subset \mathcal{R}^3$. The domain is derived as was described in previous section.

The boundary of the domain can be divided into the inlet plane, outlet plane/s and walls as $\partial\Omega = \Gamma_{in} \cup \Gamma_{out} \cup \Gamma_{wall}$, $\Gamma_{in} \cap \Gamma_{out} = \emptyset$, $\Gamma_{in} \cap \Gamma_{wall} = \emptyset$, $\Gamma_{wall} \cap \Gamma_{out} = \emptyset$. The vertices and edges which can belong to two of the boundary parts are labeled to belong primarily to the boundaries with prescribed Dirichlet boundary condition.

The problem is formulated as to find the unknowns $(\mathbf{v}, p)$ such that

$$
\begin{aligned}
\rho_* \frac{\partial \mathbf{v}}{\partial t} + \rho_* \left(\nabla \mathbf{v}\right) \mathbf{v} - \operatorname{div} \mathbf{T} &= \mathbf{0} && \text{in } \Omega, \\
\mathbf{T} &= -p\mathbf{I} + \mu_* \left(\nabla \mathbf{v} + \nabla \mathbf{v}^T\right) && \text{in } \Omega, \\
\operatorname{div} \mathbf{v} &= 0 && \text{in } \Omega, \\
\mathbf{v} &= \mathbf{v}_{in} && \text{on } \Gamma_{in}, \\
\mathbf{v} &= \mathbf{0} && \text{on } \Gamma_{wall}, \\
\mathbf{T}\mathbf{n} &= \mathbf{0} && \text{on } \Gamma_{out},
\end{aligned}
\tag{2.1}
$$

where $\mathbf{n}$ is the unit outward normal vector on boundary, $\mathbf{T}$ is a Cauchy stress tensor and μ_* is a constant dynamic viscosity. We will use the subscript $*$ for constants. The list of constants and their values used in all thesis are shown in Tab. 2.1. The initial condition for the problem (2.1) is set to

$$
\begin{aligned}
\mathbf{v}(t = 0) &= \mathbf{0} && \text{in } \Omega; \text{ on } \Gamma_{out} \cup \Gamma_{wall}, \\
\mathbf{v}(t = 0) &= \mathbf{v}_{in}(t = 0) && \text{on } \Gamma_{in}.
\end{aligned}
\tag{2.2}
$$

The Dirichlet boundary condition for velocity is prescribed on the inlet. The function $\mathbf{v}_{in} = \mathbf{v}_{in}(t, \mathbf{X})$ depends on time t and position $\mathbf{X}[x, y, z]$. The parabolic profile is prescribed

to be consistent with no-slip boundary condition. In three-dimensional case the parabolic profile can be described as

$$\mathbf{v}_{in}(t, \mathbf{X}) = -2\overline{V(t)}\mathbf{v}(\mathbf{X})\mathbf{n}; \qquad \mathbf{v}(\mathbf{X}) = \frac{r^2 - |\mathbf{CX}|^2}{r^2} \tag{2.3}$$

where $\overline{V(t)}$ is a function depended only on time, r is a radius of circular inlet and $\mathbf{C}[c_x, c_y, c_z]$ is its centerpoint. $\overline{V(t)}$ is the magnitude of the inlet velocity averaged over the inlet plane. The no-slip condition is prescribed as Dirichlet boundary condition on the walls. As we do not have any information of the pressure, we prescribe the traction free condition, imposed as a Neumann boundary condition, on the outlet/s.

Defining the inlet condition on the patient-specific geometry, one cannot assume that the inlet would be circular. There are several possibilities how to deal with this, we will mention three of them. The first one is to extend the inlet part and end it with the circular plane. This option is used in section 2.6 to get the circular inlet for Womersley profile. The second option is to prescribe the condition directly on the input polygon M, define the centerpoint $\mathbf{C}$ of all its vertices and then prescribe the profile as

$$\mathbf{v}(\mathbf{X}) \approx \left(1 - \frac{|\mathbf{CX}|}{|\mathbf{CY}|}\right)^2, \tag{2.4}$$

where $\mathbf{Y} \in \partial M \cap \overrightarrow{\mathbf{CX}}$.
The third option is to use the following equation for the input polygon M;

$$\mathbf{v}(\mathbf{X}) \approx \frac{\max\left(r^2 - |\mathbf{CX}|, 0\right)}{r^2}, \tag{2.5}$$

where $r = \min_{\mathbf{A} \in \partial M} |\mathbf{CA}|$. This approach can be applied when the assumption of the almost circular inlet plane is satisfied. This option is used in section 2.5 for parabolic profile.

Weak formulation

Multiplying the eq. (2.1) by the test functions $\mathbf{v}_{test}$ and integrating over the domain Ω and over the finite time interval $[0, \text{T}]$ we get

$$\int_0^T \left[\rho_* \left(\frac{\partial \mathbf{v}}{\partial t}, \mathbf{v}_{test}\right)_\Omega + \rho_* \left((\nabla \mathbf{v}) \mathbf{v}, \mathbf{v}_{test}\right)_\Omega - (\text{div } \mathbf{T}, \mathbf{v}_{test})_\Omega\right] dt = 0. \tag{2.6}$$

The choice of function spaces in the weak formulation can be

$$V := \left\{\mathbf{v} \in \text{L}^\infty\left(\text{I}, \left[\text{H}^1(\Omega)\right]^3\right); \quad \mathbf{v} = \mathbf{0} \text{ on } \Gamma_{in} \cup \Gamma_{wall}\right\}, \tag{2.7}$$

$$P := \left\{p \in \text{L}^2\left(\text{I}, \text{L}^2(\Omega)\right)\right\} \tag{2.8}$$

where $L^\infty \left(I, \left[H^1(\Omega) \right]^3 \right)$ and $L^2 \left(I, L^2(\Omega) \right)$ are Bochner spaces. For more details about the choice of function spaces one can see standard book on numerical analysis as (Ciarlet, 2002).

Multiplying the eq. $(2.1)_3$ by the test functions p_{test}, using the per-partes method for eq. (2.6) and imposing the boundary conditions we get the weak formulation of the problem (2.1). For simplicity we will identify $\mathbf{v}$ with its part having homogeneous Dirichlet boundary condition on Γ_{in}, namely $\mathbf{v} := \mathbf{v} - \mathbf{v}_{in} \in V$. Then the weak formulation can be formulated as follows.

Find $(\mathbf{v}, p)$ in $V \times P$ satisfying for all $(\mathbf{v}_{test}, p_{test}) \in V \times P$:

$$
\int_0^T \left[\rho_* \left(\frac{\partial \mathbf{v}}{\partial t}, \mathbf{v}_{test} \right)_\Omega + \rho_* \left((\nabla \mathbf{v}) \mathbf{v}, \mathbf{v}_{test} \right)_\Omega + (\mathbf{T}, \nabla \mathbf{v}_{test})_\Omega \right] dt = 0,
$$
$$
- \int_0^T (\operatorname{div} \mathbf{v}, p_{test})_\Omega \, dt = 0
$$

$$(2.9)$$

while surface integral $(\mathbf{T}\mathbf{n}, \mathbf{v}_{test})_{\partial\Omega} = 0$ due to the $\mathbf{v}_{test} \in V$ from eq. (2.7) and due to the boundary condition $(2.1)_6$.

In following, we will approximate eq. (2.9) with the finite element method and treated the time derivation by the Crank-Nicholson time discretization scheme.

Finite element method discretization

Let us for simplicity assume that the domain Ω is given as a union of tetrahedra forming regular tetrahedralization.

The finite element used in sections 2.4 and 2.5 will be the MINI element. It was introduced for mixed formulation of the Stokes problem in (Arnold et al., 1984). The element uses the continuous P_1 approximation for the pressure and the continuous approximation for the velocity described as a P_1^+, namely

$$
\mathbf{v}_h, \mathbf{v}_h^{test} \in V_h := \left\{ \mathbf{v}_h \in \left[C(\Omega) \right]^3, \, \mathbf{v}_h \mid_K \in \left[P_1^+(K) \right]^3 \forall K \in \Omega; \, \mathbf{v}_h \mid_E = \mathbf{0} \, \forall E \in \Gamma_{in} \right\},
$$
$$
p_h, p_h^{test} \in P_h := \left\{ p_h \in C(\Omega), \, p_h \mid_K \in P_1(K) \quad \forall K \in \Omega \right\}
$$

$$(2.10)$$

and

$$
\left[P_1^+(K) \right]^3 := \left[P_1(K) + B_4(K) \right]^3.
$$

$$(2.11)$$

A local degree of the bubble function $\left[B_4(K) \right]^3$ is represented by a function value in the centerpoint of the tetrahedron. Local degrees of freedom for MINI element are shown in Fig. 2.4, their number is 19, 5 for each velocity component and 4 for pressure.
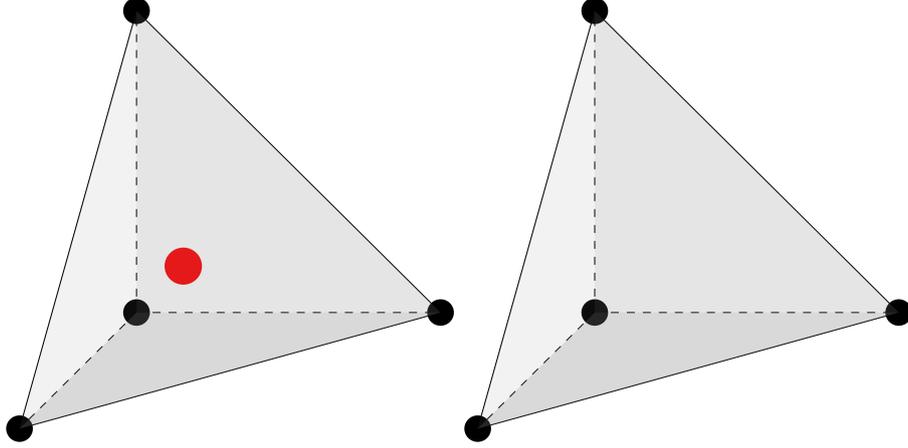
Figure 2.4: The local degrees of freedom for velocity and pressure in finite element MINI.

The finite element discretization of eq. (2.9) leads to the following formulation:
Find $(\mathbf{v}_h, p_h) \in V_h \times P_h$ such that for all $(\mathbf{v}_h^{test}, p_h^{test}) \in V_h \times P_h$ holds

$$\int_0^T \left[\rho_* \left(\frac{\partial \mathbf{v}_h}{\partial t}, \mathbf{v}_h^{test} \right)_\Omega + L(\mathbf{v}_h, p_h, \mathbf{v}_h^{test}, p_h^{test}) \right] dt = 0 \tag{2.12}$$

where

$$L(\mathbf{v}_h, p_h, \mathbf{v}_h^{test}, p_h^{test}) = \rho_* \left((\nabla \mathbf{v}_h) \mathbf{v}_h, \mathbf{v}_h^{test} \right)_\Omega + \left(\mathbf{T}_h, \nabla \mathbf{v}_h^{test} \right)_\Omega - \left(\operatorname{div} \mathbf{v}_h, p_h^{test} \right)_\Omega \tag{2.13}$$

and

$$\mathbf{T}_h = -p_h \mathbf{I} + \mu_* \left(\nabla \mathbf{v}_h + \nabla \mathbf{v}_h^T \right). \tag{2.14}$$

Time discretization

To discretize the formula (2.12) we will divide time interval $[0, T]$ into the time steps $[t_k, t_{k+1}]$, $k \in [0, N-1]$ of a length d_k and get

$$\sum_{k=0}^{N-1} \int_{t_k}^{t_{k+1}} \rho_* \left(\frac{\partial \mathbf{v}_h}{\partial t}, \mathbf{v}_h^{test} \right)_\Omega dt + \sum_{k=0}^{N-1} \int_{t_k}^{t_{k+1}} L(t) \, dt = 0 \tag{2.15}$$

using notation

$$L(t) := L(\mathbf{v}_h(t), p_h(t), \mathbf{v}_h^{test}(t), p_h^{test}(t)). \tag{2.16}$$

Then the approximations

$$\int_{t_k}^{t_{k+1}} f(t)\, dt \approx d_k \frac{f(t_{k+1}) + f(t_k)}{2}, \tag{2.17}$$

$$\frac{\partial f}{\partial t} \approx \frac{f(t_{k+1}) - f(t_k)}{d_k}, \tag{2.18}$$

$$\int_{t_k}^{t_{k+1}} \frac{\partial f(t)}{\partial t}\, dt \approx f(t_{k+1}) - f(t_k) \tag{2.19}$$

lead to the classical Crank-Nicholson time stepping scheme: Find $(\mathbf{v}_h, p_h) \in V_h \times P_h$ such that

$$\sum_{k=0}^{N-1} \rho_* \left(\mathbf{v}_h(t_{k+1}) - \mathbf{v}_h(t_k), \mathbf{v}_h^{\text{test}} \right)_\Omega + \sum_{k=0}^{N-1} d_k \frac{L(t_{k+1}) + L(t_k)}{2} = 0 \tag{2.20}$$

holds for all $(\mathbf{v}_h^{test}, p_h^{test}) \in V_h \times P_h$, with respect to definitions (2.13) and (2.16).

2.3 Hemodynamic parameters

Recent studies showed that hemodynamics in cerebral aneurysms can be considered as one of the leading factors of aneurysm rupture (Shojima et al., 2004), (Jou et al., 2008), (Metaxa et al., 2009), (Qian et al., 2011). Nowadays neurosurgeons assesses the potential rupture risk according to the morphological factors as size, shape and localization of the aneurysm (Sejkorová et al., 2016).

As the morphological parameters should describe the shape of the aneurysm, the hemodynamic parameters should describe the flow inside the aneurysm. However, computational fluid dynamics was criticized for the amount of hemodynamic parameters suggested to be responsible to the initiation, growth or rupture of the aneurysms although some of them were correlated with the rupture status in relatively big amount of cases ((Mut et al., 2014) on 210 cases, (Miura et al., 2012) on 106 cases).

The hemodynamic factors, studied in recent papers, are mostly flow patterns, their complexity and number of vortices inside the aneurysm, wall shear stress (WSS) and the oscillatory shear index (OSI) which can capture the WSS oscillations during a cardiac cycle. The most popular hemodynamic parameter is WSS because it can express the changes in the flow near the wall by one or two numbers. But larger aneurysms are associated with lower WSS regardless the rupture status, see (Lauric et al., 2013). Since this fact can lead to many misunderstandings, recent studies are focused usually on one location in the brain and, most importantly, on the similar size of the aneurysms (Chien et al., 2009).

In this section we will derive the formulas for three commonly used hemodynamic parameters related to the problematic of the cerebral aneurysms, namely WSS, OSI and relative residence time (RRT). Then we will summarize the morphological and hemodynamical parameters which were used in recent studies and which are thought to have

an influence to the aneurysm formation. The discussion of their influence, based on the study of 10 ruptured and 10 unruptured middle cerebral aneurysms, will be provided in section 2.7.

Wall shear stress

Wall shear stress is defined as a magnitude of the stress vector projected to the tangential plane.

Cauchy's theorem(text taken from (Gurtin, 1982)): *Let* $\mathbf{s}$ *be a surface force for the body during a motion. Then a necessary and sufficient condition that the momentum balance laws be satisfied is that there exist a spatial tensor field* T *(called the Cauchy stress) such that for each unit vector* $\mathbf{n}$,

$$\mathbf{s(n)} = \mathsf{T}\mathbf{n}. \tag{2.21}$$

In this text we will use the notation $\mathsf{T}\mathbf{n}$ for a surface-traction vector. The tangential part of this vector, $\mathbf{wss}$, is derived as

$$\mathbf{wss} = \mathsf{T}\mathbf{n} - [\mathsf{T}\mathbf{n} \cdot \mathbf{n}]\,\mathbf{n}. \tag{2.22}$$

As a hemodynamic factor, usually only its magnitude, denoted here WSS, is used. For the Newtonian fluid and Cauchy stress tensor of the type $(2.1)_2$ we have

$$\mathsf{T}\mathbf{n} = -p\mathbf{n} + \mu_*(\nabla \mathbf{v} + (\nabla \mathbf{v})^T)\mathbf{n}$$

$$\mathbf{wss} = -p\mathbf{n} + \mu_*(\nabla \mathbf{v} + (\nabla \mathbf{v})^T)\mathbf{n} - \left(-p\mathbf{n} + \mu_* \left[(\nabla \mathbf{v} + (\nabla \mathbf{v})^T)\mathbf{n} \cdot \mathbf{n}\right]\mathbf{n}\right)$$

and the WSS is expressed as a magnitude of

$$\mathbf{wss} = \mu_* \left((\nabla \mathbf{v})\mathbf{n} + (\nabla \mathbf{v})^T\mathbf{n}\right) - \mu_* \left[(\nabla \mathbf{v} + (\nabla \mathbf{v})^T)\mathbf{n} \cdot \mathbf{n}\right]\mathbf{n}. \tag{2.23}$$

Usually, the time averaged WSS is also computed through

$$\text{TAWSS} = \frac{1}{\mathrm{T}} \int_0^T \text{WSS}\, dt \tag{2.24}$$

where T is a length of a cardiac cycle.

(Ku et al., 1985) observed that the highest WSS was connected to the location where intimal thickening was minimal. Note that intima is an inner part of the arterial wall consisted of a single layer of endothelial cells. This layer can be damaged by high WSS and it can lead to the aneurysm initiation (Metaxa et al., 2009) and rupture (Chien et al., 2009).

Oscillatory shear index

Time changes of the **wss** directions and magnitude during a cardiac cycle can be expressed by an oscillatory shear index. This index was introduced by (He, 1996) as

$$\text{OSI} = \frac{1}{2}\left(1 - \frac{|\int_0^T \mathbf{wss}\, dt|}{\int_0^T |\mathbf{wss}|\, dt}\right). \tag{2.25}$$

(Ku et al., 1985) compared the velocity and **wss** vectors with plaque thickness in atherosclerotic human carotid bifurcation. The data were obtained from histology. They observed that the velocity and **wss** oscillated in both, magnitude and direction, during the systolic phase. They proposed the OSI as a ratio between the specified vector magnitude averaged over the cardiac cycle and **wss** magnitude averaged over the cardiac cycle and find the strong correlation between this OSI and the wall thickness. But the specified vector was introduced differently for different wall parts according to the plaque position. They simplified the definition to eq. (2.25) in (He, 1996).

(Himburg, 2004) observed that endothelial permeability of porcine aortic trifurcation increases slightly with OSI. The study was compared with in vivo measurements in domestic swine.

OSI was computed also in the cerebral aneurysm geometries, i.e. (Liu et al., 2013), (Miura et al., 2012), but they did not show the statistical difference between ruptured and unruptured group.

OSI is thought to be an index correlating with atherosclerotic plaque presence. This is a case of big aneurysms. But stagnation of blood flow can lead to both, destruction of the wall due to increased inflammatory cell infiltration and other pathobiologic responses, and to the stabilization by atherosclerotic remodeling process (Meng et al., 2013).

Relative residence time

The other parameter thought to correlate with atherosclerotic plaque presence is relative residence time (RRT). It represents time that a particle spends in a particular system. With high RRT there is a stagnation of blood flow, especially in aneurysm dome, and there is a space for inflammatory processes and plaque formation. Residence time is a relative concept because moving particles do not stay in any position (Sugiyama et al., 2013).

RRT is proportional to the inverse of Cartesian distance $D(y)$, the distance that a particle near boundary travels during a cardiac cycle, namely

$$\text{RRT} \sim D(y)^{-1}. \tag{2.26}$$

We assume a circular pipe with laminar flow in z direction. Due to symmetry, we can assume that Cartesian distance depends only on y coordinate and the unit vector normal to the boundary near the particle is $\mathbf{n} = (0, 1, 0)$. The velocity is then of a form

$\mathbf{v} = (0, 0, v_z(y))$.

From this form and eq. (2.23) we then have

$$\nabla \mathbf{v} + (\nabla \mathbf{v})^T = \begin{pmatrix} 0 & 0 & 0 \\ 0 & 0 & v_z' \\ 0 & v_z' & 0 \end{pmatrix}, \quad \mathbf{wss} = \mu_* \begin{pmatrix} 0 \\ 0 \\ v_z' \end{pmatrix} = \mu_* \frac{\partial \mathbf{v}(y)}{\partial y}. \tag{2.27}$$

Near the wall we can assume that spatial variation in **wss** can be neglected and Cartesian distance $D(y)$ is then calculated through

$$D(y) = \left| \int_0^T \mathbf{v}(y)\, dt \right| = \left| \int_0^T \frac{y}{\mu_*} \mathbf{wss}\, dt \right| = \frac{Ty}{\mu_*} (1 - 2 \cdot \text{OSI}) \frac{1}{T} \int_0^T \text{WSS}\, dt \tag{2.28}$$

where the eq. (2.25) was used in the last equality.

The standard expression of the RRT is then calculated from eq. (2.26) using the definition (2.24) as

$$\text{RRT} \sim \left[(1 - 2 \cdot \text{OSI})\, \text{TAWSS} \right]^{-1}. \tag{2.29}$$

RRT was computed on 30 cerebral aneurysms, 7 of them with atherosclerotic lesions, in (Sugiyama et al., 2013). They showed the significant relation (P=0.02) between the maximum RRT and atherosclerotic lesion on the intracranial aneurysmal wall.

Another morphological and hemodynamical parameters thought to be involved in aneurysm formation

The morphological parameters should be prescribed to evaluate the size and shape of the aneurysm. The commonly used parameters are size and aspect ratio of the aneurysm, the irregularity of the aneurysm sac and bleb presence. The list of the morphological parameters used in recent studies and their definitions are shown in Tab. 2.2. The meaning of the terms "aneurysm sac", "neck" and "bleb" and the terms "height", "size", "neck diameter" and "convex hull" are shown in Fig. 2.1 and Fig. 2.5, respectively.

Discussing the flow of the aneurysm we try to have a similar set of the hemodynamic parameteres. Next to the WSS, OSI and RRT introduced above, there are several others. Their influence on the aneurysm rupture status was studied in recent papers. They are listed in Tab. 2.3 and discussed in section 2.7.

We will continue with the numerical results using the mesh extraction, numerical model and hemodynamic parameters introduced above. The section 2.4 shows the results in comparison with numerical benchmark and section 2.5 the results using the two inflow study. Finally, there is a study comparing the flow in 10 ruptured and 10 unruptured aneurysms in section 2.6 with discussion of the parameters influence in section 2.7.

parameter	definition
size	maximum distance within the aneurysm
neck diameter	maximum distance in the neck plane
height	maximum perpendicular height of the aneurysm
aneurysm angle	angle between the lines containing neck diameter and maximum height (maximum distance from the centroid of the aneurysm neck to any point on the aneurysm dome)
aspect ratio	height/neck diameter
size ratio	height/average vessel diameter
S, V	surface area and volume of the aneurysm
S_{ch}, V_{ch}	surface area and volume of its convex hull
nonsphericity index	$1 - \frac{S_{hem}(V)}{S}$ - deviation of the aneurysm surface from that of a perfect hemisphere with the same volume
ellipticity index	$1 - \frac{S_{hem}(V_{ch})}{S_{ch}}$
undulation index	$1 - \frac{V}{V_{ch}}$ - captures the degree of surface concavity

Table 2.2: Morphological parameters for evaluating the shape of the aneurysm.

parameter	definition
energy loss	$EL = (p_{in} + \frac{\rho_*}{2}v_{in}^2 + h_{in}\rho_* g) - (p_{out} + \frac{\rho_*}{2}v_{out}^2 + h_{out}\rho_* g)$
pressure loss coefficient	$PLc = \frac{(0.5\rho_* v_{in}^2 + p_{in}) - (0.5\rho_* v_{out}^2 + p_{out})}{0.5\rho_* v_{in}^2}$
low shear area	$LSA = \frac{\text{area of the aneurysm under the low WSS}}{\text{area of whole aneurysm}} \cdot 100\%$
inflow concentration index	$ICI = \frac{\text{flow rate in aneurysm/flow rate in parent artery}}{\text{area of the inflow region/area of the neck plane}}$
shear concentration index	$SCI = \frac{\int_{S_h} \text{WSS}\,dS / \int_S \text{WSS}\,dS}{S_{high}/S}$
viscous dissipation ratio	$VDR = \frac{\int_V 2\mu_* \mathbf{D}\cdot\mathbf{D}\,dV/V}{\int_{V_{near}} 2\mu_* \mathbf{D}\cdot\mathbf{D}\,dV/V_{near}}$

Table 2.3: Hemodynamic parameters for evaluating the flow in the aneurysm - v, p, $\mathbf{D}$, WSS are velocity magnitude of the flow, normal pressure, symmetric part of the velocity gradient and wall shear stress, ρ_* and ν_* are constant density and dynamic viscosity. Low WSS is defined as a 10% of the WSS of the parent artery. S_{high} in SCI definition is the area of the region on the aneurysm where WSS is higher than the mean WSS over the parent artery, S is the area of the aneurysm. V_{near} is the volume of the "near" parent artery, V is the volume of the aneurysm.
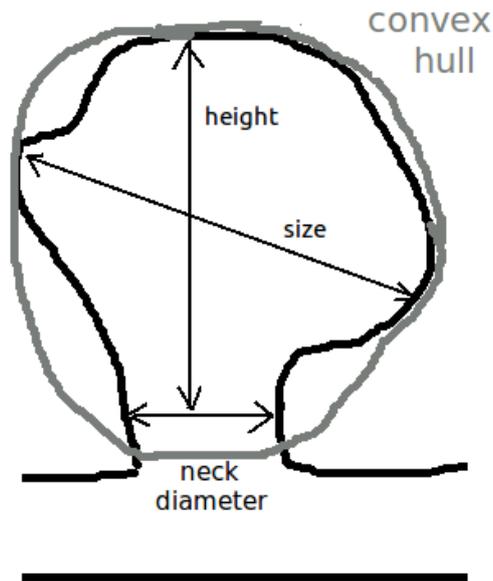
Figure 2.5: Scheme of an aneurysm representing the measurements of the morphological parameters: size of the aneurysm, neck diameter and the height of the aneurysm. The grey parts show the convex hull of the aneurysm. All of the parameters are measured from the three-dimensional pictures.

2.4 Numerical simulation in comparison with numerical benchmark

The Computational Fluid Dynamics Challenge for Rupture-Predicton in Intracranial Aneurysms (CFD Challenge) was announced in 2013 as an open challenge for CFD groups. It was organized by Die Otto-von-Guericke-Universität Magdeburg, see the website of the project (Challenge, 2013). The goal was to compute the blood flow through the two cases of the same type of aneurysms, one ruptured.

There were two phases of the CFD Challenge. In the first phase, the goal was to compute flow for both cases with arbitrary model, boundary conditions and blood parameters. According to the results, groups should compute WSS on the aneurysms and predict the rupture case and rupture place. Only the two geometries were provided.
In the second phase, the input boundary conditions were provided and the goal was to compare computed velocity and pressure firstly within the groups and secondly with the results of PIV experiment to serve as a numerical benchmark. The results of two phases were published in (Janiga et al., 2014) and (Berg et al., 2015).
In the first phase, participants were free to choose their own flow boundary conditions and significant differences appeared regarding to the WSS prediction (Janiga et al., 2014).

In the second phase, in the case of consistent boundary conditions, a good agreement among the 26 groups (from 15 countries), was achieved. Additionally, steady-state CFD results, provided on the prescribed planes, were successfully validated in a phantom model experiment but the input data were different than that provided in CFD Challenge and they were not published (Berg et al., 2015).

In this section we will compute the flow in the first geometry (case 1) under the prescribed inflow velocity magnitude from the second phase and compare it with the results from CFD Challenge.

Model

The geometry and inflow boundary condition were provided by the CFD Challenge. They are shown in Fig. 2.6.
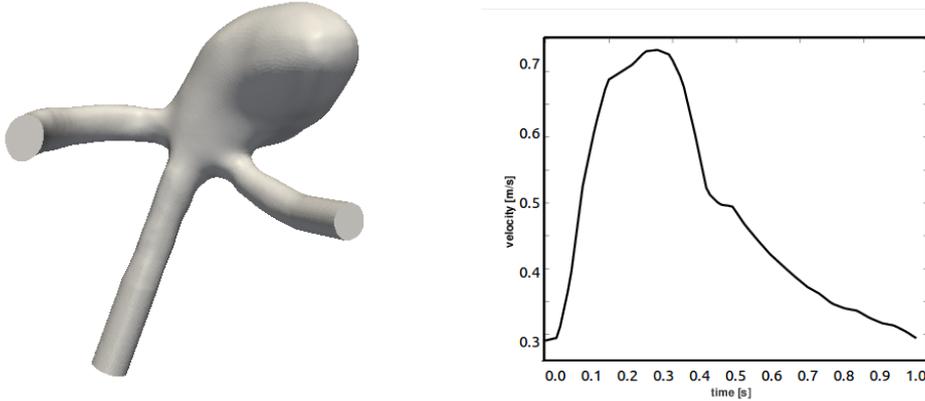
Figure 2.6: Geometry and velocity magnitude for inflow boundary condition, $\overline{V(t)}$, provided by CFD Challenge.

The surface mesh was provided in stl format, we generated only the volumetric tetrahedral mesh by iso2mesh software (Fang and Boas, 2009) with average edge length 0.4 mm.

The numerical model was as described in section 2.2 using constant flow on the inlet, $\mathbf{v}_{in} = -\overline{V(t)}\mathbf{n}$, where $\overline{V(t)}$ is shown in Fig. 2.6. Three cardiac cycles of a length 0.925 s were computed and the last one was used to the result analysis. The time step length was set to 0.00925 s. 8 CPUs were used for a computation using the Fstrin program (Hron and Mádlík, 2007). ParaView, an open-source, multi-platform data analysis and visualization application, was used for post-processing computation and visualization (Hansen and Johnson, 2011).

Two inlet planes and a centerline were published for a comparison in CFD Challenge. We will compare the "*CFD Challenge result*" with the "*Fstrin result*". CFD results mostly reflect the result using Ansys software (12 groups from 26) and constant flow velocity profile (16 groups from 26). The *Fstrin result* was obtained from the computation at time of maximal velocity in the last (third) cycle for both planes and a centerline. Also the time averaged values (over the third cycle) were compared on a centerline. The results are shown in Fig. 2.8, 2.9 and 2.7.
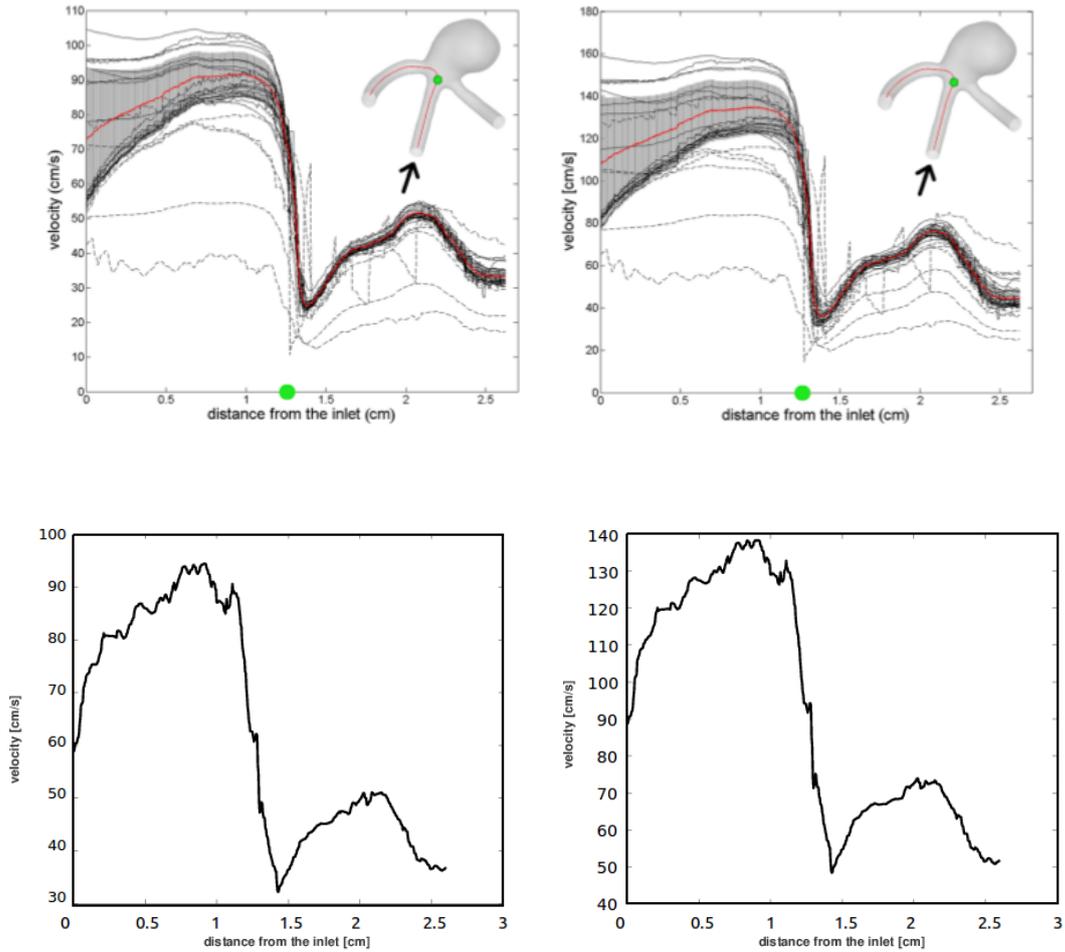
Figure 2.7: The *CFD Challenge results* (taken from (Berg et al., 2015)) and *Fstrin results* on a prescribed line firstly as cycle-averaged values, secondly at the time of maximal velocity.
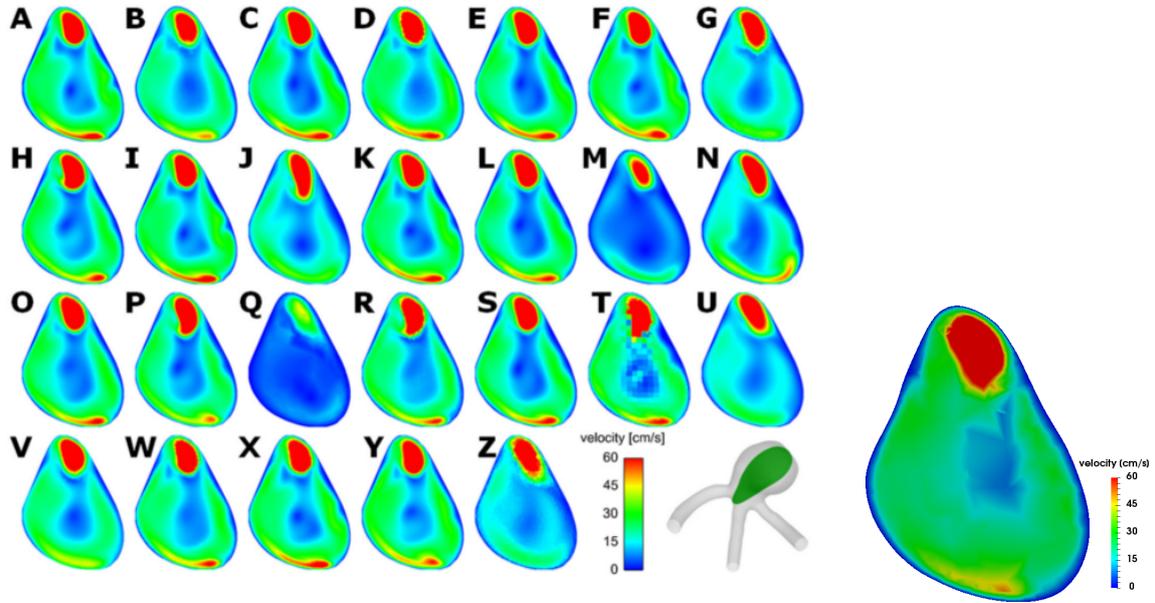
Figure 2.8: The *CFD Challenge results* (taken from (Berg et al., 2015)) and *Fstrin results* on a prescribed plane A.
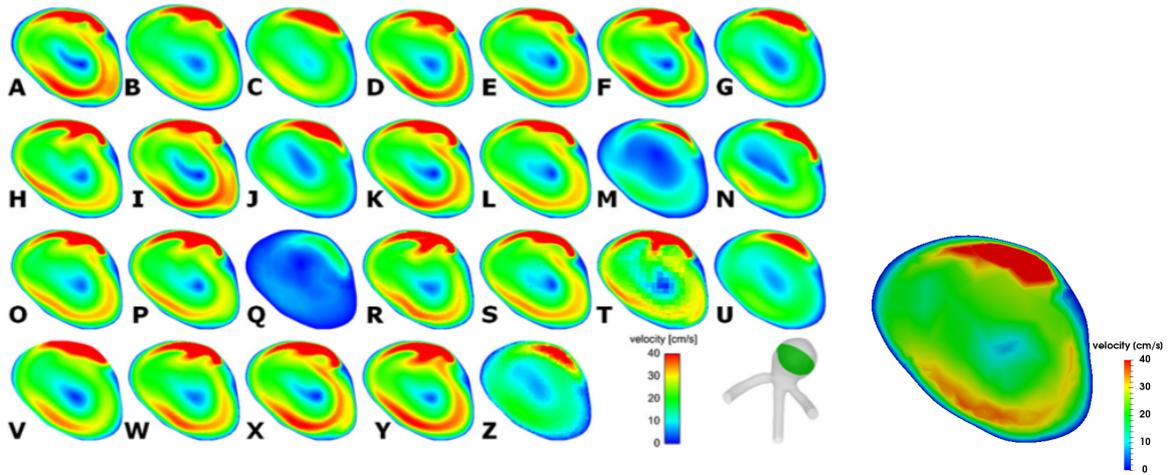

Figure 2.9: The *CFD Challenge results* (taken from (Berg et al., 2015)) and *Fstrin results* on a prescribed plane B.

Fstrin program was already tested against numerical benchmark in (Hron and Mádlík, 2007) and (Mádlík, 2010). This comparison was provided against other numerical softwares, mostly Fluent Ansys, on a geometry of intracranial aneurysm. The comparison on the planes inside an aneurysm shows the similar velocity magnitude distribution using

the same scale. Other comparison shows the velocity magnitude along the prescribed line from the inlet to an oulet plane. This results show higher variability in CFD Challenge results at the beginning of the line as different inlet velocity profiles were used. Groups in CFD Challenge mostly used the constant inlet velocity profile (16 groups from 26). The *Fstrin result*, using also constant velocity profile, shows the comparable values with the most common curve showing velocity magnitude along the line, see Fig. 2.7.

In the next section, we will show the numerical simulation using Fstrin program and parabolic velocity profile. There is a computation of flow and several hemodynamic parameters in a ruptured aneurysm. The correlation of the hemodynamic parameters and the site of rupture is provided.

2.5 Numerical simulation performed on two inflow aneurysm geometry

In this section we will show the numerical simulation on an aneurysm geometry representing the case of a patient operated on for a ruptured anterior communicating artery (ACom) aneurysm. The ACom is specified due to the two inflow vessels, see Fig. 1.3, so the two inflow study was performed. The hemodynamic parameters were calculated and correlated to the site of the rupture. This section takes parts from (Hejčl et al., 2017).

Mesh generation

The mesh was generated as was described in section 2.1. To avoid the influence of outflow condition we set the length of both outlet vessels to be similar. The final mesh contained 195 000 elements with an average node spacing of 0.3 mm. The mesh is shown in Fig. 2.12-A.

Model parameters

CT angiography was performed with a pixel resolution of 0.6 mm. The model was as described in section 2.2. Four cardiac cycles of a length 1s were computed and the last one was used to the result analysis. The time step length was set to 0.01 s. 8 CPUs were used for a computation.

A program for computing 3D Navier-Stokes equations by a finite element method, Fstrin (Hron and Mádlík, 2007), developed at the Mathematical Institute of Charles University, was used for the numerical calculation under the assumptions of rigid walls and an incompressible Newtonian fluid with a constant kinematic viscosity ν_*, see Tab. 2.1.

All numerical experiments were computed on a 64-bit cluster Snhurka (Computational cluster Snhurka, http://cluster.karlin.mff.cuni.cz). There are 180 computing hardware nodes based on Intel Core i7 CPUs with 832 GB of RAM in total, running on a Linux Operating System.

Boundary conditions

The parabolic profile (2.5) was used at the both inlets. The patient-specific flow data were not available so 1s cardiac cycle length was simulated with a time dependence of the magnitude of the average inlet velocity $\overline{V(t)}$ shown in Fig. 2.11. The geometry of the aneurysm had two different inputs, denoted here as A1 and A1 and two different outputs, see Fig. 2.10. Zero surface-traction vectors were prescribed on the outlets and a no-slip boundary condition on the walls.
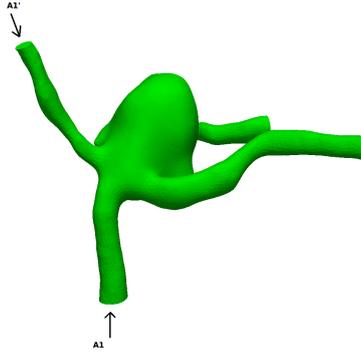

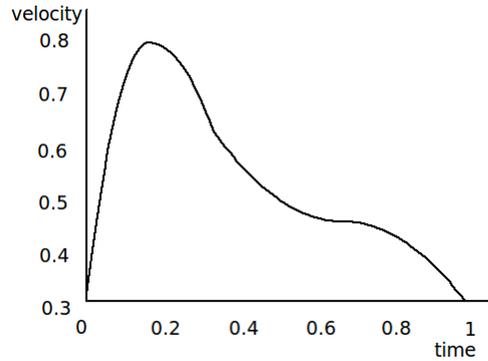Figure 2.10: The geometry with two inflow vessels - A1 and A1'.

Figure 2.11: Time dependence of a mean inflow velocity, $\overline{V(t)}$, prescribed at A1 and A1' in $\frac{m}{s}$.

A two-inflow study

There were five different computations performed on the same mesh representing an aneurysm with two input vessels. The first computation was prescribed with the same flow on A1 and A1 with the velocity prescribed between 0.3 and $0.8\frac{m}{s}$. The other four computations had fixed curvature and fixed diastolic velocity $0.3\frac{m}{s}$ but different maximal input velocities. While we prescribed $0.8\frac{m}{s}$ maximal input velocity for both, A1 and A1 planes for the first case, for the other cases we prescribed a 5% and a 10% (and vice versa for both situations) change between the two inputs. The list of values of the maximal inflow velocities in both input vessels is shown in Tab. 2.4.

Correlation of hemodynamic parameters to the site of the rupture

Four cardiac cycles were computed on two meshes to test the mesh dependency of the results. The hemodynamic parameters WSS, time averaged WSS (TAWSS) and the oscillatory shear index (OSI) were computed on the last cardiac cycle. The streamlines showed a concentrated inflow jet directed straight at the rupture point (Fig. 2.12-B). As seen on the cutting plane, the velocity vectors at the peak velocity time step made a small vortex at the small bleb of the aneurysm, but this location did not correspond with high pressure or high WSS values (Fig. 2.12-C). OSI, a non-dimensional parameter with the values between

inflow condition	max $\overline{V(t)}$ for A1 (m/s)	max $\overline{V(t)}$ for A1' (m/s)
50-50	0.8	0.8
45-55	0.72	0.88
55-45	0.88	0.72
40-60	0.64	0.96
60-40	0.96	0.64

Table 2.4: **A two-inflow study:** The CFD for the case of a ruptured ACom aneurysm was calculated under these 5 different inflow conditions.

0 and 0.5, was significant around the blebs but not on them (Fig. 2.12-D). The WSS on the aneurysm sac was lower than the WSS on the anterior cerebral blood vessels with several smaller regions of elevated WSS on the aneurysm dome (Fig. 2.12-E); one of the sites was the point of rupture as identified during surgery. The point of rupture is within a larger region of high pressure (normal stress on the wall) (Fig. 2.12-F).

A two-inflow study - results

Several hemodynamic parameters were computed for five cases with different inflow conditions, defined in Tab. 2.4. The velocity field, WSS and normal pressure are shown at peak systolic time where maximal input velocity is prescribed. Fig. 2.14 shows changes in the WSS under the 5 different conditions. The distribution of the WSS is relatively stable on the surface of the aneurysm sac, with some distortion in cases of decreased flow from the left A1 artery. In all cases the site of rupture is in the region of increased WSS. Concerning the TAWSS parameter, the similarity is even better. In terms of the character of flow, the velocity vectors show minimal changes under the 5 different conditions (Fig. 2.13). The changes in the values of pressure, stress in normal direction, are more obvious; not only in the magnitude but also in the distribution on the aneurysm sac (Fig. 2.15). For all 5 cases the site of high WSS and high pressure correspond to the site of rupture.
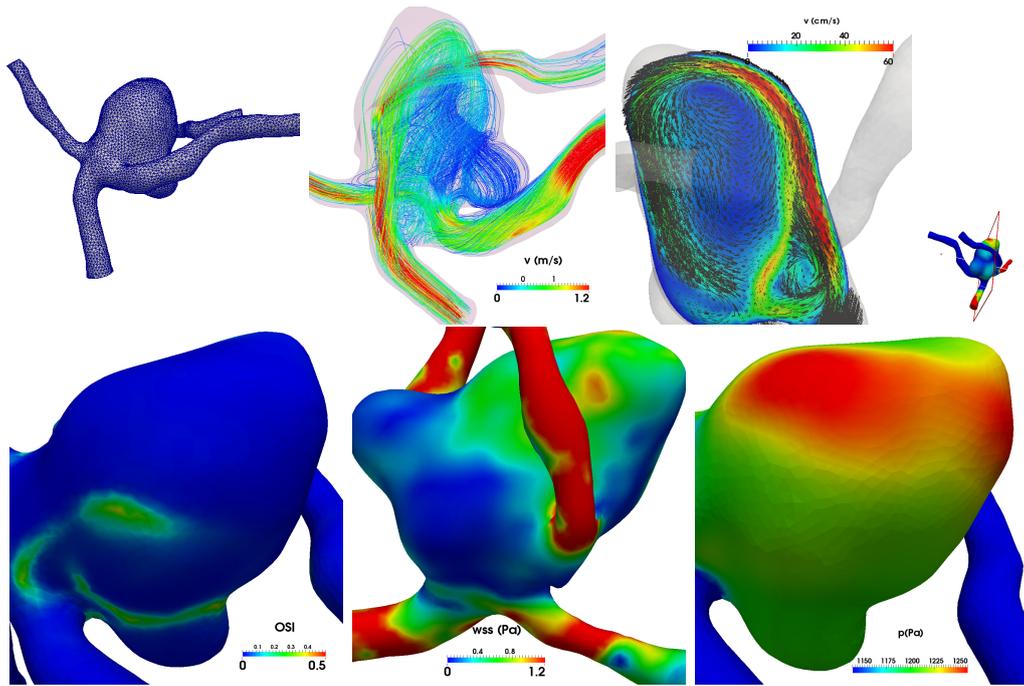
Figure 2.12: Correlation of hemodynamic parameters to the site of the rupture for an ACom aneurysm. A. - 3D mesh containing 195 000 element reconstructed from the CT angiography. B. - The streamlines showed a concentrated inflow jet directed straight at the rupture point. C. - The velocity vectors at the peak velocity time step made a small vortex at the small bulb of the aneurysm, as we can see in the cutting plane (the plane section is illustrated in the lower right corner). D. - The OSI was significant around the blebs but not on them. E. - The site of rupture was in a region of increased WSS. F. - The site of rupture was also in an area of increased wall pressure.
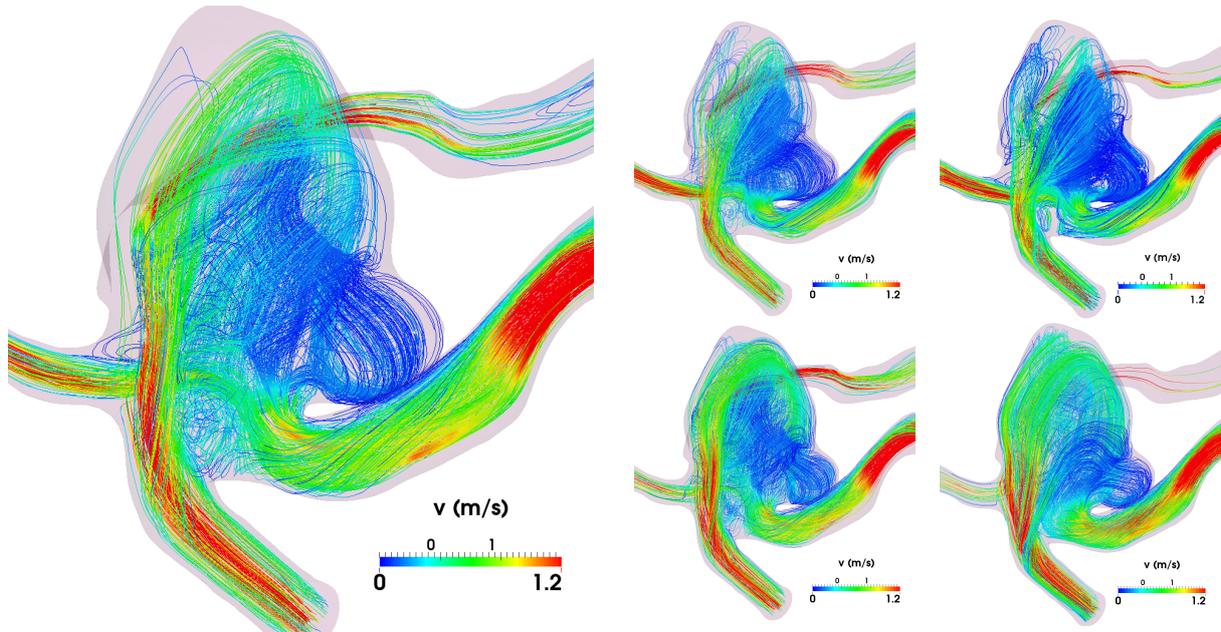
Figure 2.13: Distribution of blood flow under the 5 different situations specified in Tab. 2.4. Left column: 50-50 case, middle column: up 45-55, down 55-45, right column: up 40-60, down 60-40. All figures have the same scale in a range $0 - 1.2\frac{m}{s}$.
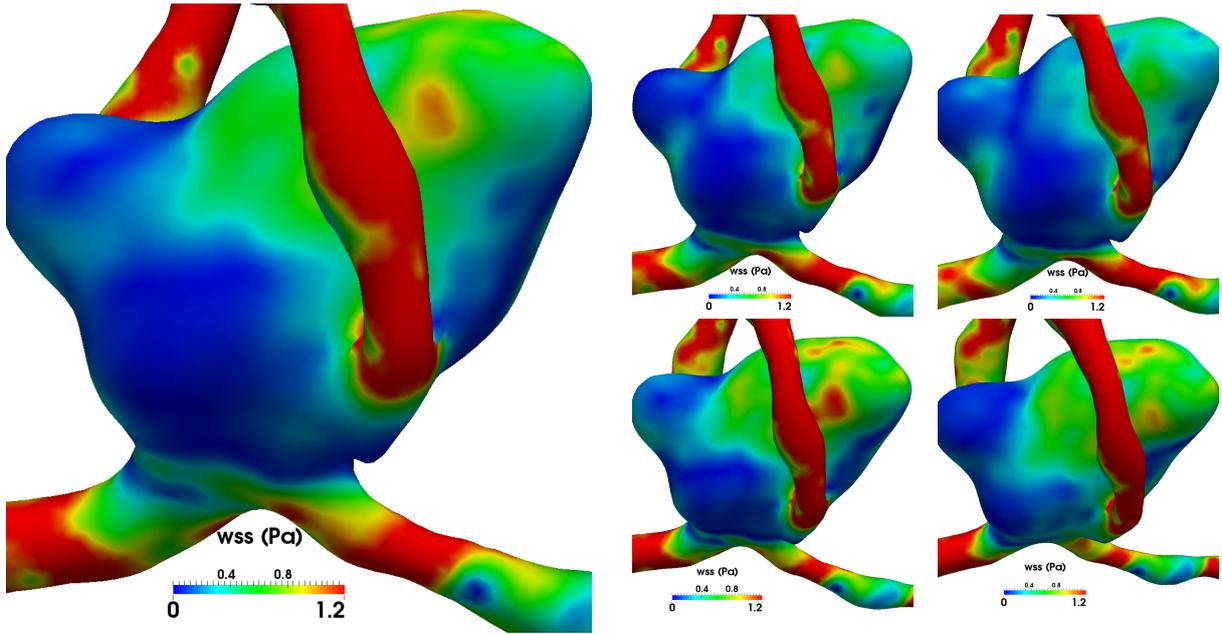
Figure 2.14: Distribution of peak WSS under the 5 different situations specified in Tab. 2.4. Left column: 50-50 case, middle column: up 45-55, down 55-45, right column: up 40-60, down 60-40. All figures have the same scale in a range $0 - 1.2$ Pa.
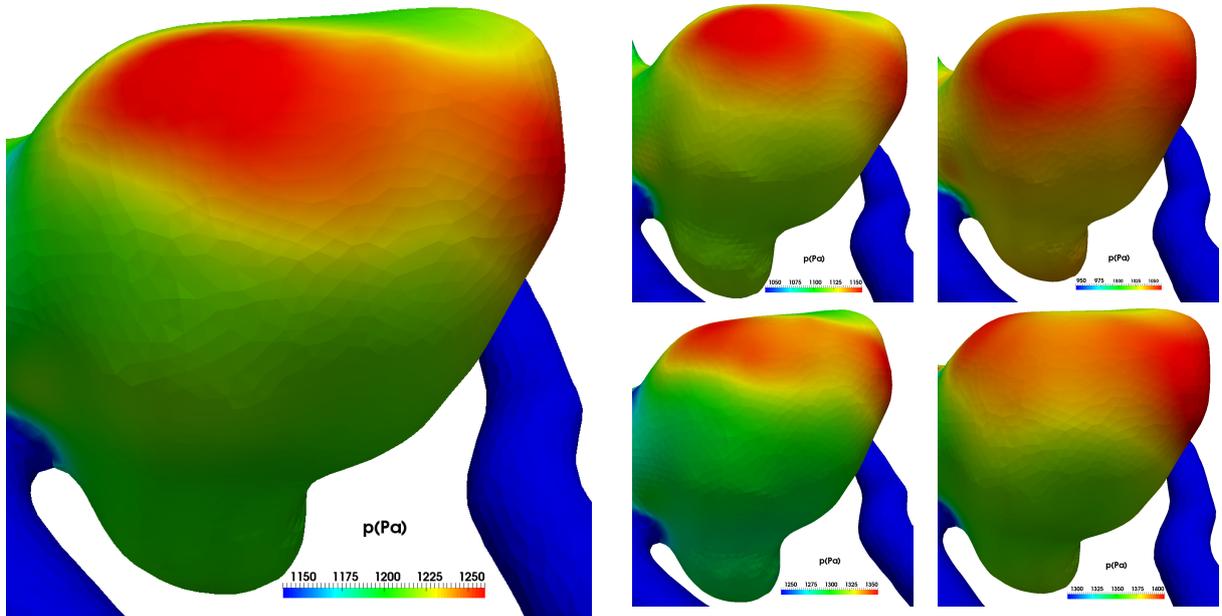

Figure 2.15: Distribution of normal pressure under the 5 different situations specified in Tab. 2.4. Left column: 50-50 case, middle column: up 45-55, down 55-45, right column: up 40-60, down 60-40. The figures have the different scales but always with 100 Pa difference between the maximal and minimal value.

Conclusion

In this chapter we showed the application of the patient specific modeling described in sections 2.1 - 2.3 on a ruptured case of an ACom aneurysm. The ruptured point corresponds to the point of inflow jet with a peak in WSS and high pressure. The aneurysm was located in the branching of the vessels with two inflows and two outflows. The high WSS and high pressure corresponded to the site of rupture also in the cases with different inflow conditions when the flow was not the same for both inputs.

2.6 Numerical simulation of the wall shear stress on 20 middle cerebral aneurysms

Recent studies examined the hemodynamic factors on unruptured and ruptured aneurysms to find a potential marker determining which unruptured aneurysm has tendency to rupture (Shojima et al., 2004; Cebral et al., 2007; Jou et al., 2008; Cebral et al., 2010; Miura et al., 2012; Meng et al., 2013). The most popular hemodynamic parameter is WSS. But larger aneurysms are associated with lower WSS regardless the rupture status (Lauric et al., 2013). Since this fact can lead to many misunderstandings, recent studies are focused not only on one location in the brain but also on the similar size of the aneurysms. The purpose of this work is to show the dependence of the WSS on the volume of the aneurysm and to show the WSS association with rupture status in volume matched saccular aneurysms. The result is the same as was obtained in (Lauric et al., 2013) in volume matched sidewall aneurysms.

Aneurysm selection and image segmentation

Twenty aneurysms in twenty patients were chosen from the database. The criteria for inclusion of aneurysms were based on good quality 3D digital subtraction angiography image, the location of the aneurysm and the rupture status. All cases were located in the middle cerebral artery (MCA), 10 of them were ruptured and 10 unruptured. The aneurysm sizes differ from 2.41 to 7.48 mm for ruptured aneurysms and from 2.67 to 6.49 mm for unruptured group. Aspect ratio, ratio between aneurysm height and neck diameter, was between values 0.3 and 1.5 for ruptured group and between 0.5 and 1.43 for unruptured group. Ten aneurysms were considered as *smaller* due to the size and volume, five of them from ruptured group. Ten other aneurysms were considered as *bigger*. Volumetric datasets, including aneurysm and parent vessel were then obtained and analyzed by the software Mimics 16.0 (Materialise, Leuven, Belgium) while the triangular surface mesh was obtained using ICEM CFD (ANSYS, Inc., Canonsburg, PA).

Mesh generation

From segmented and smoothed geometry of the aneurysm, the aneurysm neck was defined for better analysis and the mesh adaptivity. Meshes are constructed to be finer near the aneurysm neck, on the aneurysm dome and also in the branching of the vessels, if necessary. The surface meshes were used to create tetrahedral meshes for all cases with the approximately five million cells. Two aneurysms, one ruptured and one unruptured, were tested for grid independence. The importance of grid dependence test is described in (Hodis et al., 2013). For both aneurysms, four meshes with maximal edge length 0.2, 0.25, 0.3 and 0.35 mm were constructed. The average edge length was actually much lower. The chosen maximal length of the edge was then set to 0.25 mm. The results of mesh sensitivity for the unruptured case are shown in Tab. 2.5.

variable	$a_{\max} = 0.35\,\mathrm{mm}$	$a_{\max} = 0.3\,\mathrm{mm}$	$a_{\max} = 0.25\,\mathrm{mm}$	$a_{\max} = 0.2\,\mathrm{mm}$
PWSS dome	0.9586	0.9583	0.9601	0.9589
TAWSS dome	0.5057	0.5057	0.5046	0.5046
TAWSS PA	1.1390	1.1390	1.1394	1.1397
TALSA	0.4266	0.4315	0.4441	0.4441
OSI dome	0.0147	0.0146	0.0145	0.0145

Table 2.5: Results of mesh sensitivity test provided on a geometry of an unruptured aneurysm with different maximal edge length $a_{\max}$. The mesh with $a_{\max} = 0.25\,\mathrm{mm}$ was chosen for a computation. P referrs to the results at maximal time velocity, TA to the cycle averaged results. Results are averaged over the aneurysm dome (dome) or over the parent artery (PA). WSS values are shown in Pa.

The model and boundary conditions

The Newtonian model, described by Navier-Stokes equations, with constant dynamic viscosity $\mu_* = 0.0035\,\mathrm{Pa\,s}$, was applied to all aneurysms using Fluent 16.1 (ANSYS, Inc, Canonsburg PA), with a second-order implicit solver in both time and space. The finite volume method was applied with prescribed velocity inflow boundary condition and zero pressure outflow boundary condition. The inlet branch was modified in the extension to have a circular surface to Womersley velocity profile can be applied. The transient waveform, used also in (Hodis et al., 2013), is given by (Zamir, 2005). All the outlet branches were extended such that their surfaces were almost perpendicular to the vessel. The formula for Womersley profile is not trivial and its derivation can be found in (Womersley, 1955). Womersley number was assumed 3.7, blood density $\rho_* = 1050\frac{\mathrm{kg}}{\mathrm{m}^3}$.

Visualization of the results and statistical analysis

Time step was chosen as $0.001\,$s to ensure that the maximum Courant number was under 20, every tenth time slice solution was saved to be analyzed. The unknowns in the Navier-Stokes equations are velocity and the pressure. From velocity field, the velocity gradient and WSS were computed. As the pressure can be thought as the normal component of the stress performing on the vessel, the WSS is its tangential part and is thought to be responsible for the potential degenerative forces acting on the endothelial cells in intima part of the vessel (Cebral et al., 2010; Meng et al., 2013). The WSS was compared between the ruptured and unruptured group as value spatially averaged over the dome, and also over the parent vessel. Parent vessel was chosen as the part of the vessel between the aneurysm and the last branching. This is showed i.e. in (Fukazawa et al., 2013). The other variables computed for the purpose of this paper were oscillatory shear index (OSI) and low shear area (LSA). Definitions of these parameters are provided in Tab. 2.3. For all post-processing visualization software Tecplot was used (Tecplot 360, 2013 Tecplot, Inc.). As not all morphological and hemodynamic parameters were normally distributed, the Wilcoxon-Mann-Whitney U test was used to data analysis. Both groups were of the size n=10, the values were taken as significantly different for P value lower than 0.05.

Results

The parameters distribution according to the rupture status

Three cardiac cycles with a period of $1\,$s were computed and the last one was used to analyze the hemodynamic parameters. The results are shown either in the peak systole $2.43\,$s referred as the P (peak values), or averaged over the last cycle (from $2.0\,$s to $2.99\,$s when 100 solutions with different time were saved) referred as TA (time averaged). The TAWSS distribution on the dome is shown in Fig. 2.17.

We analyzed morphological parameters (size, volume, surface, nonsphericity index and aspect ratio of the aneurysm) and the hemodynamic parameters (WSS, OSI and LSA) according to the rupture status of the aneurysms. The results are shown in Tab. 2.6. The aneurysm neck diameter in this sample was higher for the unruptured group (4.4 ± 1.4 vs. $5.4 \pm 1.2\,$mm) and this was the only parameter with statistical significant difference (P < 0.05). The sizes for both groups were similar (8.43 ± 5.20 for ruptured vs. $8.38 \pm 3.11\,$mm for unruptured), as aspect ratio (1.36 ± 0.77 for ruptured vs. 1.24 ± 0.45) but the volume was higher in the ruptured group ($352.5 \pm 588.5\,$mm^3 vs. $214.9 \pm 220.1\,$mm^3).

The parameters distribution according to the size

WSS is lower in larger aneurysms. Fig. 2.16 shows the TAWSS dependence on the volume and size. In this case, the plot of TAWSS dependence on volume can be approximated as

$$\text{TAWSS} \approx \frac{1}{\text{volume}^{0.274}}.$$

We analyzed the same group of parameters for all aneurysms according to their volume. All twenty aneurysms were divided into two groups regardless their rupture status. They were considered as *bigger* if the volume was greater than $100\,\mathrm{mm}^3$ or as *smaller* otherwise. More hemodynamic parameters were significantly different as is shown in Tab. 2.7. Both peak and time averaged values for LSA were more than three times less for *smaller* group than for *bigger* group. The P value was 0.0013 for PLSA and 0.0073 for TALSA. On the other hand, the ratio between TAWSS on dome and one tenth of the TAWSS on parent artery was higher in *smaller* group ($322.7 \pm 128.1\%$ vs. $123.2 \pm 69.5\%$, P = 0.0036). OSI was significantly higher in *bigger* group. For maximal OSI over the dome the P value was 0.0091, for spatially averaged OSI on dome P = 0.0376. The computation did not show the significantly higher WSS on dome for *smaller* aneurysms but the P values were closed to 0.05, namely it was P = 0.064 for PWSS and P = 0.0539 for TAWSS.

The volume matched study

The volume dependence of the TAWSS can be avoided by studying the volume matched aneurysms. In our selected aneurysms three pairs of saccular aneurysms located in MCA were matched in the volume and shape. The aneurysms were chosen to have similar volume, size and surface area, although the aspect ratio could be different. These six cases are shown in Fig. 2.18.

The streamlines and WSS distribution were used to visualize the flow and the WSS histograms were plotted in Fig. 2.18. Volume in the pairs was about $190\,\mathrm{mm}^3$, $80\,\mathrm{mm}^3$ and $12\,\mathrm{mm}^3$. In all three pairs here we can observe the WSS histogram peak had a left shift for ruptured aneurysms. Only in the smallest pair we can observe also the bimodal distribution for ruptured case.

The discussion, summarizing the morphological and hemodynamic parameters used in recent studies and thought to be involved in aneurysm formation, follows.
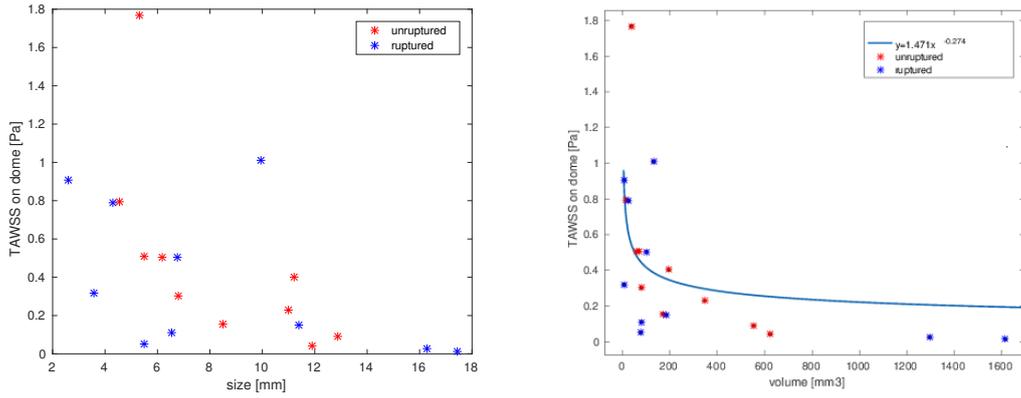
Figure 2.16: TAWSS dependence (also spatially averaged over the dome) on size and volume of the aneurysm. The figure shows no particular dependence on the dependence on volume can be approximated by the relation TAWSS $\approx \frac{1}{volume^{0.274}}$ with $R^2 = 0.2512$, SSE = 2.769.
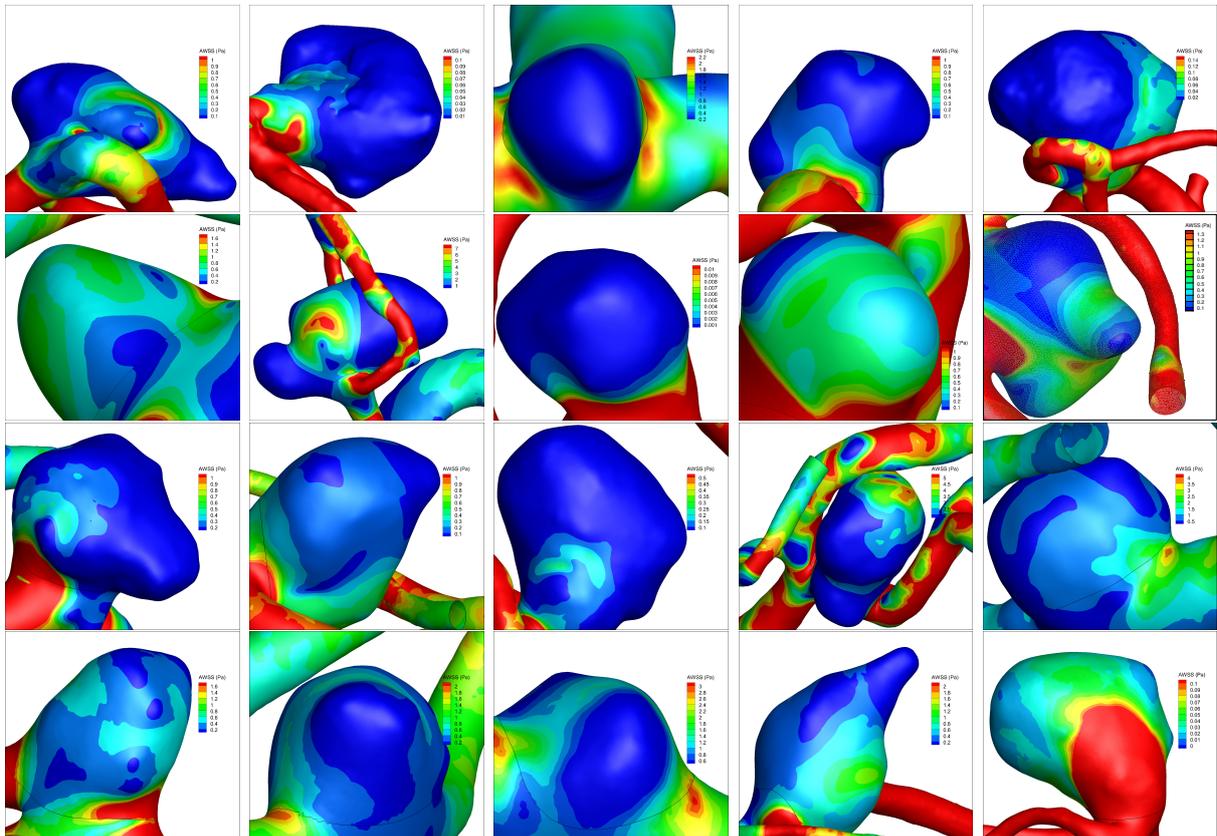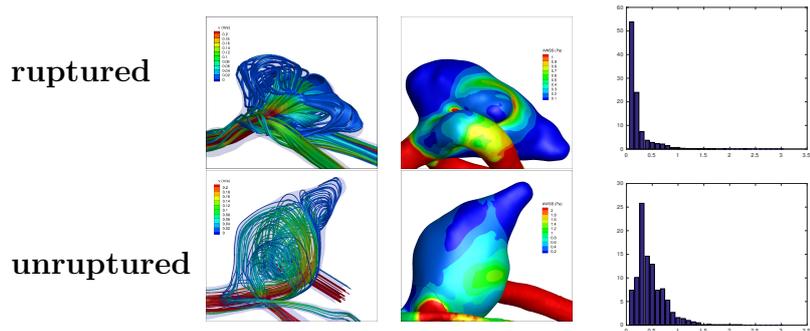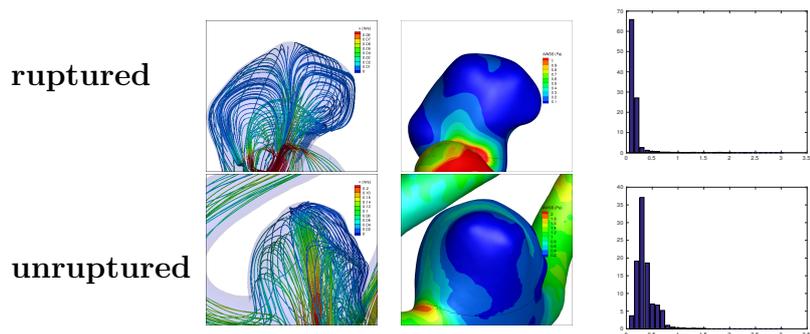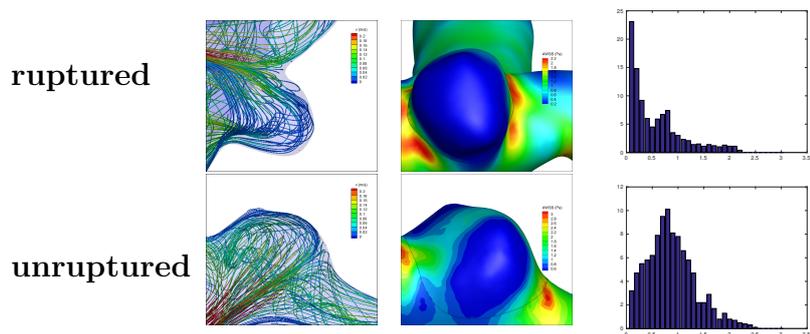

Figure 2.17: TAWSS distribution on the aneurysm dome. The first two rows show the ruptured aneurysms, the last two rows show the unruptured aneurysms.

Area: 160, 150 mm^2. Volume: 185, 195 mm^3.
Size: 11.4 mm, 11.2 mm. Aspect ratio: 0.9, 0.7.

Area: 83, 75 mm^2. Volume: 80, 79 mm^3.
Size: 6.6 mm, 6.8 mm. Aspect ratio: 0.86, 1.36.

Area: 18, 23 mm^2. Volume: 10, 14 mm^3.
Size: 3.6 mm, 4.6 mm. Aspect ratio: 1.5, 0.52.

Figure 2.18: Volume and shape matched pairs: The figure shows the streamlines, WSS distribution and WSS histograms for the volume matched aneurysms, always ruptured and unruptured case. For the biggest pair (volume 185 and 195 mm^3), the flow can be described as vortex forming when the vortex is more visible in unruptured case. The flow in the middle pair can be described as flow separated into two flow streamlines families. Only the third pair has the different flow for ruptured and unruptured case where the ruptured case has a rounded flow in aneurysm and unruptured case can be described as flow separated.

Parameter	Ruptured(n=10)	Unruptured(n=10)	P Value
Size [mm]	8.433 ± 5.201	8.379 ± 3.108	0.6776
Aneurysm neck diameter [mm]	4.419 ± 1.430	5.370 ± 1.214	0.0452
Aspect ratio	1.362 ± 0.774	1.238 ± 0.445	0.9096
Aneurysm volume [mm^3]	352.450 ± 588.478	214.860 ± 220.097	0.7913
Aneurysm surface [mm^2]	193.040 ± 250.045	145.660 ± 114.270	0.9097
Nonsphericity index	0.164 ± 0.084	0.113 ± 0.064	0.1859
mean PWSS dome [Pa]	0.728 ± 0.802	0.885 ± 0.921	0.6232
mean PWSS parent artery [Pa]	3.483 ± 4.421	2.452 ± 2.712	0.5708
mean TAWSS dome [Pa]	0.388 ± 0.387	0.480 ± 0.506	0.5708
mean TAWSS parent artery [Pa]	2.325 ± 2.723	1.688 ± 1.678	0.6776
peak LSA [%]	48.615 ± 34.359	31.351 ± 31.405	0.3075
aver LSA [%]	52.815 ± 32.067	27.827 ± 30.967	0.0890
$\frac{\text{TAWSS dome}}{0.1 \cdot \text{TAWSS parent artery}} \cdot 100\%$ [%]	180.815 ± 146.161	265.062 ± 134.320	0.1212
max OSI dome	0.864 ± 0.158	0.727 ± 0.259	0.2123
mean OSI dome	0.045 ± 0.031	0.024 ± 0.009	0.0820

Table 2.6: Morphological and hemodynamic parameters for ruptured and unruptured aneurysms.

Parameter	*bigger* (n=10)	*smaller* (n=10)	P Value
Size [mm]	11.283 ± 3.766	5.529 ± 2.034	0.0010
Aneurysm neck diameter [mm]	5.787 ± 1.027	4.002 ± 1.093	0.0058
Aspect ratio	1.440 ± 0.763	1.160 ± 0.422	0.5449
Aneurysm volume [mm^3]	521.640 ± 527.695	45.670 ± 30.724	0.0002
Aneurysm surface [mm^2]	287.030 ± 212.734	51.670 ± 28.227	0.0002
Nonsphericity index	0.192 ± 0.053	0.085 ± 0.060	0.0017
mean PWSS dome [Pa]	0.467 ± 0.568	1.146 ± 0.962	0.0640
mean PWSS parent artery [Pa]	3.372 ± 4.432	2.564 ± 2.736	0.7913
mean TAWSS dome [Pa]	0.262 ± 0.308	0.605 ± 0.500	0.0539
mean TAWSS parent artery [Pa]	2.195 ± 2.753	1.819 ± 1.672	0.5205
peak LSA [%]	63.663 ± 24.877	16.303 ± 21.622	0.0013
aver LSA [%]	61.033 ± 26.548	19.609 ± 26.001	0.0073
$\frac{\text{TAWSS dome}}{0.1 \cdot \text{TAWSS parent artery}} \cdot 100\%$ [%]	123.217 ± 69.540	322.659 ± 128.116	0.0036
max OSI dome	0.889 ± 0.188	0.702 ± 0.218	0.0091
mean OSI dome	0.038 ± 0.015	0.031 ± 0.032	0.0376

Table 2.7: Morphological and hemodynamic parameters for *bigger* and *smaller* aneurysms.

2.7 Discussion

Twenty intracranial aneurysms located at the middle cerebral artery were examined in this study. The aneurysms were divided into two groups firstly according to their rupture status to ruptured and unruptured, secondly according to their size to *bigger* and *smaller*. Three pairs of volume matched aneurysms were compared. Several morphological and hemodynamic parameters were computed.

It was shown that commonly used hemodynamic factors, WSS, LSA and OSI, are closely associated with the volume of the aneurysm. The plot of the WSS as a function of volume was performed. However, the WSS distribution, represented through the WSS histograms, in volume matched aneurysms was different for the ruptured and unruptured cases. The suggested approach is to compare volume matched pairs of ruptured and unruptured aneurysms to avoid the confounding dependence of the WSS on the aneurysm volume.

Tab. 2.8 summarizes the parameters found to be statistically significant for the ruptured and unruptured aneurysm in the discussed studies.

The morphological parameters should be prescribed to evaluate the size and shape of the aneurysm. They are mentioned and discussed in (Dhar et al., 2008). The most common parameters are size and aspect ratio. However, aneurysm rupture status have been found to correlate also with the undulation, nonsphericity and ellipticity indices and aspect ratio. (Duan et al., 2014; Dhar et al., 2008) Another potential rupture risk comes with the irregularity of the aneurysm sac and bleb presence (Zhang et al., 2014; Liu et al., 2013).

Discussing the flow in aneurysms we try to have also a set of the hemodynamic parameteres. Recently, the flow complexity and concentration, combined with small impingement zone were investigated with the rupture risk (Cebral et al., 2010). These parameters were also found to correlate with the point of rupture compared to the rest of an aneurysm sac (Hodis et al., 2013; Sejkorová et al., 2016; Hejčl et al., 2017). The classification of the flow proposed in (Naito et al., 2012) was used in Fig. 2.18.

The most common hemodynamic parameter is wall shear stress (WSS), the tangential part of the stress vector acting on the aneurysm sac. Recently, the hypothesis is that both high and low wall shear stress can cause the pathogenesis of the aneurysm (Cebral et al., 2010; Cebral and Meng, 2012; Meng et al., 2013). High flow, resulting in high wall shear stress with positive wall shear stress gradient, can cause the endothelial injury and rupture, and can also be responsible for the aneurysm initiation (Metaxa et al., 2009; Chien et al., 2009). On the other hand, low flow with high oscillations, resulting in low WSS with high OSI or high RRT, can cause the remodeling of the wall and plaque formation (Cebral et al., 2010; Meng et al., 2013).

WSS was found to be significantly higher in ruptured aneurysms ((Cebral et al., 2010) on 210 cases, (Shojima et al., 2004) on 20 MCA). On the other hand, the ruptured aneurysms were found to be significantly bigger than the unruptured group with signifi-

cantly lower WSS (Miura et al., 2012; Duan et al., 2014; Zhang et al., 2014).

(Jou et al., 2008) also showed that maximal and spatially averaged WSS is a function of the aneurysm area. However, they also showed that low shear area (LSA) was significantly lower in ruptured aneurysms. LSA combined the information of the WSS on dome with the WSS on the parent artery, see Tab. 2.3.

Also the oscillatory shear index (OSI) was found to be significantly higher for ruptured group (Lu et al., 2011). But according to the published data in (Lu et al., 2011), the P value for the LSA was 0.15, not published 0.015, so the LSA was not statistically significant in this case.

In several studies the WSS has not shown a significant difference between ruptured and unruptured aneurysms. These studies suggested that other hemodynamic parameters could play a role in the risk assessment of intracranial aneurysms. One such parameter is the energy loss, which has shown difference between ruptured and unruptured ICA-PCom and ICA aneurysms (Qian et al., 2011; Liu et al., 2013), or pressure loss coefficient on MCA aneurysms (Takao et al., 2012).

Another effort was made to investigate the growing and ruptured aneurysms or the aneurysms with atherosclerosis presence. WSS was found to decrease during the aneurysm growth (Tanoue et al., 2011; Sejkorová et al., 2016) and to be significantly lower at the ruptured points (Fukazawa et al., 2013). The significant evidence was shown between the relative residence time (RRT) and atherosclerosis presence (Sugiyama et al., 2013). But they also showed no significant evidence between the OSI and atherosclerosis.

As was discussed in (Lauric et al., 2013), the analysis on aneurysmal datasets which do not compensate for difference in aneurysm size or volume is very likely to report low WSS thresholds not sensitive for small aneurysms. One of the approaches to compensate the volume difference among the aneurysms is to use the statistical WSS maps as in (Goubergrits et al., 2011). Histograms for the whole aneurysms surface then showed a left shift of the curve towards lower WSS for ruptured aneurysms. Histograms for the dome region additionally reveal a bimodal distribution for ruptured aneurysms with the higher first peak and the lower second peak. In unruptured aneurysms, the WSS distribution was more likely to be uniform. In all three pairs studied here we can observe the WSS histogram peak had a left shift for ruptured aneurysms. Only in the smallest pair we can observe also the bimodal distribution for ruptured case.

The other approach to avoid the volume influence is to use the volume matched aneurysms (Lauric et al., 2013). In this paper, we showed the wall shear stress was lower with increasing volume. In three pairs of volume matched aneurysms we observed WSS histograms shifted towards lower WSS for ruptured aneurysms. The same results was obtained for sidewall ICA aneurysms in (Lauric et al., 2013). They also proposed the TAWSS

dependence on volume to be as TAWSS $\approx \frac{1}{volume^p}$, $p < 1$. Best fitted curve for our data was the same curve with $p = 0.274$, see Fig. 2.16.

Our study has several potential limitations that may affect the results. As with other computational studies, we include the rigid walls and Newtonian flow assumptions that differ from the in vivo state. The Newtonian fluid assumption may underestimated blebs when blebs moved the WSS histograms to the left in non-Newtonian models (Hippelheuser et al., 2014). Also the simplified outflow boundary condition and eliminating small branches from the 3D segmented model should be mentioned. The study was performed on 20 cerebral aneurysms, 10 were ruptured. The changes of the size and the shape of the aneurysm immediately before and after the rupture might affected the results. The results of ruptured aneurysms might not characterize the aneurysm with high risk of rupture, but may only document the feature of the aneurysm after rupture. Further work to validate the model with in vivo data is needed.

study	#	U	R	location	parameter
Liu, 2013	110	84	26	-	EL, irregularity
Miura, 2012	106	63	43	MCA	AR, WSS, WSSG, normalized WSS, OSI, aneurysm formation index
Jou, 2008	26	18	8	ICA	LSA
Chien, 2009	8	4	4	ICA (small)	inhomogeneous WSS distribution, impingement size, high WSS, impingement location, flow direction
Takao, 2012	50	43	7	MCA	PLc
Takao, 2012	50	44	6	ICA-PComA	PLc
Duan, 2014	30	24	6	PComA	size, low normalized WSS, LSA ellipticity and undulation index, aspect ratio
Goubergrits, 2011	22	15	7	MCA	irregularity, WSS histograms after shape analysis
Shojima, 2004	20	17	3	MCA	low WSS in tips, location of max WSS
Cebral, 2010	210	127	83	-	larger inflow concentrations, larger max WSS, shear concentrations, VDR
Lauric, 2013	18	9	9	-	WSS in volume matched pairs
Dhar, 2008	45	25	20	-	size ratio, undulation, nonsphericity and ellipticity index, aspect ratio, aneurysm angle
Qian, 2011	30	26	4	ICA-PcomA	EL
Zhang, 2014	40	20	20	(mirror)	aspect ratio, LSA, WSSmin, irregularity
Lu, 2011	18	9	9	(mirror)	OSI

Table 2.8: Morphological and hemodynamic parameters found to be significantly different for the ruptured and unruptured aneurysms. # - number of the aneurysm included in the study, U - number of unruptured aneurysms, R - number of ruptured aneurysms. Location is provided if the aneurysms in the study were at the same location of the brain. Mirror aneurysms are the aneurysms not of the same location but the term mirror denotes two aneurysms in a patient, always one of them ruptured and the second one remained unruptured. The abbreviations are explained in Tab. 1.1 and 2.3, AR = aspect ratio, WSSG = WSS gradient.

3. Flow in highly narrowed domains representing stenotic aortic valve

In this chapter we will show the computations of the flow within the geometry approximating the stenotic aortic valve. In the introductory part, section 3.1, we will provide the medical background and current methods used for the stenosis severity evaluation. They are based on Bernoulli equation. In section 3.2, we will present the assumptions which lead to the Bernoulli equation and document that they are too simplifying and consequently irrelevant to capture real situations.

Namely, these assumptions mean neglecting integrals containing viscosity and convective term of Navier-Stokes equations. In section 5.3, we will demonstrate that values of these integrals are of the same magnitude as the pressure difference or energy dissipation and thus the assumptions leading to the Bernoulli equation are too restrictive to be apply to blood flow in stenotic valves.

Our numerical model is based on full continuum mechanics approach. The numerical model, including construction of geometry and boundary conditions, is presented in the section 3.3 with more detailed discussion of used backflow stabilization in section 3.4. Finally, the numerical results provided on the domain representing the stenotic aortic valve with symmetric obstruction up to 80% stenosis are shown and discussed in section 3.5. The results presented here were published in (Švihlová et al., 2017).

3.1 Introduction

We will concern with an aortic valve which is located between the left ventricle and the ascending aorta, as was shown in Fig. 1.1. The details of an aortic valve geometry are provided in section 3.3.1 in Fig. 3.4.

A stenosis in the cardiovascular system is a reduction in cross-sectional area of a structure across which blood flows, see Fig. 3.1. Because of the stenosis in valve, the heart must pump more to ensure the distribution of needed amount of blood. An anatomic stenosis, which is simply defined by its existence, may or may not result in a physiologically important stenosis. On the other hand, stenoses are generally treated in this pathologic case. The need of stenosis evaluation (whether this is physiologically important or not) is obvious. In the rest of this section, we will look at the background leading to the current stenosis evaluation based on the Bernoulli equation.
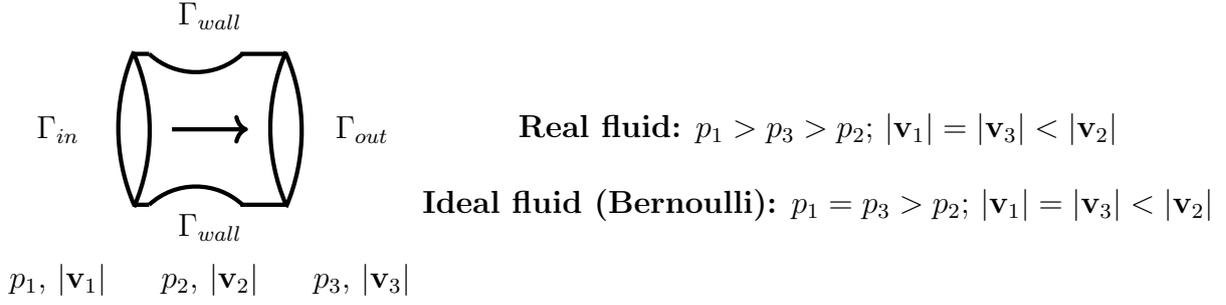
Γ_{wall}

Γ_{in} $\longrightarrow$ Γ_{out} **Real fluid:** $p_1 > p_3 > p_2$; $|\mathbf{v}_1| = |\mathbf{v}_3| < |\mathbf{v}_2|$

Ideal fluid (Bernoulli): $p_1 = p_3 > p_2$; $|\mathbf{v}_1| = |\mathbf{v}_3| < |\mathbf{v}_2|$

Γ_{wall}

$p_1, |\mathbf{v}_1|$ $p_2, |\mathbf{v}_2|$ $p_3, |\mathbf{v}_3|$

Figure 3.1: **Schematic of an valvular stenosis.** The diagram depicts an idealized stenosis within an aortic valve; position 1 = upstream of the stenosis, 2 = within the stenosis, 3 = downstream of the stenosis, $|\mathbf{v}|$ and p describe the velocity magnitude and pressure averaged over the cross-sectional area. For an ideal fluid, conservation of energy applies, and $p_1 = p_3 > p_2$, $|\mathbf{v}_1| = |\mathbf{v}_3| < |\mathbf{v}_2|$. The degree of p_2 decrease and $|\mathbf{v}_2|$ increase is determined by conservation of energy, with conservation of mass satisfied as well. When the Bernoulli equation is contrived to be used in the setting of energy dissipation, it is conveniently assumed that the pressure within the stenosis is equal to the pressure downstream of/distal to the stenosis, even though this lacks a rational basis. For the real case of flowing blood, $p_1 > p_3$ [with $(p_1 - p_3)$ quantifying the transvalvular pressure difference], typically $p_3 > p_2$ (but in principle p_3 can be $\leq p_2$), and $|\mathbf{v}_1| = |\mathbf{v}_3| < |\mathbf{v}_2|$.

We will focus mainly on two hemodynamic indicators, maximal pressure difference in aortic valve and aortic valve area as they are "the primary hemodynamic parameters recommended for clinical evaluation of AS (aortic stenosis) severity", together with direct measurement of aortic stenosis jet velocity, in the Echocardiographic assessment of valve stenosis: EAE/ASE recommendations for clinical practice (Baumgartner et al., 2009).

Gorlin formula

While valve area is strictly an anatomical assessment of stenosis severity for cardiac valves, physiological approaches have been employed to ascertain valve area. The archetype for this approach was developed by (Gorlin and Gorlin, 1951), with subsequent simplifications by (Hakki et al., 1981).

The basis for the Gorlin equation rests on Torricelli's modification of the Bernoulli equation:

$$h_1 \rho_* g + \frac{1}{2} \rho_* v_1^2 + p_1 = h_2 \rho_* g + \frac{1}{2} \rho_* v_2^2 + p_2 + Edis, \qquad \textbf{(Bernoulli equation)}$$

where 1 is used for the inflow part and 2 for the narrowed part (as they are labelled in Fig. 3.2), $h_1 \rho_* g$ and $h_2 \rho_* g$ are hydrostatic pressures, $Edis$ denotes the energy dissipation

and

$$v_1 = \frac{1}{|\Gamma_1|} \int_{\Gamma_1} |\mathbf{v}| \, dS, \qquad p_1 = \frac{1}{|\Gamma_1|} \int_{\Gamma_1} p \, dS,$$
$$v_2 = \frac{1}{|\Gamma_2|} \int_{\Gamma_2} |\mathbf{v}| \, dS, \qquad p_2 = \frac{1}{|\Gamma_2|} \int_{\Gamma_2} p \, dS. \qquad (3.1)$$

Torriceli's assumptions, namely that the short length of a valve leads to $p_1 \sim p_2 = p_{atm}$ and $(v_1 << v_2) \Rightarrow v_1$ neglected together with neglecting the energy dissipation, lead to the

$$2g(h_1 - h_2) = v_2^2. \qquad \textbf{(Torriceli's law)}$$

Since the hydrostatic pressure is proportional to h, then the maximal pressure difference, or pressure drop, is defined as $h^{drop} := h_1 - h_2$.

To include dissipation effects, (Gorlin and Gorlin, 1951) used an additional constant for velocity

$$v_2 = C\sqrt{2g}\sqrt{h^{drop}}$$

and conclude the final formula for aortic valve area (AVA) from the flow rate (Q) as

$$\text{AVA}_{\text{Gorlin}} = \frac{Q}{v_2} = \frac{Q}{C \cdot 44.5\sqrt{h^{drop}}}. \qquad \textbf{(Gorlin equation)}$$

Note that $[v_2] = \frac{cm}{s}$, $[h^{drop}] = mm$, $[Q] = \frac{ml}{s}$, $g \sim 981\frac{cm}{s^2}$. Consequently $\sqrt{2g} \sim 44.5\frac{\sqrt{cm}}{s}$ and the unit remaining for constant C is $\frac{\sqrt{cm}}{\sqrt{mm}}$. The "constant" used in Gorlin's equation was supposed to be empirical but it was evaluated in (Gorlin and Gorlin, 1951) by the mean value over an amount of patients. They suggested C to be equal 1 for aortic stenosis.

But C is actually a variable, and its value is in fact what describes energy dissipation. Moreover, the Bernoulli equation itself is an expression of conservation of energy, and thus is incapable of quantifying energy dissipation. Modifications of the Bernoulli equation using additional energy dissipation factors such as those in the Gorlin equation are totally empirical and in fact vary from condition to condition and, most importantly, from patient to patient without a basis in mechanics or mathematics that is reproducible across experimental conditions. Consequently, such approaches lack accurate and precise predictive capacity requisite of any sound theoretical model.

Gorlin/Hakki formula

Sometimes, a simplified Gorlin formula introduced by (Hakki et al., 1981) is used. It is based on substituting Q to the (**Gorlin equation**), where

$$Q \left[\frac{ml}{s}\right] = \frac{CO \left[\frac{l}{min}\right] * 1000 \left[\frac{ml}{l}\right]}{HR \left[\frac{beats}{min}\right] \cdot SET \left[\frac{s}{beat}\right]}$$

with HR = heart rate, SET = systolic ejection time and CO = cardiac output. The cardiac output is the amount of blood pumped by the heart per minute and can be measured. Then the formula

$$\text{AVA}_{\text{Hakki}} = \frac{\text{CO} \left[\frac{1}{\text{min}} \right]}{\sqrt{P1 - P2}} \qquad \text{(\textbf{Gorlin/Hakki equation})}$$

was presented, i.e. $\text{HR} \cdot \text{SET}$ was set to $\frac{1000}{44.5} = 22.47 \left[\frac{\text{s}}{\text{min}} \right]$. In the study on 60 patients, (Hakki et al., 1981) showed $\text{HR} \cdot \text{SET} = 22.66 \pm 2.88$ (values between 15.08 and 28.5). Setting this variable to be a constant is another considerable simplification.

Pressure difference derived from non-invasive Doppler techniques

The derivation for this approach was firstly used in (Hatle et al., 1978). The argumentation used there is not clear. Starting with modified Bernoulli equation with additional viscous term, they assumed it to be negligible. Neglecting also the energy dissipation they ended with

$$p^{drop} := p_1 - p_2 = \frac{1}{2} \rho_* (v_2^2 - v_1^2).$$

The pressure difference used here is the difference between hydrostatic pressures, not only the heights as in Gorlin formula. However, with v_1 set to zero, the final formula is the same as in (**Torriceli's law**), namely

$$p^{drop} = C \cdot v_2^2. \qquad \text{(\textbf{Hatle equation})}$$

Note that if $[p^{drop}] = \text{mmHg}$ and $[v_2] = \frac{\text{m}}{\text{s}}$, the "constant" $C \sim 4$ as it approximates $\frac{\rho_*}{2}$ ($\rho_* \sim 1050 \frac{\text{kg}}{\text{m}^3}$) multiplied by the constant $\frac{1\,\text{Pa}}{13534 \frac{\text{kg}}{\text{m}^3} \cdot 9.81 \frac{\text{m}}{\text{s}^2}} \cdot 1000 \frac{\text{mm}}{\text{m}} = 0.0075 \frac{\text{mmHg}}{\text{Pa}}$ using the density of the mercury. For comparison, Gorlin approach, using the same units, results in $p^{drop} = 5.05 \cdot v_2^2$.

Non-invasive techniques have been used to calculate pressure differences, as opposed to invasive direct measurements by catheterization. Nowadays, "cardiac catheterization is no longer recommended except in rare cases when echocardiography is non-diagnostic or discrepant with clinical data" (Baumgartner et al., 2009) in behalf of the non-invasive techniques, namely (**Hatle equation**) with $C = 4$. This approach also utilizes the Bernoulli equation. However, it is unlike the Gorlin-type approach specifically applied to heart valves, which at least incorporates an empirical constant to attempt to express energy dissipation (which in reality is actually highly variable). Rather, the Bernoulli equation is manipulated to allow determination of energy dissipation, even though it is an expression of energy conservation. It is conveniently assumed that energy losses in the flowing blood all occur at the outlet of a stenosis. As a consequence, the energy losses in the flowing blood can be expressed exclusively as losses in kinetic energy, and the pressure within the stenosis is equal to the pressure downstream of the stenosis. Further, the pressure difference across

the stenosis is thus equal to the loss in kinetic energy, which can be easily calculated based on non-invasively measured flow velocities at different locations relative to the stenosis.

Tab. 3.1, shows the different results in evaluating p^{drop} obtained by the non-invasive Doppler measurements, namely (**Hatle equation**) with $C = 4$ and those obtained by catheterization measurements. Loose correlations between non-invasively derived and invasively measured pressure gradients have been demonstrated. Moreover, other studies have demonstrated poor correlation between echocardiography calculations and catheterization measurements, see (Berger et al., 1984) and (Fischer et al., 1995).

study	N*	result**
(Berger et al., 1984)	44	$r = 0.79$, underestimation within 25% for 20 patients, more than 25% for 3 patients, failure for 1 patient
(Currie et al., 1985)	100	$r = 0.92$, SEE = 15, regression line: catheter $= 10.3 + 0.97 \cdot$ Doppler; table with data was not provided but the maximal difference from the graph was more than $50\,\text{mmHg}$
(Smith et al., 1986)	47	$r = 0.92$, SEE = 7.1, regression line: Doppler $= 2.8 + 0.87 \cdot$ Doppler; table with data was not provided but the maximal difference from the graph was more than $15\,\text{mmHg}$
(Burwash et al., 1993)	98	r=0.95, data not available

Table 3.1: Studies evaluating p^{drop} obtained by the non-invasive Doppler measurements in comparison with the catheter measurements; *number of people included in the study; **r=correlation coefficient, SEE = standard error in estimation computed as SEE $= \sqrt{\frac{\sum_1^N (Y-Y')^2}{N}}$ evaluating the values $(Y)_1^N$ and $(Y')_1^N$.

Aortic valve area derived from the conservation of mass

The (**Gorlin equation**) was set to be a gold standard to compute aortic valve area (AVA) with pressure drop measured by catheter and all Doppler diagnostic methods were than correlated with its values, see (Berger et al., 1984; Kosturakis et al., 1984; Warth et al., 1984; Currie et al., 1985; Smith et al., 1986; Burwash et al., 1993; Fischer et al., 1995). Tab. 3.2 shows the different results in evaluating AVA obtained by the non-invasive Doppler measurements and those obtained by the Gorlin formula. Three formulas are used, the AVA obtained by (Kosturakis et al., 1984) is derived by modification of the (**Gorlin equation**). The other two formulas are based only on the continuity equation without conceptual error in the formula derivation - they are limited only by the measurement errors and the "deviations may not always be due to inadequacies of the Doppler methods: they could also be caused by limitations in the Gorlin formula".(Fischer et al., 1995)

study	formula to be proven*	N**	result
(Kosturakis et al., 1984)	$AVA = \frac{Q}{44.5 \cdot 2 v_2}$	14	errors*** from 0 to 37.5%, mean value $19.2\% \pm 13.4\%$
(Warth et al., 1984)	$AVA = \frac{Q}{v_2}$	16	errors from 0% to 23.3%, mean value $9.5\% \pm 6.8\%$
(Fischer et al., 1995)	$AVA = \frac{v_1 \cdot area_1}{v_2} v_2$ $AVA_{\text{Kosturakis}}$ AVA_{Warth}	100	mean difference always in 95% confidence interval; differences in individual patients' measurements of AVA by the three Doppler techniques varied by up to $0.56\,\text{cm}^2$ compared with values obtained by heart catheterisation. On average, values obtained from Doppler echocardiographic methods lay up to 51% below and 78% above those obtained by heart catheterisation.

Table 3.2: Studies evaluating AVA obtained by the non-invasive Doppler measurements. *formulas for AVA were compared with (**Gorlin equation**); **number of people included in the study, the first one was performed on children; ***$error = \frac{abs(AVA_{\text{Gorlin}} - AVA_{\text{Doppler}})}{\max(AVA_{\text{Gorlin}}, AVA_{\text{Doppler}})} \cdot 100\%$; ****r=correlation coefficient, SEE = standard error in estimation computed as SEE $= \sqrt{\frac{\sum_1^N (Y - Y')^2}{N}}$ evaluating the values $(Y)_1^N$ and $(Y')_1^N$.

Calculation of AVA through the (**Gorlin equation**) or its modification based on other simplifications is strongly limiting. In the next section, we will present the assumptions leading to the Bernoulli equation.

3.2 Derivation of assumptions leading to the justification of using the Bernoulli equation

In this section we will calculate the relation between the pressure drop and dissipative and kinetic energy. We will then rigorously derive assumptions which lead to Bernoulli equation, direct proportion between the pressure drop, kinetic energy and dissipation.

Let us assume oscillatory unsteady flow at two cross sections of the tube with stenosis. The computational domain Ω is assumed to be a part of tube with stenosis limited by

the cross-sections Γ_{in} and Γ_{out}. For the three sections in Fig. 3.2, labeled 1, 2, 3, we will use the notation Γ_1, Γ_2, Γ_3, respectively. Γ_{in} will be always the cross-section Γ_1. We will distinguish two situations according to the Γ_{out}:

- **Situation 1**: $\Gamma_{in} = \Gamma_1$, $\Gamma_{out} = \Gamma_3$, the resulting pressure difference will be as usually called "transvalvular pressure difference",

- **Situation 2**: $\Gamma_{in} = \Gamma_1$, $\Gamma_{out} = \Gamma_2$, this results in maximal pressure difference, see Fig. 3.1.
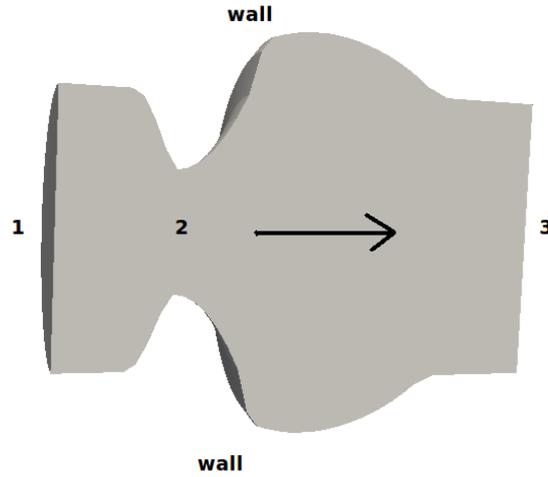
Figure 3.2: Schema of the computational domain representing the symmetric stenosis.

The flow is supposed to be described by the Navier-Stokes equations for incompressible fluid in bulk, i.e.,

$$\rho_* \left(\frac{\partial \mathbf{v}}{\partial t} + (\nabla \mathbf{v}) \mathbf{v} \right) - \operatorname{div} \left(2\mu_* \mathbf{D}(\mathbf{v}) \right) + \nabla p = \mathbf{0} \qquad \text{in } \Omega \qquad (3.2)$$
$$\operatorname{div} \mathbf{v} = 0$$

and is supposed to meet the following type of boundary conditions on the wall: either

$$\mathbf{v} = \mathbf{0} \qquad \text{on } \Gamma_{wall} \qquad (3.3)$$

or

$$\mathbf{v} \cdot \mathbf{n} = 0 \quad \text{and} \quad (\mathbf{T}\mathbf{n})_\tau = \mathbf{0} \qquad \text{on } \Gamma_{wall} \qquad (3.4)$$

53

where $(\mathbf{z})_\tau$ is a tangential part of the vector $\mathbf{z}$, namely

$$(\mathbf{z})_\tau = \mathbf{z} - [\mathbf{z} \cdot \mathbf{n}]\, \mathbf{n}.$$

The equation (3.3) represents the no-slip boundary conditions, the equation (3.4) represents the fact that flows are (perfectly) slipping along the wall.

Taking the scalar product of the first equation in (3.2) and $\mathbf{v}$, and using $\operatorname{div} \mathbf{v} = 0$ we obtain

$$\frac{\partial}{\partial t}\left(\rho_* \frac{|\mathbf{v}|^2}{2}\right) + \operatorname{div}\left(\rho_* \frac{|\mathbf{v}|^2}{2}\mathbf{v} - 2\mu_*\mathbf{D}(\mathbf{v})\mathbf{v}\right) + 2\mu_*|\mathbf{D}(\mathbf{v})|^2 + \operatorname{div}(p\mathbf{v}) = 0. \qquad (3.5)$$

Indeed, eq.(3.5) can be written as

$$\rho_*\left(\frac{\partial \mathbf{v}}{\partial t}\right)\cdot\mathbf{v} + \rho_*\left(\nabla\mathbf{v}\right)\mathbf{v}\cdot\mathbf{v} + \rho_*\frac{|\mathbf{v}|^2}{2}\operatorname{div}\mathbf{v} - \operatorname{div}\left(2\mu_*\mathbf{D}(\mathbf{v})\right)\cdot\mathbf{v} +$$
$$- 2\mu_*\mathbf{D}(\mathbf{v})\cdot\nabla\mathbf{v} + 2\mu_*\mathbf{D}(\mathbf{v})\cdot\mathbf{D}(\mathbf{v}) + p\operatorname{div}\mathbf{v} + \nabla p\cdot\mathbf{v} = 0. \qquad (3.6)$$

We now conclude from (3.5), upon integrating it over Ω, and using the Gauss theorem, that

$$\frac{d}{dt}Ek(t) + Edis(t) = -\int_{\partial\Omega} \rho_*\frac{|\mathbf{v}|^2}{2}\left(\mathbf{v}\cdot\mathbf{n}\right) + 2\mu_*\mathbf{D}(\mathbf{v})\cdot\left(\mathbf{v}\otimes\mathbf{n}\right) - p\left(\mathbf{v}\cdot\mathbf{n}\right)\, dS\,, \qquad (3.7)$$

where $Ek(t)$ and $Edis(t)$ denote the total **kinetic** and **dissipated energy** over Ω, i.e.,

$$Ek(t) := \int_\Omega \rho_*\frac{|\mathbf{v}|^2}{2}\, dx$$
$$Edis(t) := \int_\Omega 2\mu_*|\mathbf{D}(\mathbf{v})|^2\, dx. \qquad (3.8)$$

The both boundary conditions on the wall (3.3) and (3.4), symmetry of $\mathbf{D}(\mathbf{v})$ and the fact that $\mathbf{D}(\mathbf{v})\cdot(\mathbf{v}\otimes\mathbf{n}) = \mathbf{D}(\mathbf{v})\cdot(\mathbf{n}\otimes\mathbf{v}) = \mathbf{D}(\mathbf{v})\mathbf{n}\cdot\mathbf{v}$ gives us

$$-\int_{\Gamma_{wall}} \rho_*\frac{|\mathbf{v}|^2}{2}\left(\mathbf{v}\cdot\mathbf{n}\right) - p\left(\mathbf{v}\cdot\mathbf{n}\right) +$$
$$+ 2\mu_*\left[\left(\mathbf{D}(\mathbf{v})\mathbf{n}\right)_\tau + \left(\mathbf{D}(\mathbf{v})\mathbf{n}\right)_n\right]\cdot\left((\mathbf{v}\cdot\mathbf{n})\mathbf{n} + \mathbf{v}_\tau\right)\, dS = 0\,, \qquad (3.9)$$

and thus the boundary integral on the right hand side of (3.7) is calculated only over the input and output planes.

Consequently, we obtain from conservation of mass that

$$\int_{\Gamma_{in}} \mathbf{v} \cdot \mathbf{n} \, dS = - \int_{\Gamma_{out}} \mathbf{v} \cdot \mathbf{n} \, dS. \tag{3.10}$$

This is motivated by the fact that div $\mathbf{v} = 0$ in Ω and $\mathbf{v} \cdot \mathbf{n} = 0$ on Γ_{wall}. Then

$$\text{div } \mathbf{v} = 0 \Rightarrow 0 = \int_{\Omega} \text{div } \mathbf{v} = \int_{\partial\Omega} \mathbf{v} \cdot \mathbf{n} \, dS = \int_{\Gamma_{in}} \mathbf{v} \cdot \mathbf{n} \, dS + \int_{\Gamma_{out}} \mathbf{v} \cdot \mathbf{n} \, dS.$$

Recall that if the flow in a straight infinite pipe is supposed to fulfill the condition (3.4) on Γ_{wall}, then the resulting velocity is of the form of flow constant in time, it means $\mathbf{v}(x, y, z, t) = \big(0, 0, \omega(t)\big)$ where $\omega(t)$ is constant for all x, y, z for given time t.

Equation (3.7) represents general balance of energy in part of the vessel, including inflow and outflow, and can be used as a starting point for a discussion concerning conversion of different form of energy, and can provide more rigorous derivation of simplifying equations than this based on Bernoulli principle.

In the next section we will present the assumptions under which the right hand side of eq. (3.7) is proportional to pressure drop. Then we will calculate the formula for kinetic energy and dissipation under more realistic assumptions in the last section.

Assumptions leading to the proportional relationship between pressure drop, dissipation and kinetic energy

Several assumptions will be made in what follows. We will specify them as clearly as possible and label them **(A1)-(A3)**.
Without loss of generality, we also can assume that valve is situated at the z-axis position and the outward normal to the inlet and outlet sections are

$$\begin{aligned} \mathbf{n}_{in} &= (0,\, 0,\, -1), \\ \mathbf{n}_{out} &= (0,\, 0,\, 1). \end{aligned} \tag{A0}$$

(A1): First of all, we assume that the pressure is uniform at Γ_{in} and Γ_{out} for given time, i.e.

$$\begin{aligned} p(x, y, t) &= p^{in}(t) & &\text{on } \Gamma_{in}, \\ p(x, y, t) &= p^{out}(t) & &\text{on } \Gamma_{out}. \end{aligned} \tag{A1}$$

Combining the assumptions (**A0**) and (**A1**) with eq. (3.9) and (3.10) we get

$$\int_{\partial\Omega} p\mathbf{v} \cdot \mathbf{n} \, dS = \int_{\Gamma_{in}} p\mathbf{v} \cdot \mathbf{n} \, dS + \int_{\Gamma_{out}} p\mathbf{v} \cdot \mathbf{n} \, dS = p^{in} \int_{\Gamma_{in}} \mathbf{v} \cdot \mathbf{n} \, dS +$$
$$+ p^{out} \int_{\Gamma_{out}} \mathbf{v} \cdot \mathbf{n} \, dS = (p^{in} - p^{out}) \int_{\Gamma_{in}} \mathbf{v} \cdot \mathbf{n} \, dS. \tag{3.11}$$

The equation (3.7) now becomes to be of the form

$$
-\int_{\Gamma_{in}} \mathbf{v} \cdot \mathbf{n}\, dS(p^{in} - p^{out}) + \frac{d}{dt} Ek(t) + Edis(t) =
$$

$$
= -\int_{\Gamma_{in} \cup \Gamma_{out}} \rho_* \frac{|\mathbf{v}|^2}{2} (\mathbf{v} \cdot \mathbf{n}) + 2\mu_* \mathbf{D}(\mathbf{v}) \cdot (\mathbf{v} \otimes \mathbf{n})\, dS. \tag{3.12}
$$

(A2): We assume that the flow velocity at the cross sections Γ_{in} and Γ_{out} is of the form

$$
\mathbf{v} = (0,\, 0,\, \omega) \tag{A2}
$$

and the blood is supposed to flow in z coordinate direction. It corresponds to the assumption of the Bernoulli principle that flow is laminar and streamlined. Note that for the stenotic valve, specially for **Situation** 1 defined later, this is not the case, because there is recirculation enforced by the pressure in aorta. The both cases are shown in the Fig. 3.3.
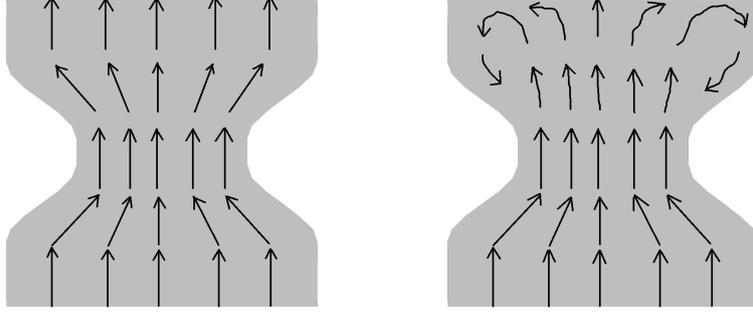
Figure 3.3: Streamlined flow and flow with recirculation in aortic root.

This assumption, incorporated in eq. (3.12) with respect to eq. (**A0**), yields to

$$
(p^{in} - p^{out}) \int_{\Gamma_{in}} \omega\, dS + \frac{d}{dt} Ek(t) + Edis(t) =
$$

$$
- \int_{\Gamma_{out}} \rho_* \frac{(\omega)^3}{2}\, dS + \int_{\Gamma_{in}} \rho_* \frac{(\omega)^3}{2}\, dS - 2 \int_{\Gamma_{out}} \mu_* \frac{\partial \omega}{\partial z} \omega\, dS + 2 \int_{\Gamma_{in}} \mu_* \frac{\partial \omega}{\partial z} \omega\, dS\,. \tag{3.13}
$$

(A3): Finally, velocity ω is uniform in the neighborhood of Γ_{in} and Γ_{out} for given time, i.e.

$$\omega(x, y, t) = \omega^{in}(t) \qquad \& \qquad \frac{\partial \omega}{\partial z} = 0 \qquad \text{on } \Gamma_{in},$$
$$\omega(x, y, t) = \omega^{out}(t) \qquad \& \qquad \frac{\partial \omega}{\partial z} = 0 \qquad \text{on } \Gamma_{out}. \tag{A3}$$

This leads to the fact that last two integrals in eq. (3.13) vanish. We can also take the constants outside the remaining integrals of the right hand side of eq. (3.13) and get

$$\omega^{in}|\Gamma_{in}| \left(p^{in} - p^{out}\right) + \frac{d}{dt}Ek(t) + Edis(t) =$$
$$- \rho_* \frac{(\omega^{out})^3}{2}|\Gamma_{out}| + \rho_* \frac{(\omega^{in})^3}{2}|\Gamma_{in}|. \tag{3.14}$$

Note that this assumption is more simplifying than replacement of the integral by the area of the input/output plane multiplied by mean value of the integrand. Defining $\omega^{in}(t) = \frac{1}{|\Gamma_{in}|} \int_{\Gamma_{in}} \omega \, dS$ does not lead to the vanishing of the integral over Γ_{in} containing the function of ω.

Finally, we will distinguish between the **Situation 1** and **Situation 2**.

Situation 1: Since the area of Γ_{in} and the area of Γ_{out} are similar, $|\Gamma_3| \sim |\Gamma_1|$, we conclude from (**A3**) and (3.10) that $\omega^{in}(t) = \omega^{out}(t)$ and consequently we get the pressure difference proportional to the energy loss, namely

$$p^{in} - p^{out} = -\frac{1}{\omega^{in}|\Gamma_{in}|} \left(\frac{d}{dt}Ek(t) + Edis(t)\right). \tag{3.15}$$

Situation 2: Since $|\Gamma_2| < |\Gamma_1|$, we will suppose that there is a constant $C = \frac{|\Gamma_1|}{|\Gamma_2|} > 1$. Then from conservation of mass, eq. (3.10), we have also $\omega^{out} = C\omega^{in}$. Eq. (3.14) than become

$$p^{in} - p^{out} = -\frac{1}{\omega^{in}|\Gamma_{in}|} \left(\frac{d}{dt}Ek(t) + Edis(t)\right) - \frac{\rho_*}{2}(\omega^{in})^2(C^2 - 1). \tag{3.16}$$

This situation does not justify the use of Bernoulli equation. Let us assume the stenosis with 80% narrowing, i.e. $|\Gamma_2| = 20\%|\Gamma_1|$. Then $C = 5$. For $\rho_* \sim 10^3 \frac{\text{kg}}{\text{m}^3}$ and $\omega^{in} \sim 0.5\frac{\text{m}}{\text{s}}$ the last term equals to the value $3000 \frac{\text{kg}}{\text{m s}^2} = 3000$ Pa ~ 22.5 mmHg. In such a severe stenosis, the pressure difference $p^{in} - p^{out}$ can be more than 40 mmHg and the last term in eq. (3.16) should be its significant source.

Derivation of relationship between pressure drop, dissipation and kinetic energy under more realistic condition

Let us come back to the equations (3.7)-(3.9) and consider inflow and outflow boundary conditions given in this thesis, namely in the section 3.3, without the backflow stabilization:

$$
\begin{aligned}
\mathbf{v}_{ref} &= \left(0, 0, \omega^{in}\right) && \text{on } \Gamma_{in}, \\
\mathbf{T}\mathbf{n} &= -\overline{P(t)}\mathbf{n} && \text{on } \Gamma_{out},
\end{aligned}
\tag{3.17}
$$

where $\omega^{in}(x, y, t) : \Gamma_{in} \times [0, T] \to \mathcal{R}$ and $P(t) : [0, T] \to \mathcal{R}$ are prescribed functions.

Outflow condition in (3.17) results in

$$
\begin{aligned}
0 &= -\int_{\Gamma_{out}} \mathbf{T}\mathbf{n} \cdot \mathbf{v}_{ref} + \overline{P(t)}\mathbf{n} \cdot \mathbf{v}_{ref}\, dS = \\
&= -\int_{\Gamma_{out}} \left(-p\left(\mathbf{v} \cdot \mathbf{n}\right) + 2\mu_* \mathbf{D}(\mathbf{v}) \cdot (\mathbf{v} \otimes \mathbf{n})\right) dS - \int_{\Gamma_{out}} \overline{P(t)}\mathbf{n} \cdot \mathbf{v}_{ref}\, dS.
\end{aligned}
\tag{3.18}
$$

Thus we have (compare with eq.(3.7))

$$
\begin{aligned}
-\int_{\Gamma_{out}} \rho_* \frac{|\mathbf{v}|^2}{2}\left(\mathbf{v} \cdot \mathbf{n}\right) + 2\mu_* \mathbf{D}(\mathbf{v}) \cdot (\mathbf{v} \otimes \mathbf{n}) - p\left(\mathbf{v} \cdot \mathbf{n}\right) dS = \\
= -\int_{\Gamma_{out}} \rho_* \frac{|\mathbf{v}|^2}{2}\left(\mathbf{v} \cdot \mathbf{n}\right) dS + \int_{\Gamma_{out}} \overline{P(t)}\mathbf{n} \cdot \mathbf{v}_{ref}\, dS
\end{aligned}
\tag{3.19}
$$

For inflow condition we know $\frac{\partial \omega}{\partial z} = 0$. Inserting (3.19) into the (3.7) we then obtain

$$
\begin{aligned}
\frac{d}{dt} Ek(t) + Edis(t) &= -\int_{\Gamma_{out}} \rho_* \frac{|\mathbf{v}|^2}{2}\left(\mathbf{v} \cdot \mathbf{n}\right) dS + \overline{P(t)} \int_{\Gamma_{out}} \mathbf{v}_{ref} \cdot \mathbf{n}\, dS \\
&\quad -\int_{\Gamma_{in}} \rho_* \frac{|\mathbf{v}|^2}{2}\left(\mathbf{v} \cdot \mathbf{n}\right) dS + \int_{\Gamma_{in}} p\, \mathbf{v} \cdot \mathbf{n}\, dS.
\end{aligned}
\tag{3.20}
$$

Assuming $p^{in} = p^{in}(t)$ to be a constant on Γ_{in} for fixed time, denoting $p^{out} = \overline{P(t)}$ and using the conservation of mass, eq. (3.10), we get

$$
p^{in} - p^{out} = -\frac{1}{\omega^{in}|\Gamma_{in}|}\left(\frac{d}{dt} Ek(t) + Edis(t) + \int_{\Gamma_{in} \cup \Gamma_{out}} \rho_* \frac{|\mathbf{v}|^2}{2}\left(\mathbf{v} \cdot \mathbf{n}\right)\right).
\tag{3.21}
$$

where Γ_{out} can be both, Γ_2 or Γ_3, in opposite to the eqations (3.15) or (3.16), respectively.

In the next two sections we will introduce the computational model. In section 3.5 the pressure difference, kinetic energy and dissipated energy will be derived directly from the computed $\mathbf{v}$ and p without using the relation (3.21). This relation will be compared with the results obtained by continuum mechanics approach in section 5.3.

3.3 Determination of dissipated energy using continuum mechanics approach

In this section we will focus on aortic valve stenosis as a case example to apply the continuum mechanics approach. Specifically, for a pre-specified left ventricular outflow tract velocity profile and ascending thoracic aortic pressure profile as inflow and outflow boundary conditions we will determine pressure, velocity, kinetic energy and energy dissipation as functions of the entire spatial field (left ventricular outflow tract, aortic valve/root, and proximal ascending thoracic aorta) and time.

In this section we will derive the model for the flow of the incompressible Newtonian fluid in the three-dimensional narrowed channel representing the geometry of the stenotic valve under the assumption of rigid walls.

Even if the fluid were flowing in a vessel that has a rigid boundary, the problem is quite challenging as we have to solve the problem wherein locally the Reynolds number could be large, the geometry of the flow domain complex, and the flow unsteady. The flow can be locally turbulent and it can also separate. Moreover, even if we were to simplify the problem to that of the flow of a Navier-Stokes fluid in such geometry, the problem is quite daunting. In the case of flow across a valve, the material in question is blood. While blood is a complex mixture of plasma, red and white blood cells, platelets, lipoproteins, ions, etc., undergoing a big amount of biochemical reactions, fibrinolysis, coagulation and lysis, the flow of blood under normal conditions in large vessels can be approximated reasonably well as a flow of classical linearly viscous fluid, that is a fluid whose response is characterized by the Navier-Stokes constitutive relation, though in small blood vessels, blood displays non-Newtonian behavior by exhibiting shear-thinning (Chien et al., 1966; Yeleswarapu et al., 1998), stress relaxation (Thurston, 1979), normal stress differences, etc. In very small blood vessels such as capillaries as the diameter of the red blood cells are of comparable or even larger than the diameter of the blood vessel, even using a continuum fluid model for blood would be totally inappropriate. However, in the problem of flow across a diseased valve, even in the case of acute stenosis, the flow of blood can be described by the classical incompressible Navier-Stokes fluid as was discussed in chapter 1.

Let us assume oscillatory unsteady flow described by the Navier-Stokes equations for an incompressible fluid, namely

$$
\rho_* \left(\frac{\partial \mathbf{v}}{\partial t} + (\nabla \mathbf{v}) \mathbf{v} \right) - \operatorname{div} \left(2\mu_* \mathbf{D}(\mathbf{v}) \right) + \nabla p = \mathbf{0}
$$
$$
\operatorname{div} \mathbf{v} = 0 \qquad \text{in } \Omega \qquad (3.22)
$$
$$
\mathbf{T} = -p\mathbf{I} + 2\mu_* \mathbf{D}
$$

where $\mathbf{T}$ is the Cauchy stress tensor, $p = -\frac{1}{3}(\operatorname{tr} \mathbf{T})$ is the mean normal stress that is usually

referred to as the mechanical pressure, $\mathbf{v}$ is the velocity of the fluid, $\mathbf{D} = \frac{1}{2}\left(\nabla\mathbf{v} + \left(\nabla\mathbf{v}\right)^T\right)$, μ_* denotes the constant dynamic viscosity and $\nu_* = \frac{\mu_*}{\rho_*}$ is the kinematic viscosity. We will use the subscript $*$ for constants. The list of constants and their values are shown in chapter 2 in Tab. 2.1. The computational domain $\Omega \subset \mathcal{R}^3$ will be specified later.

In the case of a fluid characterized by the Navier-Stokes constitutive relation, the dissipation $Edis$ is given by

$$Edis = \mathbf{T} \cdot \mathbf{D}, \tag{3.23}$$

which in virtue of incompressibility and form of the stress relation (see $(3.22)_2$ and $(3.22)_3$) simplifies to

$$Edis = 2\mu_*\mathbf{D} \cdot \mathbf{D}. \tag{3.24}$$

In this text, we focus on computations of the pressure difference, kinetic energy and dissipation within/across the geometry representing the stenotic aortic valve. We depict the computed velocity field in the region of the stenosis and distal to it, where secondary flows and recirculation occur. Recirculation and unsteady flow are the major reasons why Bernoulli principle cannot be applied in this kind of problems.

In principle, since we know the velocity field pointwise due to experimental measurements, we can directly determine the rate of dissipation given by (3.24). In the case to be studied here, i.e. flows in aortic valve stenosis, the minimum focus of the known velocity field is the left ventricular outflow tract, i.e. we assume to know the reasonable approximation of the inflow velocity profile.

The pressure difference, kinetic energy and dissipation will be shown in geometries representing aortic valve with symmetric stenosis of severity 50%, 60%, 70% and 80% where severity is given as the formula (3.25). The geometry is limited by the assumption that aortic walls are non-deformable, but with reasonable approximations of the real geometry. The formulation of the boundary conditions used in the model with physiologically relevant pressure and flow profiles follows. Finally, in section 3.5, we will discuss the results achieved from three-dimensional computations where Navier-Stokes equations are used.

3.3.1 Geometry

The geometry of the computational domain Ω should represent the aortic valve which is highly deformable viscoelastic tissue located between the left ventricle and aorta.

The aortic valve, comprised of three leaflets, is shown in the diagram 3.4 as being attached to the aortic root circumferentially, forming a circumferentially thickened ridge of fused leaflet/aortic tissue termed the aortic valve annulus. The annulus is a three-dimensional crown-like structure, as opposed to a planar structure. In addition, the diameter of the base of the annulus (ventriculo-aortic junction) is smaller than the diameter of the aortic root-ascending thoracic aortic junction (a.k.a. sinotubular junction), such that the annulus is within a conic section. Two-point of view are shown in diagram 3.4, the geometry approximation used for computations and located on the z axis is described and shown in

Fig. 3.5, while the geometry dimensions are shown in Fig. 3.6. All these figures represent the healthy (non-stenotic) valve.
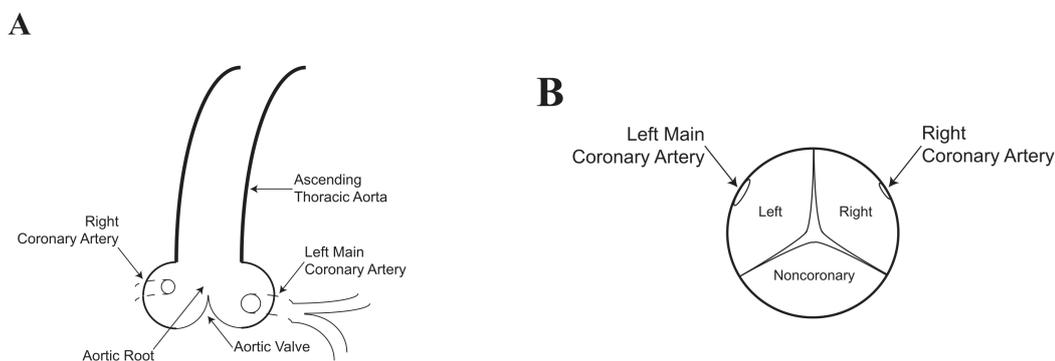

Figure 3.4: **Anatomy of the human aortic valve/root complex.** The aortic valve is a viscoelastic tissue composed of three leaflets which are opening and closing during a cardiac cycle. **A.** Long-axis view. In this view, not all three leaflets can be seen. Rather, cross sections of the right and left leaflet are shown. The view demonstrates the valve during either systolic isovolumetric contraction, or either phase of diastole, i.e. opening or closing phase. **B.** Short-axis view. In this view, all three leaflets can be visualized. This view is an approximate representation of the surgeons view of the aortic valve/root complex when the ascending thoracic aorta has been transected proximally. The view also demonstrates the valve during opening or closing phase.
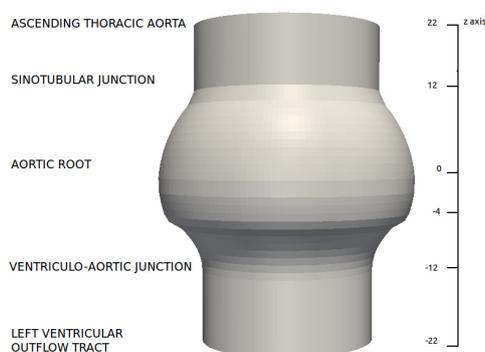
Figure 3.5: **The description of the geometry.** The aortic root is situated between $z = -12$ and $z = 12$, where $z = -12$ corresponds to the ventriculo-aortic junction and $z = 12$ to the sinotubular junction. $z = 0$ corresponds to a widest place of aortic root. The part from $z = -22$ to $z = -12$ is supposed to be 1cm part of the left ventricular outflow tract, the part between $z = 12$ and $z = 22$ is 1 cm part of ascending thoracic aorta.
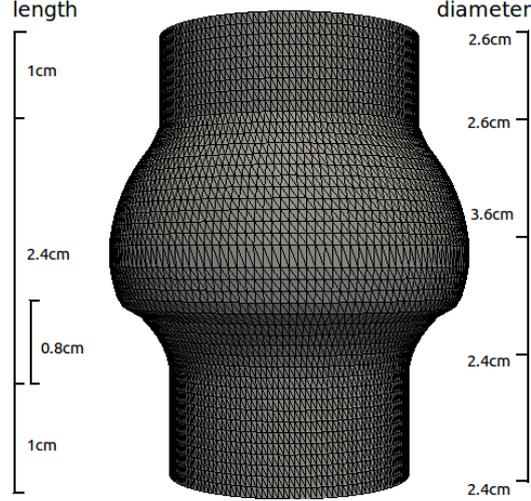
Figure 3.6: **The geometry dimensions.** Left ventricular outflow tract, aortic root and proximal ascending thoracic aortic dimensions for the healthy case with a rigid wall assumption: The length of the aortic root is 2.4 cm here, the part of the aortic root which should be affected by the stenosis is set to 0.8 cm. The length of the part representing left ventricle junction is 1cm, the length of the cylinder representing the part of the ascending aorta is 1cm. The diameter of the sinotubular junction is 2.6 cm, the diameter of the ventriculo-aortic junction 2.4 cm. Finally the maximal diameter of the geometry is 3.6 cm.

In the following, we will be mostly interested in the stenotic/narrowed geometries. The computational meshes are shown in Fig. 3.7. Firstly, there is a geometry represented aortic valve with symmetric severity 50%, then 60%, 70% and finally 80%. The severity, expressing the level of narrowing, is given as a relation between the area of the healthy part, approximated here by a circle with radius R, and the area of the stenotic part, approximated by a circle with radius r, i.e.,

$$severity = (1 - \frac{area_r}{area_R}) \cdot 100\% \tag{3.25}$$

such that the more narrowed/stenotic geometry has a higher severity.
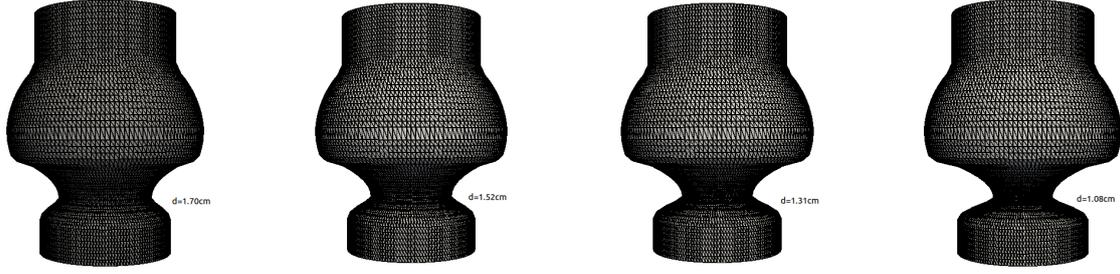
Figure 3.7: **Geometry representing the stenotic valve with a different severity.** Severity is assumed to be equal $1 - \frac{\pi d^2}{\pi D^2}$, where $D = 2.4\,\text{cm}$ is the original diameter of the valve without stenosis and d represents the diameter of the narrowed geometry. For 50% stenosis diameter $d = 1.7\,\text{cm}$, for 60% stenosis $d = 1.52\,\text{cm}$, for 70% stenosis $d = 1.31\,\text{cm}$ and finally $d = 1.07\,\text{cm}$ for 80% stenosis.

3.3.2   Boundary conditions

In a given domain $\Omega \subset \mathbf{R}^3$, representing the simplified aortic valve, the velocity $\mathbf{v}$ and pressure p satisfy eq. (3.22). Let us consider the boundary of the domain $\partial\Omega$, which consists of three parts. Γ_{wall} denotes the walls and Γ_{in}, Γ_{out} are the inlet and outlet, respectively. In order to be physiologically and clinically relevant, first we consider the known pressure distal to the aortic valve, in the proximal ascending thoracic aorta, (as a Neumann boundary condition on the outlet) and known velocity of blood ejected by, and flowing out of, the left ventricle (as a Dirichlet boundary condition on the inlet). On rigid walls, we consider the no-slip boundary conditions, as opposite to the slip boundary condition studied in chapter 5. Hence,

$$
\begin{aligned}
\mathbf{v} &= \mathbf{0} & &\text{on } \Gamma_{wall}, \\
\mathbf{v} &= \mathbf{v}_{in} & &\text{on } \Gamma_{in}, \\
\mathbf{T}\mathbf{n} - \frac{1}{2}\rho_*(\mathbf{v}\cdot\mathbf{n})_-\mathbf{v} &= -\overline{P(t)}\mathbf{n} & &\text{on } \Gamma_{out}
\end{aligned}
\tag{3.26}
$$

and initial condition for the velocity is set to

$$
\mathbf{v}(t = 0) = \mathbf{0} \qquad \text{in } \overline{\Omega}. \tag{3.27}
$$

Here, $\mathbf{n}$ represents the unit normal vector to the boundary and $(\mathbf{v}\cdot\mathbf{n})_-$ denotes the negative part of the function $\mathbf{v}\cdot\mathbf{n}$, used as an outflow stabilization term, as was analyzed in (Bertoglio and Caiazzo, 2014). The value for the constant parameters are given in Tab. 2.1.

The velocity $\mathbf{v}_{in}$ is given as a parabolic profile with its magnitude scaled by a time dependent factor, $\overline{V(t)}$, representing the velocity averaged over the inlet plane. The velocity time dependent factor $\overline{V(t)}$ is a curve unique for an individual patient. Here, we used the curve

displayed in Fig. 3.8, in which each cardiac cycle is of 1s length and the systolic ejection period SEP with length 0.3 s is the time during which the aortic valve is considered open; see Fig. 3.9. During the SEP, the velocity initially is $0\frac{m}{s}$ (no flow), increases to v_{max}, and then decreases to $0\frac{m}{s}$ (at which part of the SEP ends). For the purpose of this work, we set $v_{max} = 0.7\frac{m}{s}$ for all geometries.
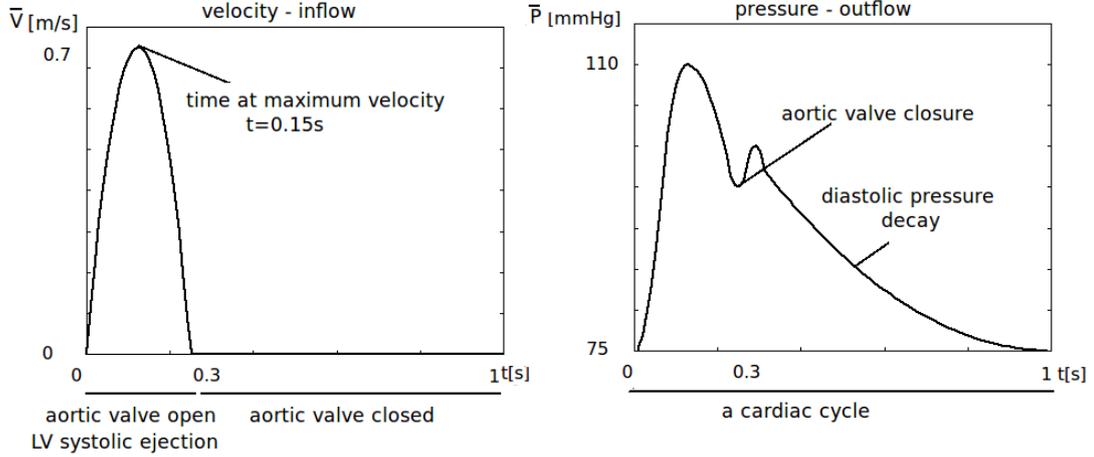

Figure 3.8: The prescribed outlet pressure and inlet velocity functions $\overline{P(t)}$ and $\overline{V(t)}$ as functions of time.

Note that the time-averaged velocity $\mathbf{v}_{\text{TA}} = \int_{\text{SEP}} \mathbf{v}\, dt = \frac{2}{3}\mathbf{v}_{max} = 0.45\frac{m}{s}$, the systolic ejection period SEP $= 0.3$ s, time for maximum velocity is at 0.15 s, and the area of input cross-section $A_{valve} = \pi\frac{D^2}{4} = 4.5\,\text{cm}^2$. The diameter of the input plane is set as $D = 2.4\,\text{cm}$. The corresponding stroke volume SV (volume of the blood ejected by the left ventricle per heart beat) can be then computed from the left ventricular ejection volumetric flow rate F as

$$\text{SV} = \int_{t=0}^{1} \text{F}\, dt = \int_{t=0}^{1} A_{valve} * \overline{V(t)}\, dt = A_{valve} * \text{SEP} * \mathbf{v}_{mean} \doteq 61\,\text{ml}. \qquad (3.28)$$

At the outlet, i.e., the proximal ascending thoracic aorta, we prescribe the pressure mean value $\overline{P(t)}$, which is based on information from measurements in the aorta as a function of time. At the output, recirculation may occur, and can lead to instabilities. We assume that no aortic valve regurgitation is present, and use backflow stabilization used at the outlet as studied in (Bertoglio and Caiazzo, 2014) and (Braack and Mucha, 2014).
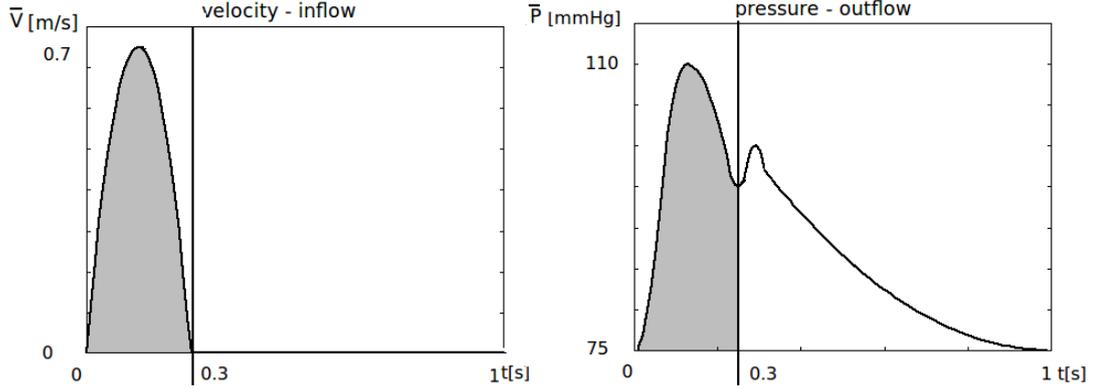
Figure 3.9: Systolic ejection period SEP.

The function $\overline{P(t)}$ can depend on the stenosis severity. As aortic valve stenosis progresses, if and when left ventricular intrinsic systolic function (contractility) decompensates and cannot maintain (i.e., contractility is not high enough) adequate stroke volume in the face of elevated afterload posed by the stenotic valve, systemic arterial hypotension may occur. This occurs, but is uncommon. We have assumed adequate (which must actually be supranormal) left ventricular contractility to maintain stroke volume and distal aortic pressure. Thus, for the purposes of this work, we used the function $\overline{P(t)}$, see Fig. 3.9 (right), such that the peak systolic aortic pressure $p_{max} = 110\,\text{mmHg}$ and the nadir diastolic aortic pressure $p_{min} = 75\,\text{mmHg}$ in all geometries. For better illustration, we use units of millimeters Hg for pressure ($1\,\text{Pa} = 0,0075\,\text{mmHg}$).

3.4 Numerical model and outflow boundary treatment for circulation

In this section we will shortly provide the weak formulation of the problem (3.22)&(3.26) and subsequent discretization. Then we will provide the motivation for the stabilization term when the circulation occurs on the outflow plane Γ_{out}.

Weak formulation

Let us multiply the eq. $(3.22)_1$ by the test function $\mathbf{v}_{test} \in V$ and integrate the results over the domain Ω and over the finite time interval $\text{I} = [0, \text{T}]$. We will also multiply eq. $(3.22)_2$

by the test function $p_{test} \in P$. The functional spaces are defined through

$$V := \left\{ \mathbf{v} \in \mathrm{L}^{\infty}\left(\mathrm{I}, \left[\mathrm{H}^1(\Omega) \right]^3 \right); \quad \mathbf{v} = \mathbf{0} \text{ on } \Gamma_{in} \cup \Gamma_{wall} \right\},$$

$$P := \left\{ p \in \mathrm{L}^2\left(\mathrm{I}, \mathrm{L}^2(\Omega) \right) \right\}. \tag{3.29}$$

Using the per-partes method, we get the weak formulation of the problem. For simplicity we will identify $\mathbf{v}$ with its part having homogeneous Dirichlet boundary condition on Γ_{in}, namely $\mathbf{v} := \mathbf{v} - \mathbf{v}_{in} \in V$. Then the weak formulation of (3.22)&(3.26) can be formulated as follows.

Find $(\mathbf{v}, p)$ in $V \times P$ satisfying for all $(\mathbf{v}_{test}, p_{test}) \in V \times P$:

$$\int_0^T \left[\left(\rho_* \frac{\partial \mathbf{v}}{\partial t}, \mathbf{v}_{test} \right)_\Omega + \left(\rho_* \left(\nabla \mathbf{v} \right) \mathbf{v}, \mathbf{v}_{test} \right)_\Omega + \left(\mathbf{T}, \nabla \mathbf{v}_{test} \right)_\Omega \right] dt +$$

$$- \int_0^T \left(\frac{1}{2} \rho_* \left(\mathbf{v} \cdot \mathbf{n} \right)_- \mathbf{v}, \mathbf{v}_{test} \right)_{\Gamma_{out}} dt = - \int_0^T \left(\overline{P(t)} \mathbf{n}, \mathbf{v}_{test} \right)_{\Gamma_{out}} dt \tag{3.30}$$

$$- \int_0^T \left(\operatorname{div} \mathbf{v}, p_{test} \right)_\Omega dt = 0$$

Finite element discretization

We will identify the domain Ω with its discretization into finite elements. All elements will be tetrahedra.

Then the formulation of (3.30) can be discretized by Taylor-Hood element. The function spaces are

$$\mathbf{v}_h, \mathbf{v}_h^{test} \in V_h := \{ \mathbf{v}_h \in \left[C(\Omega) \right]^3, \ \mathbf{v}_h \mid_K \in \left[\mathrm{P}_2(K) \right]^3 \ \forall K \in \Omega;$$

$$\mathbf{v}_h \mid_E = 0 \ \forall E \in \Gamma_{in} \cup \Gamma_{wall} \}, \tag{3.31}$$

$$p_h, p_h^{test} \in P_h := \left\{ p_h \in C(\Omega), \ p_h \mid_K \in \mathrm{P}_1(K) \ \forall K \in \Omega \right\}.$$

According to the weak formulation (3.30) we will define variational forms

$$B(\mathbf{v}, p, \mathbf{v}_{test}, p_{test}) = \left(\rho_* \left(\nabla \mathbf{v} \right) \mathbf{v}, \mathbf{v}_{test} \right)_\Omega + \left(\mathbf{T}, \nabla \mathbf{v}_{test} \right)_\Omega +$$

$$- \left(\frac{1}{2} \rho_* \left(\mathbf{v} \cdot \mathbf{n} \right)_- \mathbf{v}, \mathbf{v}_{test} \right)_{\Gamma_{out}} - \left(\operatorname{div} \mathbf{v}, p_{test} \right)_\Omega, \tag{3.32}$$

$$F(\mathbf{v}_{test}) = - \left(\overline{P(t)} \mathbf{n}, \mathbf{v}_{test} \right)_{\Gamma_{out}}.$$

Then the finite element formulation of (3.30) is to look for $(\mathbf{v}_h, p_h) \in V_h \times P_h$ such that

$$\int_0^T \left(\rho_* \frac{\partial \mathbf{v}}{\partial t}, \mathbf{v}_{test} \right)_\Omega + B(\mathbf{v}_h, p_h, \mathbf{v}_h^{test}, p_h^{test}) \, dt = \int_0^T F(\mathbf{v}_h^{test}) \, dt \tag{3.33}$$

holds for all $(\mathbf{v}_h^{test}, p_h^{test}) \in V_h \times P_h$ with respect to the definitions (3.31) and (3.32).

Time discretization

Time discretization of the problem (3.33) can be treated by the Crank-Nicholson scheme as defined in chapter 2. Form $L(t)$ from eq. (2.16) then equals to

$$L(t) = B - F \tag{3.34}$$

and the forms B and F are defined in (3.32).

Outflow boundary stabilization term

Due to the stenosis, the recirculation distal to the aortic valve may occur as it is shown in Fig. 3.10. This leads to the backflow occurring on the outflow boundary condition in the short geometry representing the aortic valve. "Backflow instabilities might result in the arise of large nonphysical oscillations near the open boundary, which compromise the feasibility and the reliability of the numerical simulations." (Bertoglio and Caiazzo, 2014) Moreover, the backflow on the boundary condition leads to the $\mathbf{v} \cdot \mathbf{n} < 0$ on Γ_{wall}. We recall the eq. (3.21), the equality between the energy source (inflow) and energy losses (including outflow):

$$\begin{aligned}
\int_{\Gamma_{in}} \rho_* \frac{|\mathbf{v}|^2}{2} (\mathbf{v} \cdot \mathbf{n}) = &-\omega^{in}(t)|\Gamma_{in}| \left(p^{in}(t) - p^{out}(t) \right) \\
&- \frac{d}{dt} Ek(t) - Edis(t) - \int_{\Gamma_{out}} \rho_* \frac{|\mathbf{v}|^2}{2} (\mathbf{v} \cdot \mathbf{n}).
\end{aligned} \tag{3.35}$$

The $\mathbf{v} \cdot \mathbf{n} < 0$ on Γ_{out} in eq. (3.35) can lead to an uncontrolled energy increase during backflow, since this contribution cannot be bounded a priori.
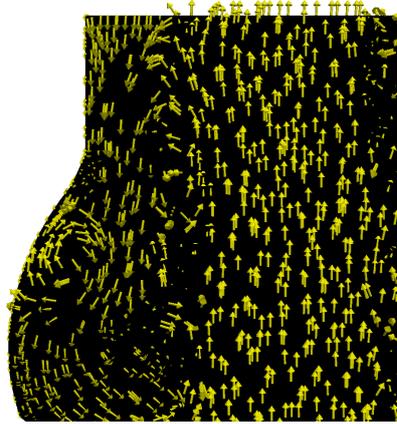
Figure 3.10: Recirculation inside the domain and following backflow on the outflow boundary.

This stabilization term was also analyzed in (Braack and Mucha, 2014). As opposite to the do-nothing condition,

$$(\nabla \mathbf{v} - p\mathbf{I})\mathbf{n} = \mathbf{0} \qquad \text{(do-nothing)}$$

with a constant viscosity coefficient $\nu > 0$, a directional do-nothing condition

$$(\nu \nabla \mathbf{v} - p\mathbf{I})\mathbf{n} - \frac{1}{2}(\mathbf{v} \cdot \mathbf{n})_{-}\mathbf{v} = \mathbf{0} \qquad \text{(directional do-nothing)}$$

was introduced. The additional term guarantees construction of the energy estimate for large data for Navier-Stokes equations. (Braack and Mucha, 2014)

3.5 Numerical computations of the pressure drop and dissipated energy on geometries representing stenotic valve with different narrowing levels

FEniCS software for solving partial differential equations (Logg et al., 2012) was used to compute the problem eq.(3.22) and (3.26) by the finite element method. The time derivatives in the equations were approximated by the Crank-Nicholson scheme. Time interval of systolic ejection period length 0.3s was computed, and an adaptive time step was used. The time step length varies from 1E-2 to 2E-3 for mild stenotic cases with 50% and 60% severity. Because of high velocities in the narrowed part, the length of time step had to be finer in more severe cases. The time step length varies from 1E-3 to 2E-4 for 70% case and from 1E-3 to 5E-5 for 80% .

To show the results, we plot the pressure p_Γ defined in (3.37), dissipation $Edis_\Gamma$ specified in (3.38) and kinetic energy Ek_Γ defined as (3.39) along the centerline for meshes with different severities, see (3.25), namely 50%, 60%, 70% and 80%. The centerline is an axis passing through the vessel; Γ denotes cross-sectional area along the centerline, see Fig. 3.11.

Graphs of pressure, kinetic energy and energy dissipation, at time at maximum velocity, but varying as functions of position, are shown in Fig. 3.13. Similar graphs of time averaged values over the systolic ejection period, but again varying as functions of position, are displayed in Fig. 3.14.

Time averaged value of pressure is calculated over the SEP as

$$p_{\Gamma aver} = \frac{1}{0.3} \int_0^{0.3} p_\Gamma \, dt. \qquad (3.36)$$

Kinetic energy and energy dissipation are calculated similarly.

$$p_\Gamma = \frac{\int_\Gamma p\, dS}{\mathrm{area}(\Gamma)} \qquad (3.37)$$

$$Edis_\Gamma = \frac{2\mu_* \int_\Gamma \mathbf{D} \cdot \mathbf{D}\, dS}{\mathrm{area}(\Gamma)} \qquad (3.38)$$
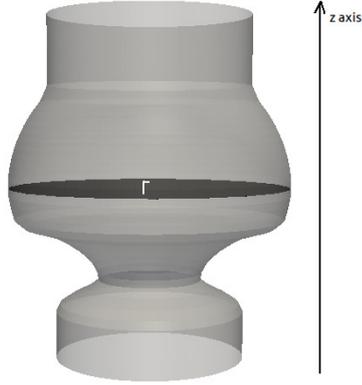
$$Ek_\Gamma = \frac{0.5\rho_* \int_\Gamma \mathbf{v} \cdot \mathbf{v}\, dS}{\mathrm{area}(\Gamma)} \qquad (3.39)$$

Figure 3.11: Cross-section areas Γ along the centerline, which corresponds to the z axis.

Figure 3.12 depicts transvalvular pressure drop as a function of time over a range of stenosis severities. Tables 3.3 and 3.4 display maximum and mean SEP transvalvular pressure drops over the range of stenosis severities. These data are consistent with measured data in (Garcia et al., 2006). Classically, stenoses are thought to cause adverse hemodynamic and other sequelal once stenosis severity is in the range of $70 - 80\%$. Our findings are consistent with this clinical experience.

sev	input pressure [mmHg]	pressure drop [mmHg]
50%	115.6	5.6
60%	124.3	14.3
70%	141.7	31.7
80%	183.3	73.3

sev	input pressure [mmHg]	pressure drop [mmHg]
50%	101.6	3.0
60%	106.1	7.5
70%	115.1	16.5
80%	135.0	36.4

Table 3.3: Computed input integral pressure (i.e. averaged over the input cross-sectional area) and the pressure drop at time at maximum velocity. Output integral pressure was fixed (prescribed as a boundary condition) to $110\,\mathrm{mmHg}$.

Table 3.4: Computed input integral pressure (i.e. averaged over the input cross-sectional area) and the pressure drop as an average value over the SEP. Output integral pressure was fixed (prescribed as a boundary condition) to $98.6\,\mathrm{mmHg}$.
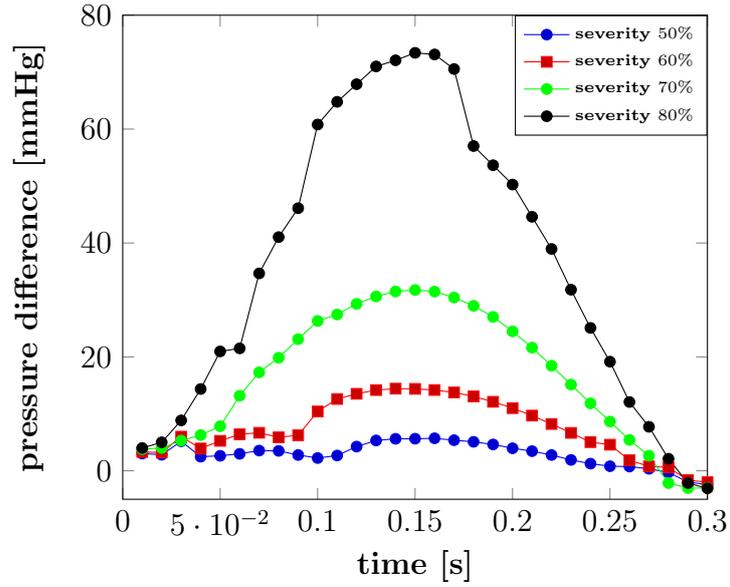
Figure 3.12: Pressure drop across the aortic valve during the SEP, for different degrees of of stenosis. Pressure drop is defined as a difference between the pressure averaged over cross-sectional area of output and pressure averaged over cross-sectional area of input, i.e. the difference between p_Γ at $z = -22$ and p_Γ at $z = 22$.

Figures 3.13 and 3.14 show the variables averaged over cross-sectional area Γ as functions of the z coordinate (see Fig. 3.11), at time $t = 0.15\,\text{s}$, and averaged over the SEP, respectively. Graphs of the time evolution of variables (i.e., as time-varying functions) during the SEP at specified z coordinates are shown in Fig. 3.15. Velocity distribution on a valvular geometry with the severity up to 50% will be shown in section 5.3 in Fig. 5.4-5.9.
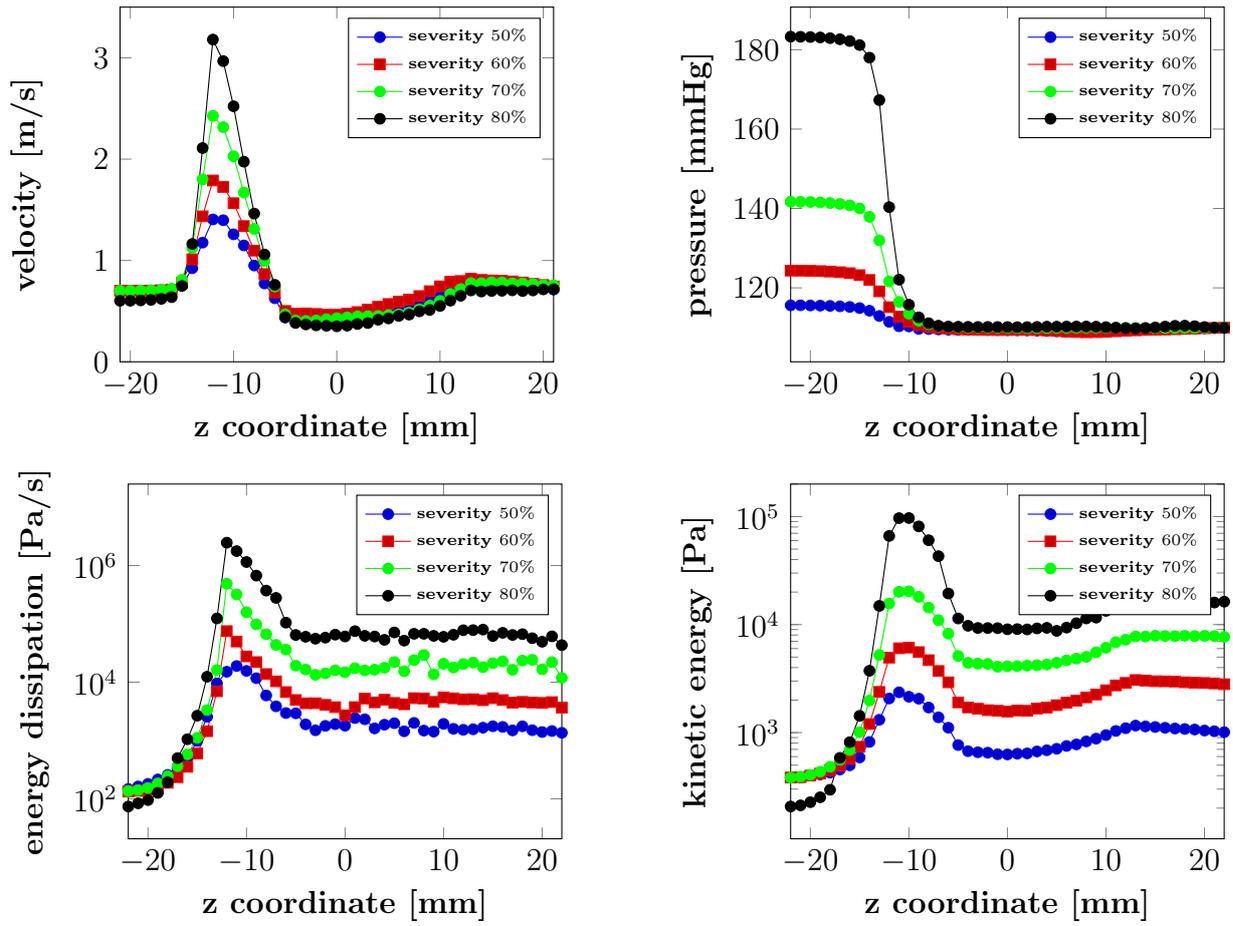
Figure 3.13: Velocity, pressure, kinetic energy and energy dissipation averaged over cross-sectional area Γ, varying as functions of the z coordinate (length), set at the time of maximum velocity ($t = 0.15$ s).
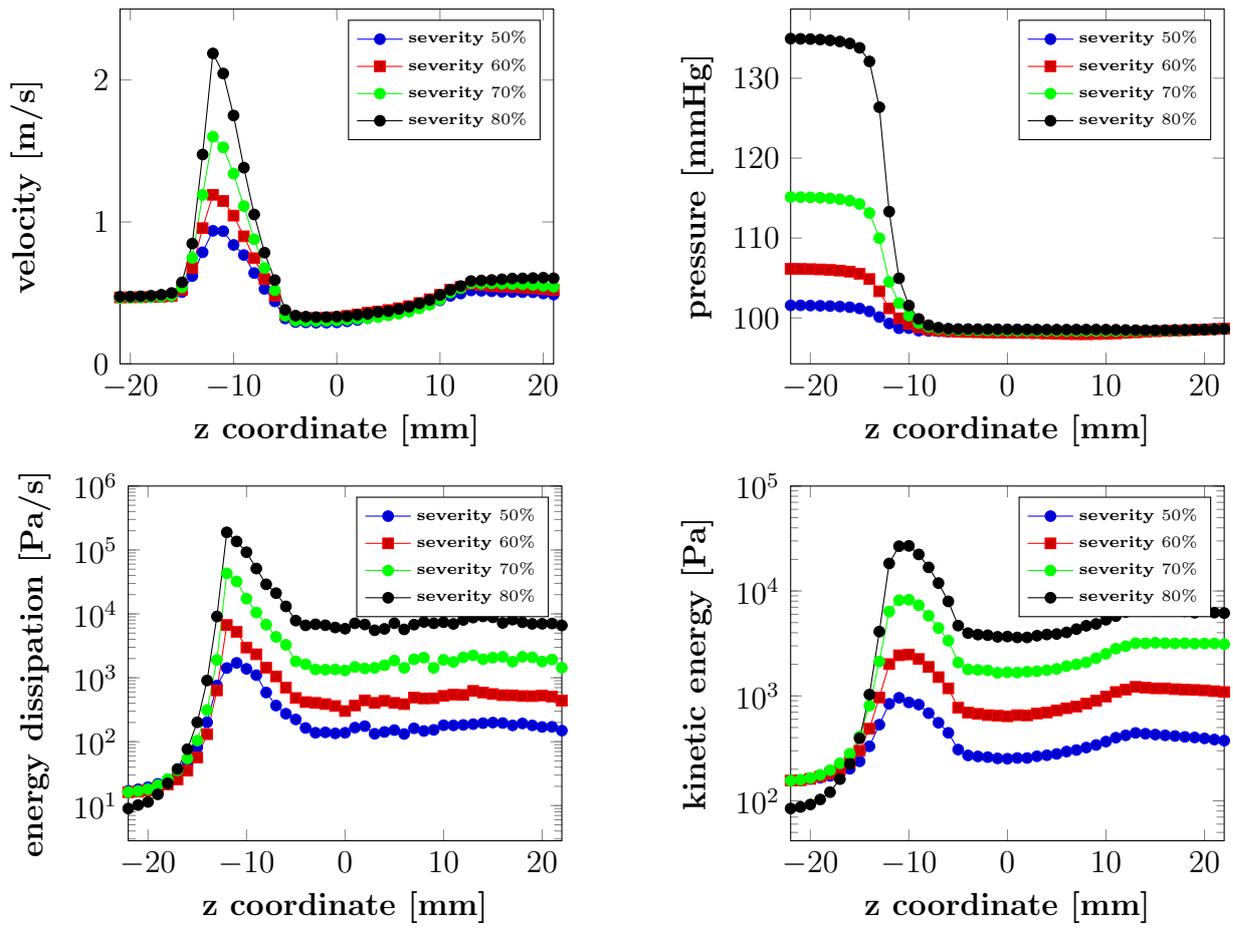
Figure 3.14: Velocity, pressure, kinetic energy and energy dissipation averaged over space (cross-sectional area Γ) and time (SEP), varying as functions of the z coordinate (length).
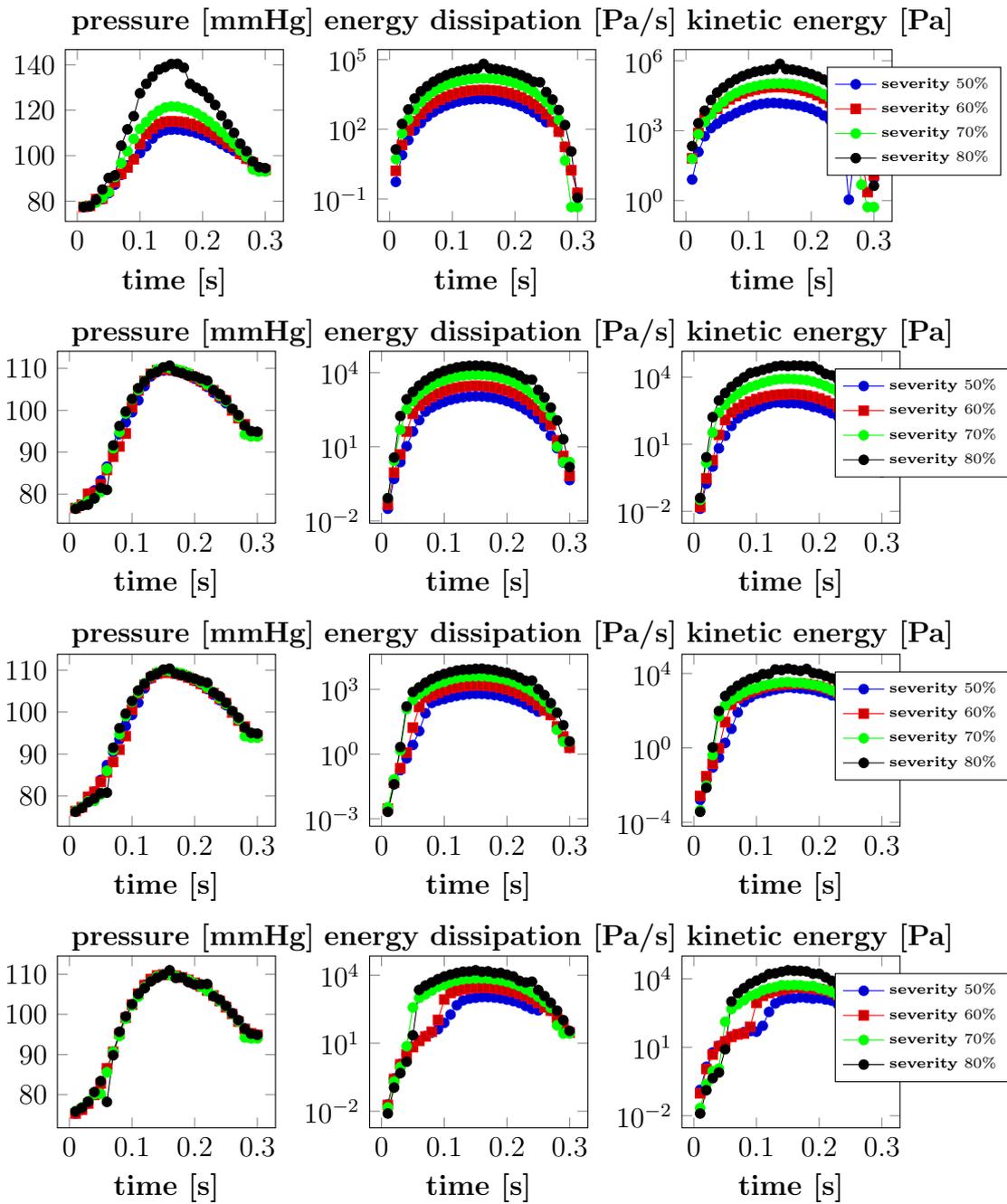
Figure 3.15: Pressure, kinetic energy and energy dissipation averaged over cross sectional area Γ, varying as functions of time; at $z = -12, -6, 0, 12$.

3.6 Conclusion

The existing body of literature and extant work on modeling of cardiovascular blood flow generally is limited by important oversimplifications and frank conceptual errors - both mathematical and mechanical. A need for rigorous mathematical/mechanical modeling of cardiac and vascular function and blood flow thus is required. This work is a substantial shift in modeling approaches to cardiovascular system function from which further progress may be made.

It was shown that the assumptions currently used in medical practice and leading to the Bernoulli equation, which is in fact an expression of energy conservation, are too restrictive with respect to the flow in stenotic valves. Moreover, the surface integrals arised from the Navier-Stokes equations are neglected. In chapter 5, we will show that the values of these integrals are not negligible next to the values of dissipated energy and pressure drop.

The presented model is based on full time dependent Newtonian model using realistic three-dimensional geometry and physiologically relevant boundary conditions. It was shown that the model is capable to compute the relevant hemodynamic parameters such as pressure difference and amount of the dissipated energy, and it gives the values of transvalvular pressure difference consistent with the measured data.

With respect to limitations, there are two oversimplifications. The first oversimplification is principally geometric, and is the specification of valve structure and stenosis in the absence of actual valve leaflets, with stenosis modeled as a reduction in housing/wall diameter. The absence of valve leaflets necessitates up-front specification of the absence of regurgitation via a backstop. Thus, further work incorporating moving actual valve leaflets, and modeling stenosis as a reduction in leaflet motion and systolic (for the aortic valve) ejection orifice expansion and subsequent contraction is necessary. Nonetheless, the current model can yet be applied to arterial blood flow in its current form. The second limitation is that a rigid aorta is assumed. Many previous studies have incorporated aortic wall mechanics, but using simplified lumped parameter approaches. Further work would address this oversimplification as well.

A variety of mechanisms contribute to energy losses, see (Akins et al., 2008): so called "viscous losses", "turbulent losses", "flow separation losses", etc. However, these losses are not independent or additive. More importantly, Bernoullis equation is absolutely mute with regard to all three of these losses, or for that matter, any energy losses. The physical basis and blood property understanding for all of these types of energy losses is viscosity. However, the Bernoulli equation based approach assumes an inviscid fluid. Finally, with regards to turbulence, no current model is capable of describing the relevant phenomena. Consequently, it has remained one of the most important unsolved problems in mechanics. Thus, to merely appeal to an *ad hoc* modification of Bernoullis equation incorrectly suggests that a more rigorous approach is being employed than that which is actually used.

4. Computation of the pressure data directly from velocity data including the potential error in measurements

The ability to non-invasively determine the pressure in a flowing fluid has wide ranging technological relevance and import, an example being problems in medicine concerning the flow of biological fluids. The cardiovascular system presents several situations wherein the non-invasive determination of pressure would significantly reduce serious risks, including fatality, associated with invasive procedures. This study is concerned with the determination of the pressure field from non-invasive velocity data with a view towards determining the pressure drop across a diseased valve as a consequence of the dissipation in the fluid as it flows through the valve, the loss of pressure bearing a direct relation to the extent of the disease. While there have been some careful mathematical attempts at determining the pressure field from information for the velocity field, with regard to the Navier-Stokes fluid (see the references below), most of the studies concerning the determination of pressure from the velocity data with regard to flow across diseased valves and other related cardiovascular flow problems are based on an appeal to inappropriate governing equations, namely the Bernoulli equation, which are grossly inadequate to describe the dissipation that takes place in a flowing fluid, see section 3.1, namely (**Hatle equation**), as it is used in clinical practice, although it is derived from the simplified Bernoulli equation, i.e. under the law of conservation of energy.

What is however required is a much more careful consideration of the viscous dissipation that takes place during the fluid flow and the resulting pressure drop. We discuss in detail the inverse problem of determining the pressure field from data for the velocity field which might or might not be known precisely. The study does not appeal to the Bernoulli equation but considers in full the Navier-Stokes equations for an incompressible linearly viscous fluid.

While blood in small vessels exhibits shear-thinning characteristics, in a vessel of the size under consideration it can be modeled as a Newtonian fluid.

We idealize the geometry of the flow to a flow in a rigid pipe with an obstruction knowing full well that the real flow domain is far more complicated and the walls being highly deformable.

The methods for the pressure determination are introduced in section 4.1 and applied to the geometry representing the stenotic aortic valve with symmetric and non-symmetric obstruction in section 4.2. This approaches are also tested in patient-specific geometries representing cerebral vessels affected by an aneurysm. This is done in section 4.3. The results presented here were published in (Švihlová et al., 2016).

4.1 Determining the pressure for the flow of the Navier-Stokes fluid

Instead of trying to get some sort of an estimate on the loss of pressure as a consequence of the dissipation, we will introduce in this section how to directly obtain the pressure field once the velocity field is known. The velocity field is assumed to have been determined by either echocardiography or 4D Magnetic Resonance Imaging, and we will consider both knowledge of the velocity field at a limited amount of the points and the possibility of uncertainty of the values for the velocity field. This will be discussed in sec. 4.2.

Two methods of the pressure determination can be expressed in two different ways, one as a Poisson equation for the pressure field and the other based on the Stokes equation with additional stabilization/correction term. We will refer to them as Pressure Poisson Equation method (PPE method) and Stokes Equation method (STE method). They are described in sections 4.1.2 and 4.1.3.

We will use the velocity and pressure coming from the Navier-Stokes equations as a reference values and call them $\mathbf{v}_{ref}$ and p_{ref}, respectively. The velocity $\mathbf{v}_{ref}$ will be used as a starting point for two methods for pressure determination (instead of taking data from measurements). The reference pressure p_{ref} will be then used for the comparison of two methods which can directly compute the pressure field from the velocity field.

4.1.1 Reference flow

In a given domain $\Omega \subset \mathbf{R}^3$, representing the simplified aortic valve, the velocity $\mathbf{v}_{ref}$ and pressure p_{ref} satisfy

$$\rho_* \left(\frac{\partial \mathbf{v}_{ref}}{\partial t} + \left(\nabla \mathbf{v}_{ref} \right) \mathbf{v}_{ref} \right) + \nabla p_{ref} - \operatorname{div} \left(2\mu_* \mathbf{D}(\mathbf{v}_{ref}) \right) = \mathbf{0},$$
$$\operatorname{div} \mathbf{v}_{ref} = 0 \tag{4.1}$$

with the boundary conditions

$$\begin{aligned}
\mathbf{v}_{ref} &= \mathbf{0} && \text{on } \Gamma_{wall}, \\
\mathbf{v}_{ref} &= \mathbf{v}_{in} && \text{on } \Gamma_{in}, \\
\mathbf{T}\mathbf{n} - \frac{1}{2}\rho_*(\mathbf{v}_{ref} \cdot \mathbf{n})_- \mathbf{v}_{ref} &= -P(t)\mathbf{n} && \text{on } \Gamma_{out},
\end{aligned} \tag{4.2}$$

where $\mathbf{T} = -p_{ref}\mathbf{I} + 2\mu_* \mathbf{D}(\mathbf{v}_{ref})$. The vector $\mathbf{n}$ is the unit normal vector to the boundary $\partial\Omega$ which consists of three parts: Γ_{wall} denotes the walls and Γ_{in}, Γ_{out} are the inlet and outlet, respectively. The list of constants and their values is shown in Tab. 2.1. The subscript $*$ is always used for constants. The boundary data $\mathbf{v}_{in}$ and $\overline{P(t)}$ are the same as

used in section 3.3.2, namely the input velocity profile is parabolic with time-dependent magnitude given by the curve 3.8 (left) and the output pressure is prescribed as a time-dependent variable, but constant on the output plane for given time, given by the curve 3.8 (right). One cardiac cycle lasts 1s, the time when the aortic valve is considered open is from 0 s to 0.25 s (in opposite to 0.3 s used in the section 3.3.2). Initial condition for velocity is set to

$$\mathbf{v}_{ref}(t = 0) = \mathbf{0} \qquad\qquad \text{in } \overline{\Omega}. \qquad (4.3)$$

The computational meshes for the reference flow are shown in Fig. 4.1. The first one represents an aortic valve with 55% symmetric severity where the severity is given by formula (3.25) as a relation between the area of the healthy part and the area of the stenotic part. The length of the valve $L = 2.4$ cm and the radius of the healthy part $R = 1.2$ cm. For the stenotic part the length $l = 1.2$ cm and the radius $r = 0.805$ cm. The second mesh with the same L, l and R represents an aortic valve with 50% non-symmetric severity.
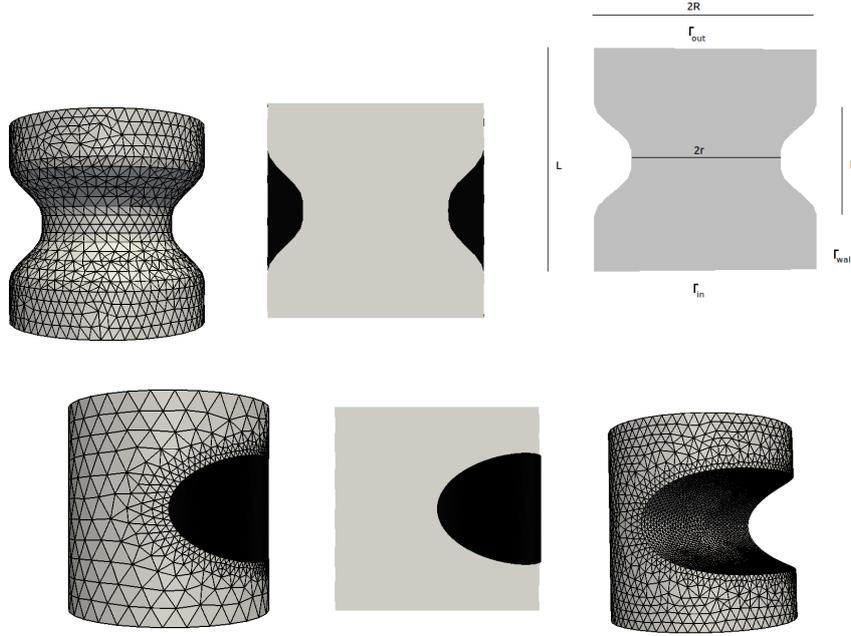
Figure 4.1: The first row: three-dimensional mesh for reference flow representing the valve with the symmetric stenosis with 55% severity, for illustration also the slices of the computational mesh. Grey parts represent the domain of valve, black parts represent the tissue causing the stenosis. The second row: three-dimensional mesh for reference flow representing the valve with the 50% non-symmetric stenosis, then a slice of a domain and another view to the mesh. The sizes of the meshes: $L = 2.4$ cm, $l = 1.2$ cm, $R = 1.2$ cm, $r_{sym} = 0.805$ cm.

4.1.2 Determination of the pressure by the PPE method

We now start with a discussion of the PPE method. We can derive from (4.1) for $q_{\mathrm{ppe}} \approx p$ that

$$-\nabla q_{\mathrm{ppe}} = \mathbf{f}(\mathbf{v}_{ref}), \tag{4.4}$$

where we define the quantity

$$\mathbf{f}(\mathbf{v}_{ref}) = \rho_* \left(\frac{\partial \mathbf{v}_{ref}}{\partial t} + \left(\nabla \mathbf{v}_{ref} \right) \mathbf{v}_{ref} \right) - \mathrm{div}(2\mu_* \mathbf{D}(\mathbf{v}_{ref})) \tag{4.5}$$

which depends only on the given velocity field $\mathbf{v}$.

On taking the divergence of the Navier-Stokes equations (4.1) we obtain, in virtue of the incompressibility condition $(4.1)_2$, that

$$-\Delta p = \rho_* \nabla \mathbf{v}_{ref} \cdot \left(\nabla \mathbf{v}_{ref} \right)^T. \tag{4.6}$$

Since the real problem takes place in a complex geometry, we will have to solve the Laplaces equation (4.6) numerically. For a given velocity field $\mathbf{v}_{ref}$, which may not be necessarily divergence free and consequently $\mathrm{div}\,\mathbf{f}(\mathbf{v}_{ref})$ differs from the right hand side of (4.6), we want to solve the problem for $q_{\mathrm{ppe}} \approx p$, where q_{ppe} meets

$$\begin{aligned}
-\Delta\, q_{\mathrm{ppe}} &= \mathrm{div}\,\mathbf{f}(\mathbf{v}_{ref}) && \text{in } \Omega, \\
\frac{\partial q_{\mathrm{ppe}}}{\partial \mathbf{n}} &= -\mathbf{f}(\mathbf{v}_{ref}) \cdot \mathbf{n} && \text{on } \partial\Omega
\end{aligned} \tag{4.7}$$

with $\mathbf{f}(\mathbf{v}_{ref})$ given by (4.5). We approximate $\frac{\partial \mathbf{v}}{\partial t}$ in (4.5) by $\frac{\mathbf{v}^{k+1}-\mathbf{v}^k}{t^{k+1}-t^k}$ where $\mathbf{v}^{k+1}$ is a given velocity field at current time step t^{k+1} and $\mathbf{v}^k$ is (also given) velocity field at previous time step t^k.

Since this problem admits unique solution up to a constant we need to supply some additional condition to have uniquely defined solution. We will provide a priori knowledge of the pressure mean value over the outlet of the domain.

We refer to the problem of finding a numerical solution of (4.7) with (4.5) and this additional condition fixing the value of pressure as the PPE method.

This method is described for example in (Heys et al., 2010; Gurka et al., 1999; Yang et al., 1996; Krittian et al., 2012; Bolin and Raguin, 2008; Charonko et al., 2010; Song et al., 1994; Dabiri et al., 2014; Shirokoff and Rosales, 2011) and is closely connected to a projection step in the projection methods used to decouple the velocity-pressure computation when solving the Navier-Stokes equations, see for example (Liu et al., 2010; Prohl, 2008; Guermond et al., 2006). In (Song et al., 1994) it is shown that the PPE method is equivalent to finding pressure p such that the functional $||\nabla p - \mathbf{f}(\mathbf{v}_{ref})||_{\Omega}^2$ is minimized.

In order to solve (4.7) for q_{ppe}, we need to know the appropriate boundary conditions for q_{ppe}. Boundary conditions are determined by the physics of the problem. However, when

one is unable to determine the appropriate boundary conditions based on an understanding of the physics of the problem, one can take recourse to a mathematical procedure that is reasonable and expected of the solution to the problem, provided one is assured of a solution that is sufficiently smooth. One can obtain conditions by evaluation the governing partial differential equation on the boundary.

This method leads to a scalar linear problem. However, even in the weak form it requires computation of first or even second derivatives of the velocity field, depending how many derivatives we can move to the test functions, which can be problematic if the velocity field is measured.

4.1.3   Determination of the pressure using the STE method

In this approach, based on the idea from (Cayco and Nicolaides, 1986), we want to directly determine a pressure as a function q_{ste} such that $-\nabla q_{\text{ste}} = \mathbf{f}(\mathbf{v}_{ref})$ in a weak sense, where $\mathbf{f}(\mathbf{v}_{ref})$ is given by (4.5).

This is done by solving a Stokes problem for the unknowns $\mathbf{w}$ and $q_{\text{ste}} \approx p$ such that

$$
\begin{aligned}
-\Delta\,\mathbf{w} - \nabla\,q_{\text{ste}} &= \mathbf{f}(\mathbf{v}_{ref}) && \text{in } \Omega, \\
\operatorname{div}\mathbf{w} &= 0 && \text{in } \Omega, \\
\mathbf{w} &= \mathbf{0} && \text{on } \partial\Omega.
\end{aligned}
\tag{4.8}
$$

It is important to recognize that $\mathbf{w}$ is considered here as an unknown and has nothing common with the given velocity $\mathbf{v}_{ref}$. In fact, $\mathbf{w}$ is expected to be almost zero. Again we need to provide a priori knowledge of the pressure at one point, or pressure mean value over some part of the domain or its boundary, to get a unique solution.

The solution of (4.8) with the right hand side of (4.5) and the prescribed mean pressure value over the outlet is referred to as the STE method. This method leads to a larger linear saddle-point type system of equations. However it requires less regularity on the data than the PPE method introduced in the previous section since no additional derivative of the data vector $\mathbf{f}(\mathbf{v}_{ref})$ is needed.

4.1.4   Weak formulation of the problems

The subsequent computations are run using the FEniCS, automated finite element solver (Logg et al., 2012) which allows for an easy employment of the standard finite element method to a wide class of variational problems. First, the Navier-Stokes problem (4.1) is written in variational form as (3.30).

The time discretization is done by an implicit one step difference method and with regard to spatial discretization, the function spaces V, P are approximated by standard piece-wise polynomial spaces, i.e. Taylor-Hood P_2/P_1 elements.

Standard FEM discretization is used to find the approximate solution to PPE and STE problems. The space P_S is approximated by piece-wise P_1 functions and the spaces P_P and

V by piece-wise P_2 functions. The space $\mathcal{R}$ is one dimensional space of constants on the computational domain and is used to enforce the additional condition on the mean value of the pressure over the Γ_{out} part of the boundary by means of global Lagrange multiplier.

Namely the PPE and STE problems are cast in weak forms as follows:

PPE: Find $(q_{\mathrm{ppe}}, r) \in P_P \times \mathcal{R}$ such that for all $(q^{test}, r^{test}) \in P_P \times \mathcal{R}$

$$\int_\Omega \nabla q_{\mathrm{ppe}} \cdot \nabla q^{test} \, dx = \int_\Omega \mathbf{f}(\mathbf{v}_{ref}) \cdot \nabla q^{test} + \int_{\Gamma_{out}} r \, q^{test} \, ds,$$

$$\int_{\Gamma_{out}} (q_{\mathrm{ppe}} - p) \, r^{test} \, ds = 0. \tag{PPE}$$

STE: Find $(\mathbf{w}, q_{\mathrm{ste}}, r) \in V \times P_S \times \mathcal{R}$ such that for all $(\mathbf{w}^{test}, q^{test}, r^{test}) \in V \times P_S \times \mathcal{R}$

$$\int_\Omega \nabla \mathbf{w} \cdot \nabla \mathbf{w}^{test} \, dx - \int_\Omega q_{\mathrm{ste}} \, \mathrm{div}\, \mathbf{w}^{test} \, dx = \int_\Omega \mathbf{f}(\mathbf{v}_{ref}) \cdot \mathbf{w}^{test} \, dx,$$

$$\int_{\Gamma_{out}} r \, q^{test} \, ds + \int_\Omega q^{test} \, \mathrm{div}\, \mathbf{w} \, dx = 0,$$

$$\int_{\Gamma_{out}} (q_{\mathrm{ste}} - p) \, r^{test} \, ds = 0. \tag{STE}$$

4.2 Numerical results

In sections 4.1.2 and 4.1.3 we introduced two approaches to ascertain the pressure directly from the velocity field. In order to compute the results achieved by these two methods we introduced the reference velocity $\mathbf{v}_{ref}$ and reference pressure p_{ref} in section 4.1.1. They are plotted, on slices of the meshes, in Fig. 4.2. The maximal local Reynolds numbers for these two problems, in symmetric and non-symmetric domains, are 560 and 765, respectively.

We will compare the pressures q_{ppe} and q_{ste} obtained by the two methods proposed in sec. 4.1.2 and 4.1.3 with this reference pressure p_{ref}. To do that, we will compute the pressure as an integral over the slices along the centerline as in eq. (4.9).

$$p_{\mathrm{REF}} = \frac{\int_\Gamma p_{ref} \, dS}{\mathrm{area}(\Gamma)} \tag{4.9}$$

The centerline is an axis passing through the vessel, Γ denotes the cross-section area perpendicular to the centerline, see Fig. 4.3. The resulting curves presenting the pressure drop within the domain, computed through the formula (4.9), are shown in the Fig. 4.4. The centerline here passes through the z axis so we will use the term "z coordinate" for the figures, not "cross-section area along the centerline".

We define q_{PPE} and q_{STE} for q_{ppe} and q_{ste} similarly as in eq. (4.9). While we will ascertain pressure only in a systolic time step $t = 0.125 \, \mathrm{s}$ as a steady flow, we will consider the

functions p_{REF}, q_{PPE} and q_{STE} depend only on the z coordinate.

In order to ascertain the efficiency of the two methods we compute the pressure field corresponding to three types of velocity data, the first which we refer to as fine data wherein we have full information for the velocity field on a very fine grid, the second type of data which we refer to as coarse data wherein the information is available only on a rough grids with different level of the coarseness, and finally the third type of data, "data with a noise", wherein the first two types are combined with added random modification in its values.

The reference velocity $\mathbf{v}_{ref}$ will serve as the input data for the pressure determination by PPE and STE methods, i.e. to find q_{ppe} and q_{ste}, respectively. The computed pressure p_{ref} will be used as the reference pressure to compare the accuracy of these two methods.

4.2.1 Fine data

We will start with the velocity field given on the same very fine mesh as that for which we know the velocity field exactly, i.e. velocity field known at every vertex of the mesh and with the velocity field measured exactly without noise. The meshes for symmetric and non-symmetric stenoses are shown in Fig. 4.7 and 4.8. Computation on the fine data corresponds to the computation on L0 mesh, i.e. the finest mesh.

For both cases, symmetric and non-symmetric, we compute the relative errors

$$
\begin{aligned}
err_{ppe} &= \frac{\|q_{\mathrm{ppe}} - p_{ref}\|_{L^2}}{\|p_{ref}\|_{L^2}}, \\
err_{ste} &= \frac{\|q_{\mathrm{ste}} - p_{ref}\|_{L^2}}{\|p_{ref}\|_{L^2}},
\end{aligned}
\tag{4.10}
$$

where obtained pressures q_{ppe} and q_{ste} were linearly interpolated to the finer mesh where p_{ref} was computed. The relative errors are shown in Tab. 4.1 and the point-wise errors are plotted in Fig. 4.5 for better illustration.
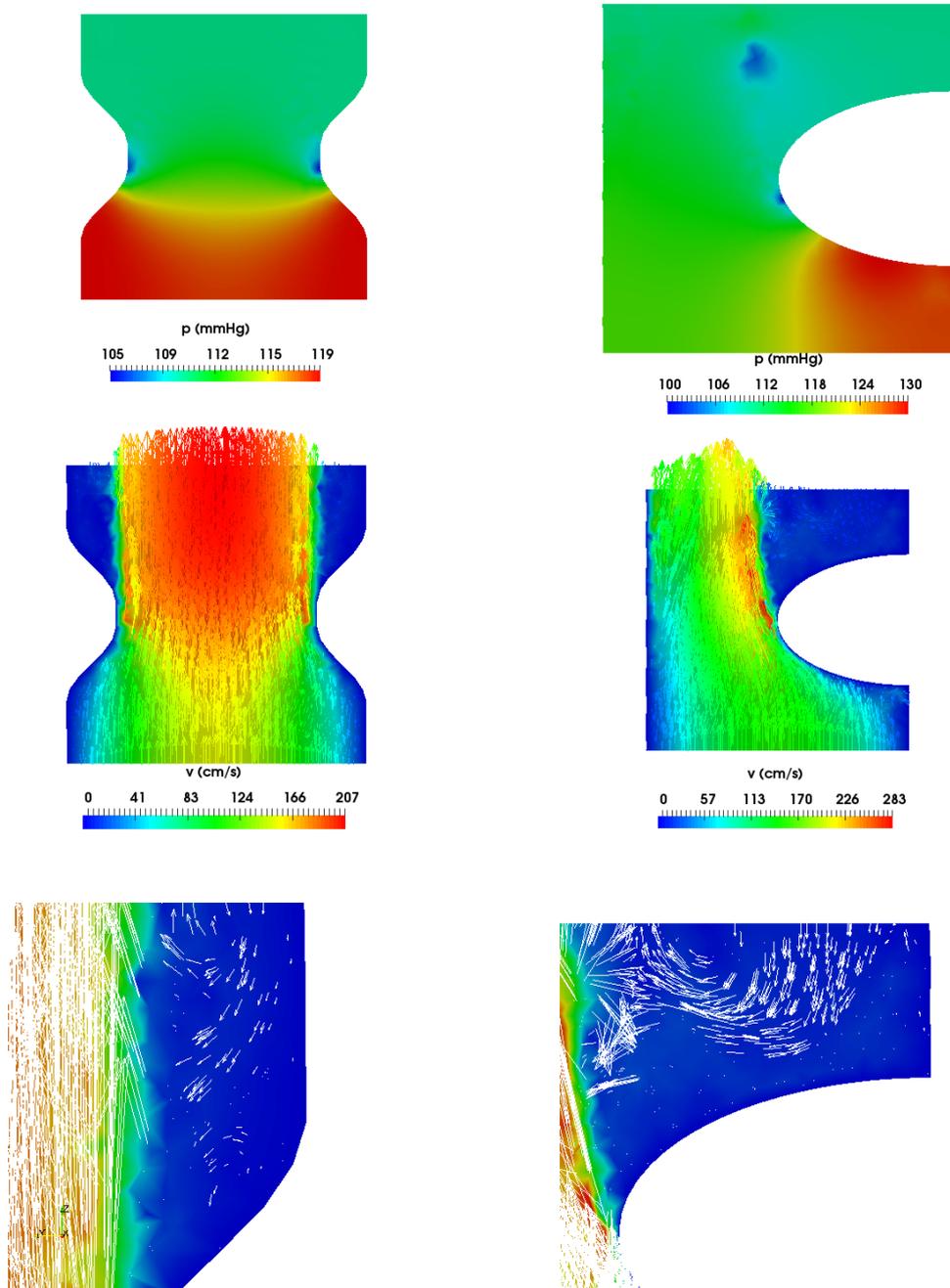
Figure 4.2: The first two rows depict the distribution of the reference pressure p_{ref} and the reference velocity $\mathbf{v}_{ref}$ for symmetric (left column) and non-symmetric (right column) domains; the third row contains the detail of the velocity field $\mathbf{v}_{ref}$ on slice near the outlet to show the recirculation in flow.
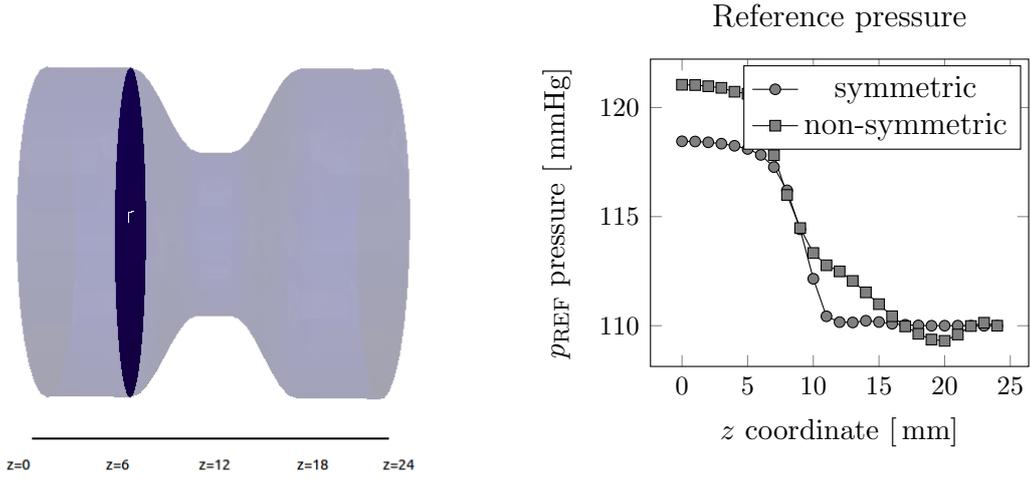
Figure 4.3: Cross-section areas Γ along the centerline.

Figure 4.4: The reference pressure p_{REF} (4.9) computed over cross-sections as a function of the position along the centerline for two different geometries during a systolic time step.

	$\dfrac{\|q_{\text{ppe}} - p_{ref}\|_{L^2}}{\|p_{ref}\|_{L^2}}$	$\dfrac{\|q_{\text{ste}} - p_{ref}\|_{L^2}}{\|p_{ref}\|_{L^2}}$
symmetric	6.40e-04	1.50e-14
non-symmetric	3.50e-03	1.16e-14

Table 4.1: Relative errors for fine data.

While we are fixing the pressures $p_{\text{REF}} = q_{\text{PPE}} = q_{\text{STE}}$ on Γ_{out}, computed through the formula (4.9), we are interested in comparison of the pressure differences or pressure drops $q_{\text{PPE}}^{\text{drop}}$ and $q_{\text{STE}}^{\text{drop}}$ compared to the reference pressure drop $p_{\text{REF}}^{\text{drop}}$. Their definitions are as follows:

$$\begin{aligned}
q_{\text{PPE}}^{\text{drop}} &:= q_{\text{PPE}}(inlet) - q_{\text{PPE}}(outlet), \\
q_{\text{STE}}^{\text{drop}} &:= q_{\text{STE}}(inlet) - q_{\text{STE}}(outlet), \\
p_{\text{REF}}^{\text{drop}} &:= p_{\text{REF}}(inlet) - p_{\text{REF}}(outlet).
\end{aligned} \tag{4.11}$$

The differences between the $q_{\text{PPE}}^{\text{drop}}$ and $q_{\text{STE}}^{\text{drop}}$ in comparison with $p_{\text{REF}}^{\text{drop}}$ are shown in Tab. 4.2, the pressures p_{REF}, q_{PPE} and q_{STE} are shown in Fig. 4.6.
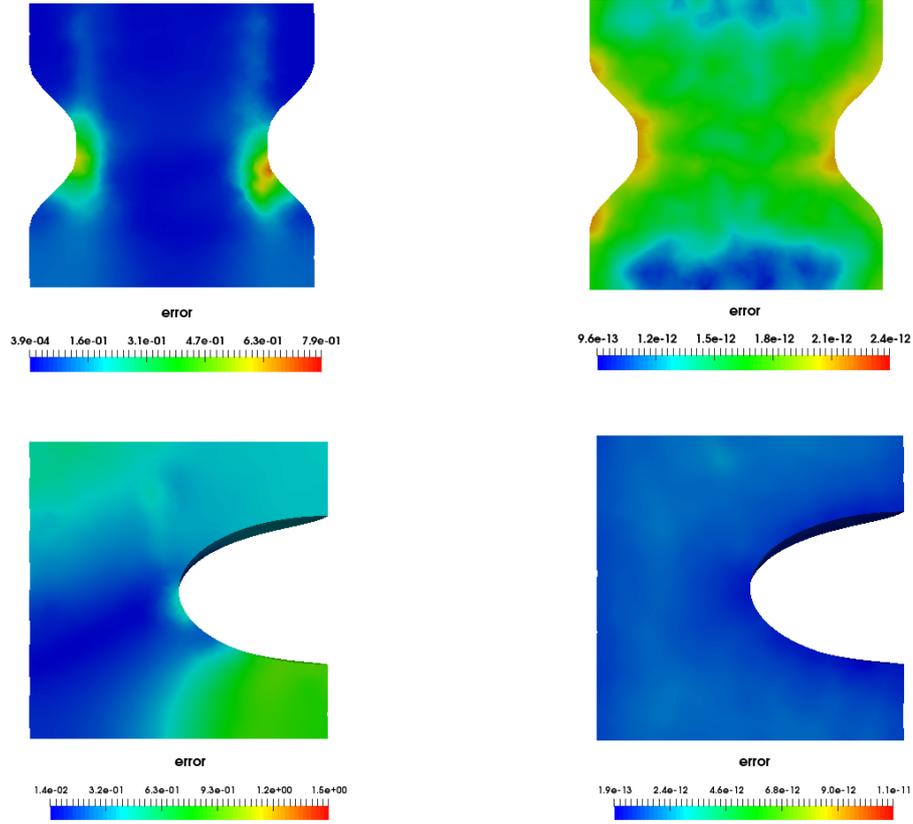
Figure 4.5: Absolute values of point-wise errors $\left|q_{\text{ppe}} - p_{ref}\right|$ (left column) and $\left|q_{\text{ste}} - p_{ref}\right|$ (right column) in mmHg on a slice of the symmetric domain (the first row) and non-symmetric domain (the second row).

	$\left|p_{\text{REF}}^{\text{drop}} - q_{\text{PPE}}^{\text{drop}}\right|$	$\left|p_{\text{REF}}^{\text{drop}} - q_{\text{STE}}^{\text{drop}}\right|$
symmetric	8.42e-02	1.42e-14
non-symmetric	9.44e-01	1.00e-08

Table 4.2: Errors in the pressure drops for fine data.
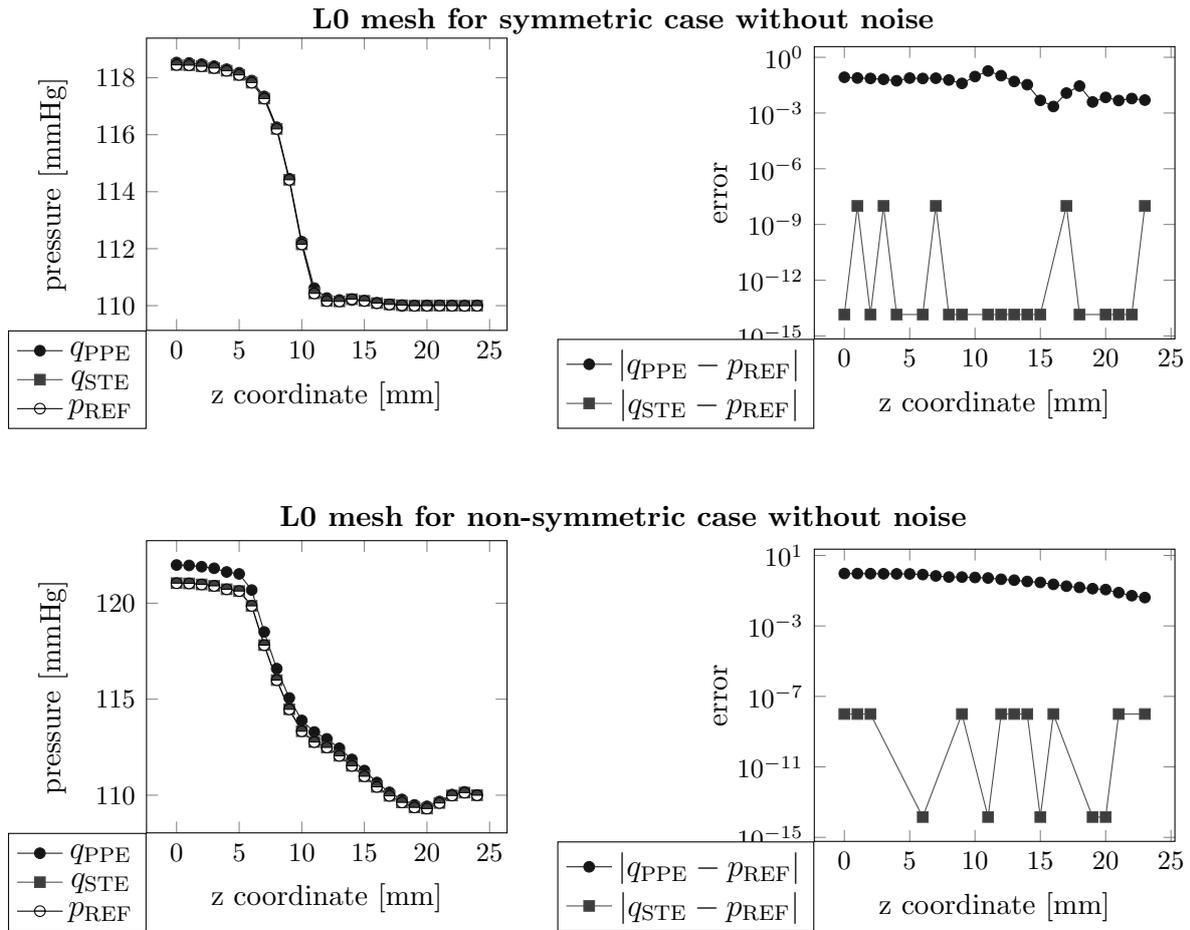
Figure 4.6: Results on L0 mesh without noise. First column: The reference and obtained pressure computed through the formula (4.9). Second column: The absolute value of difference between the reference and obtained pressure.

4.2.2 Coarse data

In this section we will do more tests with less accurate velocity fields with fewer points where we pretend to know the velocity exactly. This means computations on the coarser meshes. All of these meshes, referred here as a level L0 for the finest mesh and L4 for the coarsest mesh, are shown in Fig. 4.7 and 4.8.
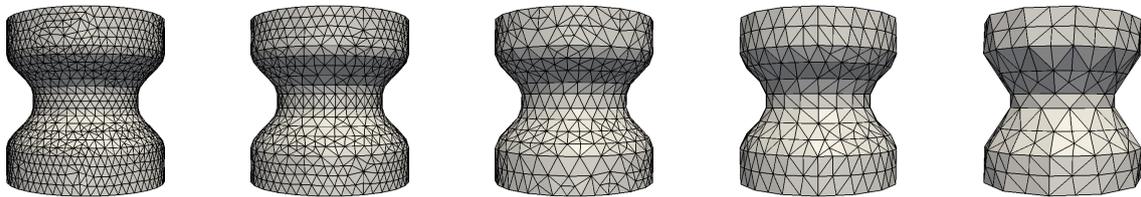
| L0 mesh: 19.861 nodes | L1 mesh: 9.883 nodes | L2 mesh: 4.856 nodes | L3 mesh: 2.405 nodes | L4 mesh: 1.138 nodes |

Figure 4.7: The computational mesh L0 for the reference flow and the coarser meshes for ascertaining pressure for symmetric case.
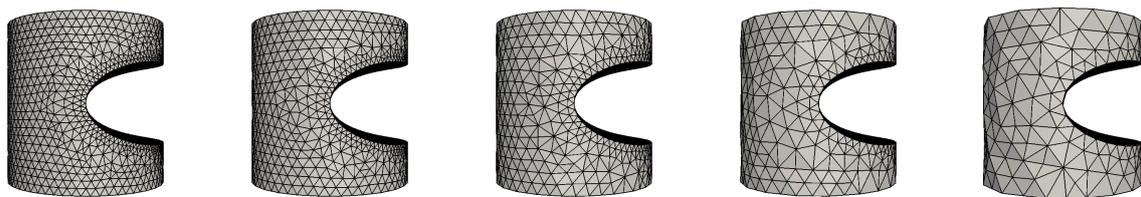
| L0 mesh: 22.427 nodes | L1 mesh: 11.883 nodes | L2 mesh: 6.255 nodes | L3 mesh: 3.085 nodes | L4 mesh: 1.479 nodes |

Figure 4.8: The computational mesh L0 for the reference flow and the coarser meshes for ascertaining pressure for non-symmetric case.

Pressures p_{REF}, q_{PPE} and q_{STE}, computed as in (4.9), and also the errors $|q_{\mathrm{PPE}} - p_{\mathrm{REF}}|$ are plotted for L0, L2 and L4 meshes in Fig. 4.9 for symmetric case and in Fig. 4.10 for non-symmetric case. The convergence curves of relative errors are shown in Fig. 4.11. $1/h$ here is taken as cube root of the number of nodes of the mesh. The relative errors, eq. (4.10), and the errors in pressure drop estimation are shown in the next section in Tab. 4.3 and Tab. 4.4, respectively.
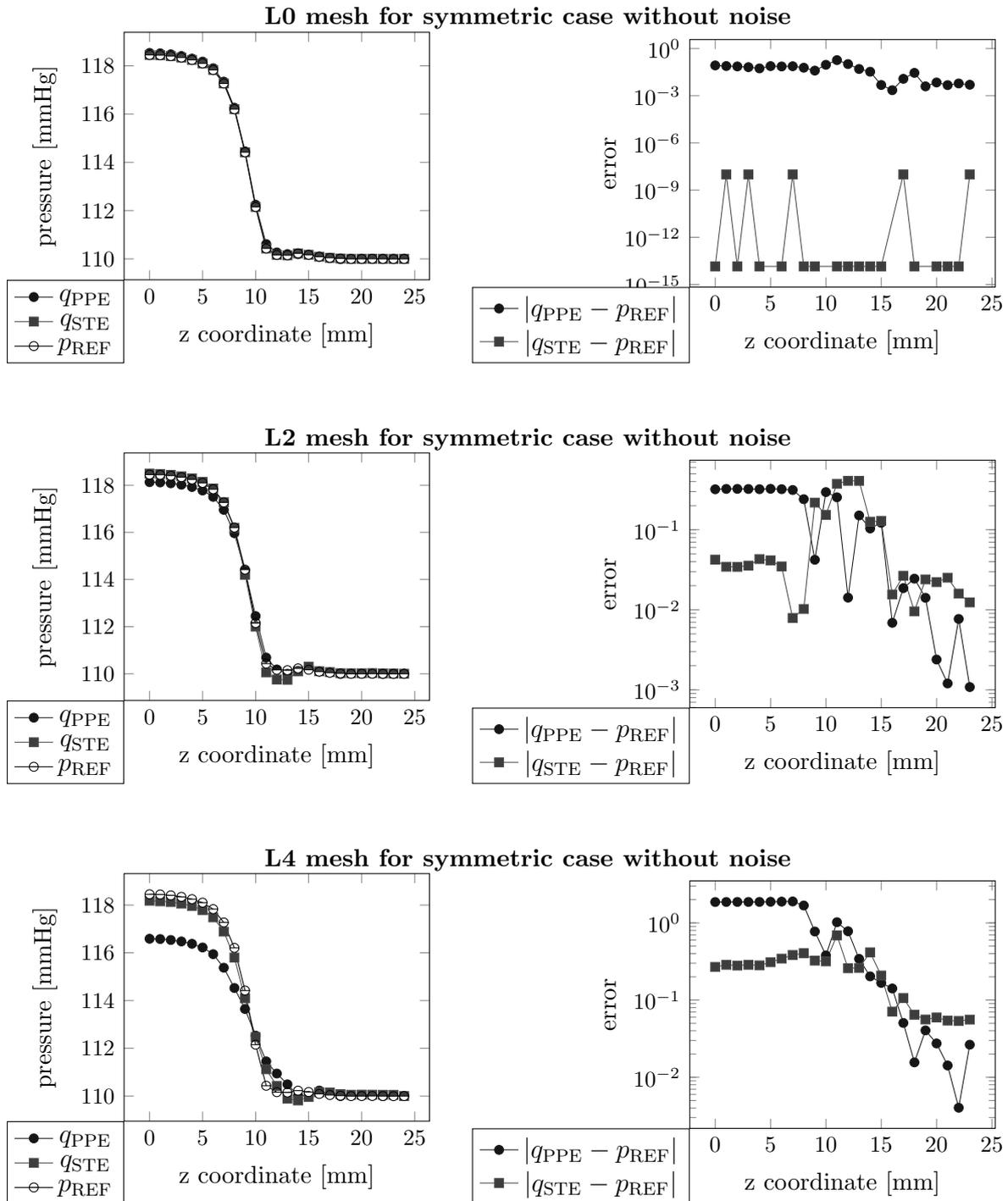
Figure 4.9: Reference and obtained pressure computed through the formula (4.9) in the first column and the absolute value of difference between the reference and obtained pressure in a second column for both methods.
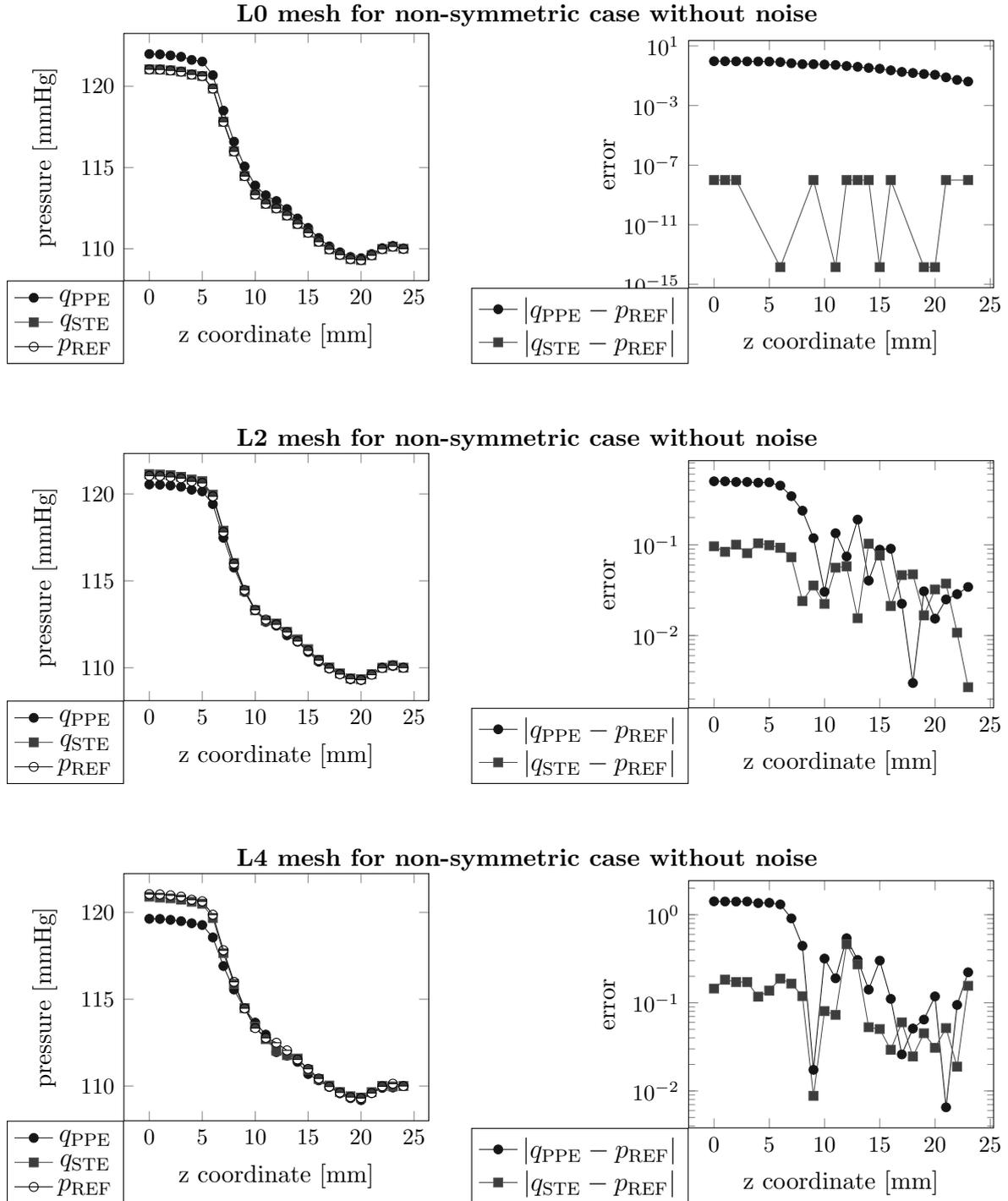
Figure 4.10: Reference and obtained pressure computed through the formula (4.9) in the first column and the absolute value of difference between the reference and obtained pressure in a second column for both methods.
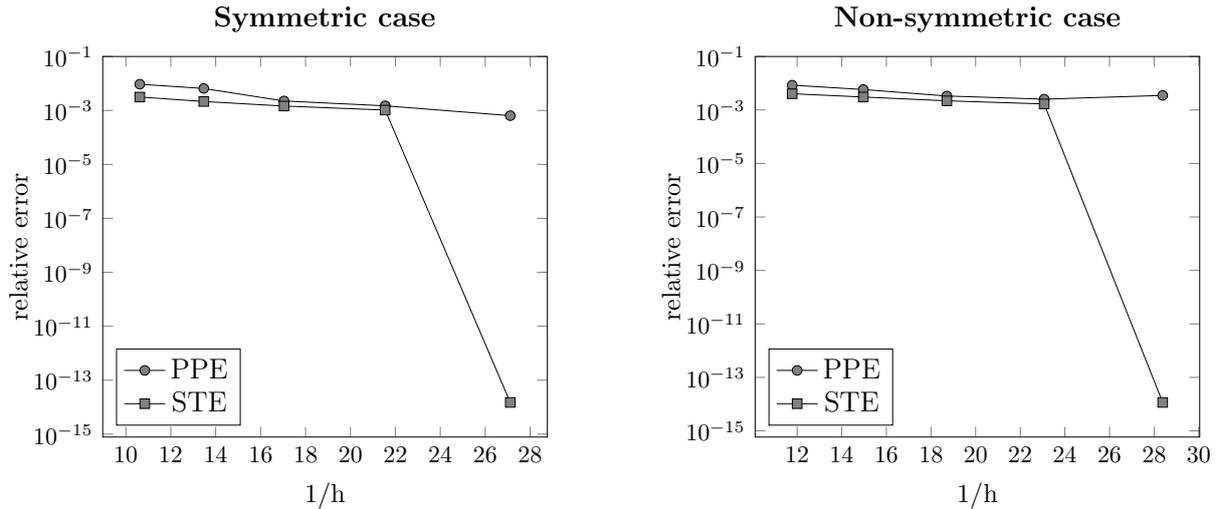
Figure 4.11: Convergence curves of relative errors for coarse data without noise.

4.2.3 Data with the noise

Here we want to simulate the fact that velocity is measured with the error or noise. While there is an interpolation error due to the limited amount of points where we know the velocity, we will also include the error of the measurement which can be as much as 5% or 10%. This means that the velocity $\mathbf{v}_{ref}(\overline{\mathbf{x}})$ in the point $\overline{\mathbf{x}}$ is replaced by the $\mathbf{v}_{\text{meas}}(\overline{\mathbf{x}}) = (1 \pm \varepsilon(\overline{\mathbf{x}}))\mathbf{v}_{ref}(\overline{\mathbf{x}})$ where $\varepsilon(\overline{\mathbf{x}}) \in [0, 0.05]$ for maximal 5% error, $\varepsilon(\overline{\mathbf{x}}) \in [0, 0.1]$ for maximal 10% error respectively. That is the vector of the reference (exact) velocity is (due to the measurement) lessened or increased in magnitude by the error 5% or 10%. This is numerically simulated by adding a random number $\varepsilon \in [-0.05, 0.05]$, $\varepsilon \in [-0.1, 0.1]$ respectively, to each point where we know the velocity.

We can combine these two errors (error due to information at a limited amount of points and error due to the deviations of measured and exact vectors). We will distinguish the meshes for computation as levels L0-L4, as they are labeled in Fig. 4.7 - 4.8, and the error due to the deviation as N0, N5 and N10 for including noise 0%, 5% or 10%.

The relative errors between the reference and obtained pressure are shown for both geometries (symmetric and non-symmetric) and for all computational meshes L0-L4 in Tab. 4.3. Tab. 4.4 shows the errors in pressure drop estimations.

The convergence curves of relative errors are shown in Fig. 4.12 and Fig. 4.13. 1/h here is taken as cube root of the number of nodes of the mesh.

	symmetric case			non-symmetric case		
	err_{ppe}	err_{ste}	$\frac{err_{ppe}}{err_{ste}}$	err_{ppe}	err_{ste}	$\frac{err_{ppe}}{err_{ste}}$
L0N0	6.40e-04	1.50e-14	-	3.50e-03	1.16e-14	-
L1N0	1.49e-03	1.03e-03	1.44	2.53e-03	1.68e-03	1.51
L2N0	2.24e-03	1.46e-03	1.54	3.33e-03	2.20e-03	1.51
L3N0	6.52e-03	2.15e-03	3.04	5.82e-03	3.05e-03	1.91
L4N0	9.37e-03	3.14e-03	2.99	8.46e-03	4.05e-03	2.09
L0N5	9.03e-04	6.66e-04	1.36	4.91e-03	2.81e-03	1.75
L1N5	1.82e-03	1.26e-03	1.45	4.94e-03	3.34e-03	1.48
L2N5	2.40e-03	1.52e-03	1.58	4.84e-03	3.83e-03	1.27
L3N5	7.10e-03	2.49e-03	2.85	8.07e-03	6.46e-03	1.25
L4N5	9.15e-03	3.18e-03	2.88	9.87e-03	8.46e-03	1.17
L0N10	1.45e-03	1.33e-03	1.09	6.89e-03	5.63e-03	1.22
L1N10	2.37e-03	1.75e-03	1.36	8.13e-03	6.09e-03	1.34
L2N10	2.86e-03	1.84e-03	1.56	7.76e-03	6.70e-03	1.16
L3N10	7.82e-03	3.13e-03	2.50	1.19e-02	1.20e-02	0.99
L4N10	9.06e-03	3.44e-03	2.63	1.56e-02	1.57e-02	0.99

Table 4.3: Relative errors for PPE and STE methods, see eq. (4.10).

	symmetric case			non-symmetric case		
	$|p_{\mathrm{REF}}^{\mathrm{drop}} - q_{\mathrm{PPE}}^{\mathrm{drop}}|$	$|p_{\mathrm{REF}}^{\mathrm{drop}} - q_{\mathrm{STE}}^{\mathrm{drop}}|$	$\frac{|p_{\mathrm{REF}}^{\mathrm{drop}} - q_{\mathrm{PPE}}^{\mathrm{drop}}|}{|p_{\mathrm{REF}}^{\mathrm{drop}} - q_{\mathrm{STE}}^{\mathrm{drop}}|}$	$|p_{\mathrm{REF}}^{\mathrm{drop}} - q_{\mathrm{PPE}}^{\mathrm{drop}}|$	$|p_{\mathrm{REF}}^{\mathrm{drop}} - q_{\mathrm{STE}}^{\mathrm{drop}}|$	$\frac{|p_{\mathrm{REF}}^{\mathrm{drop}} - q_{\mathrm{PPE}}^{\mathrm{drop}}|}{|p_{\mathrm{REF}}^{\mathrm{drop}} - q_{\mathrm{STE}}^{\mathrm{drop}}|}$
L0N0	0.08	0.00	-	0.94	0.00	-
L1N0	0.23	0.05	4.841	0.44	0.12	3.772
L2N0	0.32	0.04	7.576	0.50	0.10	5.206
L3N0	1.19	0.14	8.770	1.01	0.03	30.697
L4N0	1.86	0.27	6.938	1.42	0.15	9.779
L0N5	0.04	0.10	0.418	1.17	0.29	4.024
L1N5	0.33	0.06	5.281	1.00	0.18	5.595
L2N5	0.23	0.14	1.688	0.71	0.02	43.149
L3N5	1.35	0.28	4.896	1.64	1.19	1.381
L4N5	1.90	0.36	5.342	0.22	1.44	0.153
L0N10	0.00	0.20	0.017	1.39	0.58	2.387
L1N10	0.43	0.17	2.554	1.55	0.47	3.314
L2N10	0.14	0.24	0.601	0.92	0.06	15.805
L3N10	1.51	0.41	3.673	2.27	2.40	0.945
L4N10	1.92	0.44	4.402	1.86	3.03	0.616

Table 4.4: Error in the pressure drop for PPE and STE methods, see eq. (4.11).
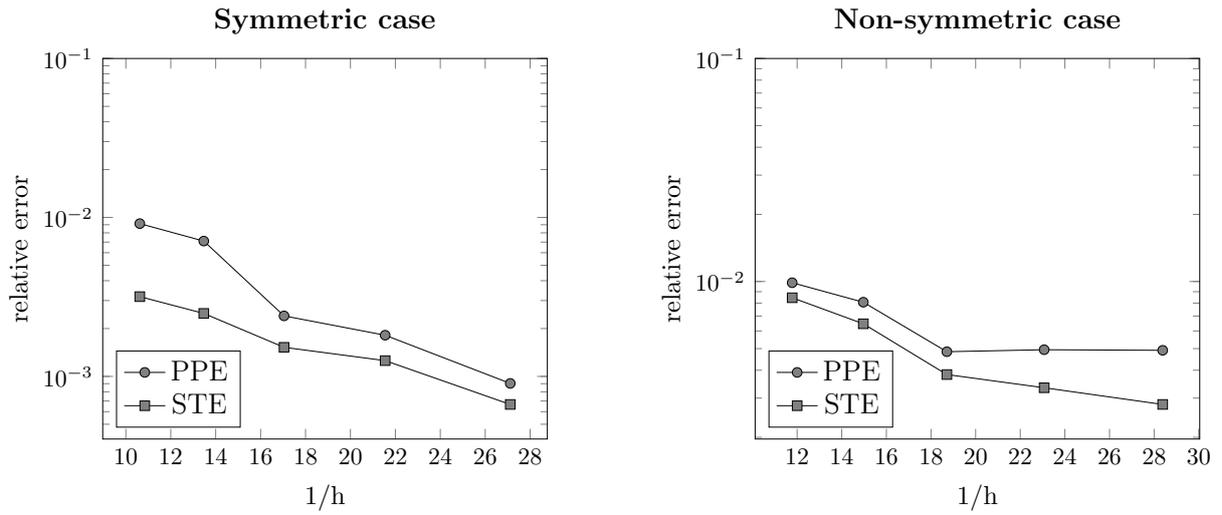
Figure 4.12: Convergence curves of relative errors for coarse data with 5% noise.
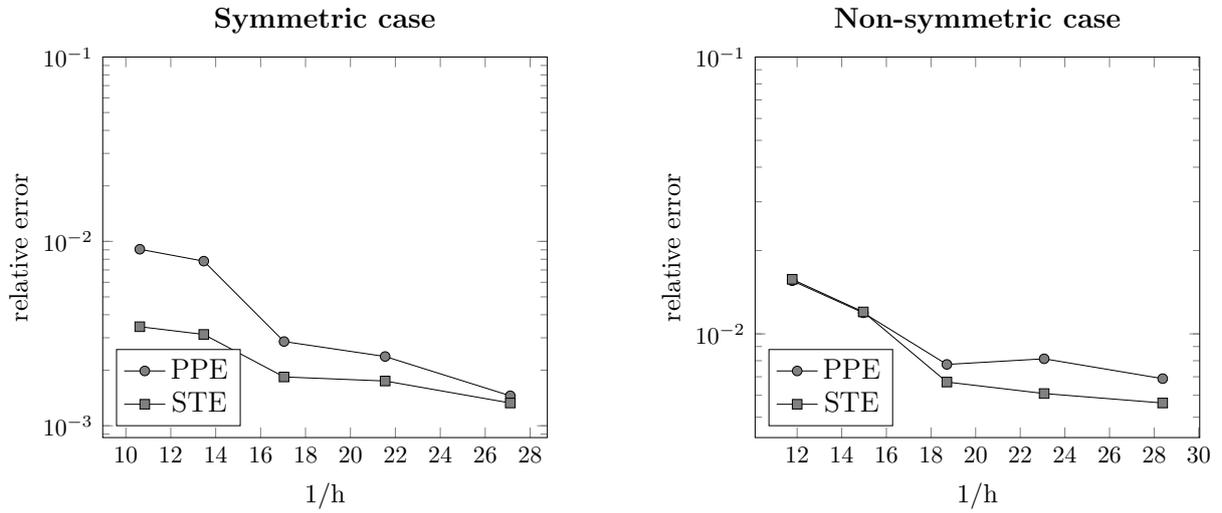
Figure 4.13: Convergence curves of relative errors for coarse data with 10% noise.

4.3 Computation of the pressure from the velocity field in patient specific geometry

In this section we will demonstrate the fact the methods can be used for patient specific geometry obtained from imaging methods. The geometry used here will be the geometry of the cerebral artery (namely basilar artery, see Fig. 1.3) affected by an aneurysm, shown in Fig. 4.14. The geometry was derived by the process described in section 2.1.
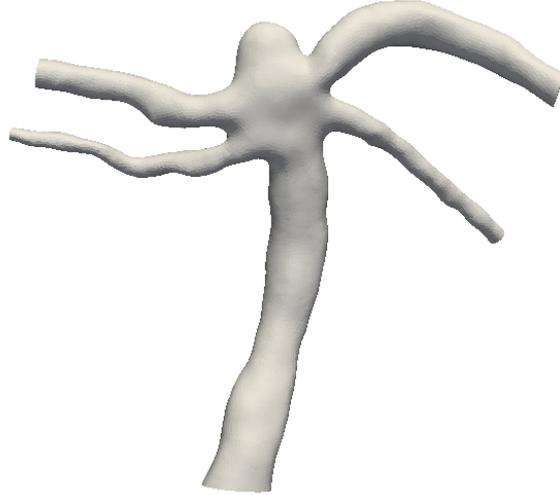
Figure 4.14: Geometry of the cerebral aneurysm.

Fig. 4.15 shows absolute values of point-wise errors $\left|q_{\mathrm{ppe}} - p_{ref}\right|$ and $\left|q_{\mathrm{ste}} - p_{ref}\right|$ in Pa for PPE method and STE method, respectively. The error distributions are shown on the whole domain, specially on the aneurysm sac, and on the slice. These point-wise plots show the error for "fine data" as they were introduced in section 4.2.1, i.e. the computation with the knowledge of the exact velocity field in all points of the geometry. There is a uniformly distributed error for STE method, the same results as was obtained in section 4.2 for simplified domains, see Fig. 4.2.

The methods were tested also in the "coarser data", as they were described in section 4.2.2, i.e. the computations were performed with the knowledge of the exact velocity field but only in the smaller amount of points of the geometry. This was simulated by using the coarser meshes. The number of nodes and the average node distances are shown in Tab. 4.5.

The relative errors

$$e_{ppe}^{rel} = \frac{\|q_{\mathrm{ppe}} - p_{ref}\|_{\mathrm{L}^2}}{\|p_{ref}\|_{\mathrm{L}^2}}, \quad e_{ste}^{rel} = \frac{\|q_{\mathrm{ste}} - p_{ref}\|_{\mathrm{L}^2}}{\|p_{ref}\|_{\mathrm{L}^2}} \tag{4.12}$$

are plotted in Fig. 4.16 against the $1/h$ which is taken as cube root of the number of nodes of the mesh. The errors were more than thirty times higher. However, H^1 errors were only about 1.5 times higher. The relative errors are shown in L^2 norm in Tab. 4.6 and in H^1 norm in Tab. 4.7.

	c0	c1	c2	c3
# points	38763	28591	24891	23690
node distance	0.295	0.328	0.338	0.337

Table 4.5: Number of points and average node distance in mm in the computational mesh. The c0 refers to the "fine data" - the computation was performed with the whole information of the velocity, i.e. in all points. The c1-c3 refer to the "coarser data" - the computations with the limited information of the velocity. i.e. known in less amount of points.
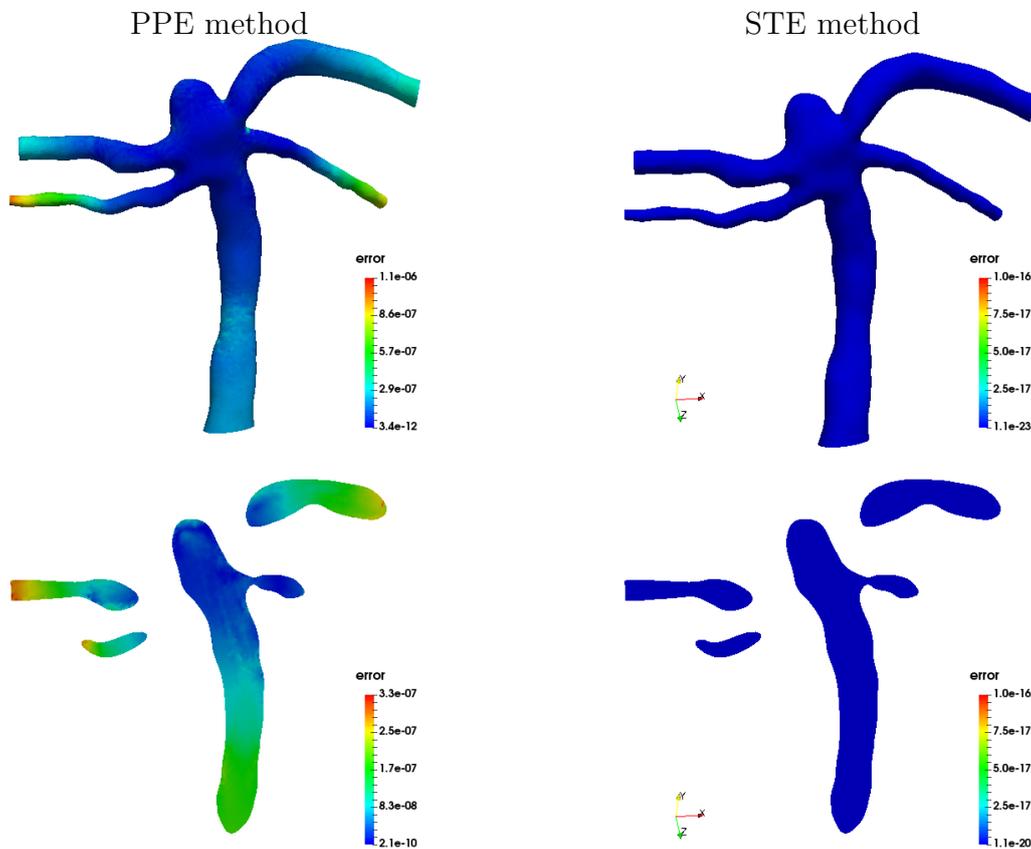
Figure 4.15: Absolute values of point-wise errors $\left|q_{\mathrm{ppe}} - p_{ref}\right|$ (left column) and $\left|q_{\mathrm{ste}} - p_{ref}\right|$ (right column) in mmHg on the surface of the mesh (the first row) and on a slice of the domain (the second row) for fine data in the case of patient-specific geometries.

93
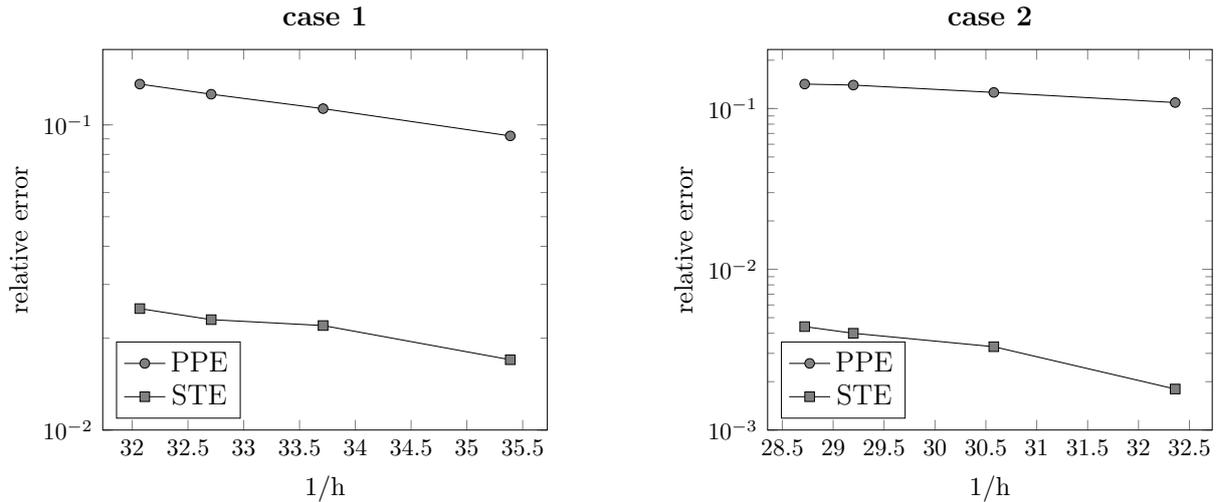
Figure 4.16: Convergence curves of relative errors for coarse data in patient-specific geometries.

	case 1 - PPE	case 1 - STE	case 2 - PPE	case 2 - STE
c0	0.092	0.017	0.109	0.0018
c1	0.113	0.022	0.126	0.0033
c2	0.126	0.023	0.140	0.0040
c3	0.136	0.025	0.142	0.0044

Table 4.6: Relative errors in L^2 norm for pressure determination in patient-specific geometries.

	case 1 - PPE	case 1 - STE	case 2 - PPE	case 2 - STE
c0	0.328	0.067	0.382	1.41e-13
c1	0.387	0.266	0.483	0.295
c2	0.397	0.292	0.510	0.341
c3	0.406	0.350	0.524	0.356

Table 4.7: Relative errors in H^1 norm for pressure determination in patient-specific geometries.

4.4 Conclusion

In this study, we have developed a mathematically rigorous methodology for the determination of the pressure field from a knowledge of the velocity field in the case of the Navier-Stokes fluid, with a view towards the determination of the pressure loss across a diseased valve. Two methods were tested firstly for idealized geometries in section 4.2,

then for patient-specific cerebral aneurysm geometries in section 4.3. In all of the cited references, the Pressure Poisson equation, referred here as PPE method, was used to compute the pressure. We compared the PPE method, as described in section 4.1.2, with a new approach, namely the STE method as presented in section 4.1.3. The STE method is based on the Helmholtz decomposition theorem (see for example (Maria Denaro, 2003) for its application in the context of projection methods), and it allows us to compute the pressure under lower regularity requirements on the given velocity. In Cayco and Nicolaides (1986) this approach is used to recover pressure for two-dimensional flows that allows the authors to use the stream function formulation. However we have not found any publication using this method to recover the pressure for given velocity field in general three dimensional flows. In sections 4.2 and 4.3 we show that the STE method provides more accurate pressure approximation than PPE method for the same velocity data. Of course, in the STE method we solve a system of four partial differential equations in three dimensions, while the PPE method requires solving just one scalar equation.

The study captures some of the salient features concerning the flow of blood in cardiovascular systems, such as the mechanical properties of blood and the spatiotemporal characteristics of ventricular, trans-valvular, and arterial blood flow. Also, we incorporated the normal physiological mechanical properties of the conduit. However, fully integrating the deformable conduit with moving fluid/solid boundary into the existing model, in order to develop a comprehensive mathematical model, is considerably more difficult and will be the focus of future endeavors. Testing a more refined model against clinically relevant datasets then may be undertaken.

5. Flow with slip boundary condition on the wall applied to the highly narrowed domain

In fluid dynamics, the influence of the material surrounding the domain enters the computation via boundary conditions. No-slip and slip boundary conditions can be considered as two limiting cases for boundary conditions prescribed on the walls whereas the Navier's slip and various stick-slip boundary conditions can capture some regimes between the limits.

Blood flow experiments (Bennett, 1967), (Bugliarello and Hayden, 1963) report the existence of slip of red cells in contact with the wall in small glass capillaries. It was suggested that the existence of slip can cause the flow dependence of the viscosity (Nubar, 1971). It was shown that changes of the Navier's slip parameter can change the flow more markedly than the change of the constitutive equation for the fluid (Hron et al., 2008).

From this perspective, it is of interest to see how the macroscopic properties, such that transvalvular pressure difference and energy dissipation across the stenotic valve, differ in the two limiting cases of the boundary condition on the walls, no-slip and free-slip.

In this chapter we will compute the fluid flow described by the non-stationary incompressible Navier-Stokes equations in bounded fixed domain $\Omega \subset \mathcal{R}^3$ with free-slip boundary condition prescribed on the walls. Computational model will be the same as used in chapter 3, except the free-slip prescribed on the walls and constant velocity profile prescribed on the inflow. Schema of the computational domain, representing the symmetric stenosis of aortic valve with 50% severity, is shown in Fig. 5.1.
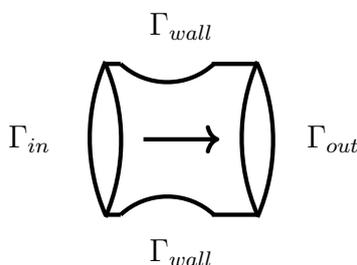
Figure 5.1: Schema of the computational domain.

The Dirichlet boundary condition for velocity will be prescribed on the inlet, the pressure and stabilization term, discussed in chapter 3, will be prescribed on the outlet. The free-slip boundary condition on the wall will be formulated and then treated by the Nitsche's method.

5.1 Problem formulation

Let the unknowns $(\mathbf{v}, p)$ satisfy the following system:

$$
\begin{aligned}
\frac{\partial \mathbf{v}}{\partial t} + (\nabla \mathbf{v})\,\mathbf{v} - \operatorname{div} \mathbf{T} &= \mathbf{0} & &\text{in } \Omega, \\
\mathbf{T} &= -p\mathbf{I} + \nu_* \left(\nabla \mathbf{v} + \nabla \mathbf{v}^T\right) & &\text{in } \Omega, \\
\operatorname{div} \mathbf{v} &= 0 & &\text{in } \Omega, \\
\mathbf{v} &= \mathbf{v}_{in} & &\text{on } \Gamma_{in}, \\
\mathbf{T}\mathbf{n} &= -p_{out}\mathbf{n} + \tfrac{1}{2}\left(\mathbf{v} \cdot \mathbf{n}\right)_-\mathbf{v} & &\text{on } \Gamma_{out}, \\
\mathbf{v} \cdot \mathbf{n} &= 0 & &\text{on } \Gamma_{wall}, \\
\left(\mathbf{T}\mathbf{n}\right)_\tau &= \mathbf{0} & &\text{on } \Gamma_{wall}
\end{aligned}
\tag{5.1}
$$

where $\Omega \subset \mathcal{R}^3$ is a fixed domain with the boundary $\partial\Omega$ consisting of three non-overlapping parts Γ_{in}, Γ_{out} and Γ_{wall}, $\mathbf{n}$ is the unit outward normal vector to the boundary and ν_* is a constant kinematic viscosity. The list of constants and their values are shown in chapter 2 in Tab. 2.1. There are two prescribed functions, $\mathbf{v}_{in} = \mathbf{v}_{in}(x, y, t)\colon \Gamma_{in} \times [0, \mathrm{T}] \to \mathcal{R}^3$ and $p_{out} = \frac{\overline{P(t)}}{\rho_*}\colon [0, \mathrm{T}] \to \mathcal{R}$ with $\mathrm{T} = 1.0\,\mathrm{s}$. Interval $[0, \mathrm{T}]$ represents a cardiac cycle. In this formulation, we identify p with $\frac{p}{\rho_*}$, where ρ_* is a constant density of the fluid. Initial condition for velocity is set to

$$
\mathbf{v}(t = 0) = \mathbf{0} \qquad\qquad \text{in } \overline{\Omega}. \tag{5.2}
$$

We would like to highlight three things. Firstly, inlet velocity profile suitable for slip boundary condition is constant flow, namely

$$
\mathbf{v}_{in} = -\overline{V(t)}\mathbf{n}, \tag{5.3}
$$

where $\overline{V(t)}\colon [0, \mathrm{T}] \to \mathcal{R}$ is a function depended only on time and $\mathbf{n}$ is the unit outward normal vector on Γ_{in}. Functions $\overline{V(t)}$ and $\overline{P(t)}$ are shown in chapter 3 in Fig. 3.8 with systolic ejection time (SEP) equal to $0.3\,\mathrm{s}$.

Secondly, slip boundary condition is prescribed only for the tangential part of the surface-traction vector $\mathbf{T}\mathbf{n}$ which was already defined as $\mathbf{wss} = \left(\mathbf{T}\mathbf{n}\right)_\tau$ in chapter 2 and computed as (2.23). Tangential part for a vector $\mathbf{z}$ is defined as

$$
(\mathbf{z})_\tau = \mathbf{z} - [\mathbf{z} \cdot \mathbf{n}]\,\mathbf{n}. \tag{5.4}
$$

Finally, the outflow boundary condition $(5.1)_4$ is the same as presented in section 3.4. It consists of the prescribed pressure and backflow stabilization term.

Weak formulation

In the considered case, the suitable functional spaces are

$$V := \left\{ \mathbf{v} \in \mathrm{L}^\infty \left(\mathrm{I}, \left[\mathrm{H}^1(\Omega) \right]^3 \right); \quad \mathbf{v} = 0 \text{ on } \Gamma_{in}, \quad \mathbf{v} \cdot \mathbf{n} = 0 \text{ on } \Gamma_{wall} \right\}, \qquad (5.5)$$

$$P := \left\{ p \in \mathrm{L}^2 \left(\mathrm{I}, \mathrm{L}^2(\Omega) \right) \right\} \qquad (5.6)$$

where $\mathrm{I} = [0, \mathrm{T}]$ is a finite time interval.

Multiplying the first equation in (5.1) by the test function $\mathbf{v}_{test} \in V$ and integrating over the domain Ω and over the finite time interval $[0, \mathrm{T}]$ we get

$$\int_0^T \left[\left(\frac{\partial \mathbf{v}}{\partial t}, \mathbf{v}_{test} \right)_\Omega + \left((\nabla \mathbf{v}) \mathbf{v}, \mathbf{v}_{test} \right)_\Omega - (\operatorname{div} \mathbf{T}, \mathbf{v}_{test})_\Omega \right] dt = 0. \qquad (5.7)$$

We will also multiply the third equation in (5.1) by the test function $p_{test} \in P$.
Using the per-partes method and imposing the boundary conditions $(5.1)_4$-$(5.1)_7$ we get the weak formulation of the problem. For simplicity we will identify $\mathbf{v}$ with its part having homogeneous Dirichlet boundary condition on Γ_{in}, namely $\mathbf{v} := \mathbf{v} - \mathbf{v}_{in} \in V$. Then the weak formulation of (5.1) can be formulated as follows.
Find $(\mathbf{v}, p)$ in $V \times P$ satisfying for all $(\mathbf{v}_{test}, p_{test}) \in V \times P$

$$\int_0^T \left[\left(\frac{\partial \mathbf{v}}{\partial t}, \mathbf{v}_{test} \right)_\Omega + \left((\nabla \mathbf{v}) \mathbf{v}, \mathbf{v}_{test} \right)_\Omega + (\mathbf{T}, \nabla \mathbf{v}_{test})_\Omega \right] dt +$$
$$- \int_0^T \left(\frac{1}{2} (\mathbf{v} \cdot \mathbf{n})_- \mathbf{v}, \mathbf{v}_{test} \right)_{\Gamma_{out}} dt = - \int_0^T (p_{out} \mathbf{n}, \mathbf{v}_{test})_{\Gamma_{out}} dt, \qquad (5.8)$$

$$- \int_0^T (\operatorname{div} \mathbf{v}, p_{test})_\Omega \, dt = 0. \qquad (5.9)$$

5.2   Nitsche's method

Nitsche's method was introduced by (Nitsche, 1971) to handle the Dirichlet boundary conditions and put them into the weak formulation. It is type of a penalty method. The Nitsche's method can be connected to the stabilized Lagrange multiplier method (Babuška, 1973; Barbosa and Hughes, 1991), as discussed in (Stenberg, 1995). The range of method's applications covers domain decomposition (Juntunen, 2015) or fluid structure interaction problems (Benk et al., 2012).

In this section we will show the Nitsche's method applied to the boundary conditions on the wall $(5.1)_6$ and $(5.1)_7$. Then the finite element discretization will be formulated. The equations used in this section was presented in (Freund and Stenberg, 1995) for Stokes

equations and in (Mekhlouf et al., 2016) for the Navier-Stokes equations with slip boundary condition on the whole boundary. Both papers also shown the numerical results on 2D geometry.

According to the weak formulation (5.8)-(5.9) we will define variational forms

$$B(\mathbf{v}, p, \mathbf{v}_{test}, p_{test}) = \big((\nabla \mathbf{v}) \, \mathbf{v}, \mathbf{v}_{test}\big)_\Omega + (\mathbf{T}, \nabla \mathbf{v}_{test})_\Omega +$$
$$- \left(\frac{1}{2}(\mathbf{v} \cdot \mathbf{n})_- \mathbf{v}, \mathbf{v}_{test}\right)_{\Gamma_{out}} - (\operatorname{div} \mathbf{v}, p_{test})_\Omega, \tag{5.10}$$

$$F(\mathbf{v}_{test}) = - (p_{out}\mathbf{n}, \mathbf{v}_{test})_{\Gamma_{out}}. \tag{5.11}$$

Then the Nitsche's formulation of the problem

$$B(\mathbf{v}, p, \mathbf{v}_{test}, p_{test}) = F(\mathbf{v}_{test}) \tag{5.12}$$

is then defined as finding $(\mathbf{v}, p)$ in $V \times P$ satisfying $\forall (\mathbf{v}_{test}, p_{test}) \in V \times P$

$$\left(\frac{\partial \mathbf{v}}{\partial t}, \mathbf{v}_{test}\right)_\Omega + B(\mathbf{v}, p, \mathbf{v}_{test}, p_{test}) + C(\mathbf{v}, p, \mathbf{v}_{test}, p_{test}) = F(\mathbf{v}_{test}) \tag{5.13}$$

with

$$C(\mathbf{v}, p, \mathbf{v}_{test}, p_{test}) = \sum_{E \in \Gamma_{wall}} \frac{\beta \nu_*}{h_E} (\mathbf{v} \cdot \mathbf{n}, \mathbf{v}_{test} \cdot \mathbf{n})_E +$$
$$- (\mathbf{T}\mathbf{n} \cdot \mathbf{n}, \mathbf{v}_{test} \cdot \mathbf{n})_{\Gamma_{wall}} - (\mathbf{v} \cdot \mathbf{n}, \mathbf{T}^{test}\mathbf{n} \cdot \mathbf{n})_{\Gamma_{wall}} \tag{5.14}$$

where $\beta \in \mathcal{R}$ is a stabilization parameter, in computation set to 10000, ν_* is a constant kinematic viscosity and h_E is the diameter of the triangle E on Γ_{wall}. In the computation, we set h_E as the maximal triangle diameter on Γ_{wall} to be the same for all triangles, $h_E = 0.0031 \,\mathrm{m}$. The value of the ratio $\frac{\beta \nu_*}{h_E}$ is equal to $\frac{10^4 \cdot 3.71 \cdot 10^{-6}}{3.1 \cdot 10^{-3}} \approx 12$. $\mathbf{T}^{test}$ is formulated similarly as a Cauchy stress tensor $(5.1)_2$ with test functions $\mathbf{v}_{test}, p_{test}$, namely

$$\mathbf{T}^{test} = -p_{test}\mathbf{I} + \nu_* \left(\nabla \mathbf{v}_{test} + (\nabla \mathbf{v}_{test})^T\right). \tag{5.15}$$

Finite element discretization

Let us for simplicity assume that the domain Ω is given as a union of tetrahedra forming regular tetrahedralization.

We will use Taylor-Hood elements represented by the function spaces

$$\mathbf{v}_h, \mathbf{v}_h^{test} \in V_h := \left\{\mathbf{v}_h \in [C(\Omega)]^3, \ \mathbf{v}_h \mid_K \in [\mathrm{P}_2(K)]^3 \ \forall K \in \Omega; \ \mathbf{v}_h \mid_E = 0 \ \forall E \in \Gamma_{in}\right\},$$
$$p_h, p_h^{test} \in P_h := \left\{p_h \in C(\Omega), \ p_h \mid_K \in \mathrm{P}_1(K) \ \forall K \in \Omega\right\}.$$

Then the eq. (5.13)-(5.14) can be discretized. We look for $(\mathbf{v}_h, p_h) \in V_h \times P_h$ such that or all $(\mathbf{v}_h^{test}, p_h^{test}) \in V_h \times P_h$ holds

$$\left(\frac{\partial \mathbf{v}}{\partial t}, \mathbf{v}_{test}\right)_\Omega + B(\mathbf{v}_h, p_h, \mathbf{v}_h^{test}, p_h^{test}) + C(\mathbf{v}_h, p_h, \mathbf{v}_h^{test}, p_h^{test}) = F(\mathbf{v}_h^{test}) \qquad (5.16)$$

and the forms B, C, F are defined in eq. (5.10), (5.11) and (5.14).

Time discretization

Time discretization of the problem (5.16) will be treated by the Crank-Nicholson scheme as defined in chapter 2. For Nitsche's formulation, form $L(t)$ from eq. (2.16) is

$$\begin{aligned}L(t) = B(\mathbf{v}_h(t), p_h(t), \mathbf{v}_h^{test}, p_h^{test}) + C(\mathbf{v}_h(t), p_h(t), \mathbf{v}_h^{test}, p_h^{test}) + \\ - F(\mathbf{v}_h(t), p_h(t), \mathbf{v}_h^{test}, p_h^{test})\end{aligned} \qquad (5.17)$$

with B, C, F defined in eq. (5.10), (5.11) and (5.14).

5.3 Numerical simulations

In sections 5.1-5.2 we introduced the model of the flow with free-slip boundary condition on the wall treated by the Nitsche's method. In this section, we will compare the results obtained by this model with the results using no-slip boundary condition on walls. This problem was studied in chapter 3, see the eq. (3.22) and (3.26).

Results in cylindrical geometry

Firstly, the problem was tested in the cylinder. The diameter of the cylinder was set to 24 mm and its height to 44 mm to has similar sizes as the geometries representing the aortic valve (see below). Due to the flow distribution, shown in Fig. 5.2, dissipated energy in the cylinder with slip boundary condition and constant velocity profile was zero opposite to the nonzero dissipated energy in the no-slip case, concretely

$$\frac{1}{|\text{SEP}|} \int_{\text{SEP}} \frac{\int_\Omega 2\mu_* \mathbf{D}{:}\mathbf{D}\, dx}{volume}\, dt = 92.2 \frac{\text{Pa}}{\text{s}}$$

in no-slip case.
Pressure drop or pressure difference averaged over SEP,

$$\frac{1}{|\text{SEP}|} \int_{\text{SEP}} \frac{\int_{\Gamma_{in}} p\, dS}{area_{\Gamma_{in}}} - \frac{\int_{\Gamma_{out}} p\, dS}{area_{\Gamma_{out}}}\, dt,$$

was 0.3 mmHg in no-slip case and 0.18 mmHg in slip case. Length of the systolic ejection period, $|\text{SEP}|$, is equal to 0.3 s.
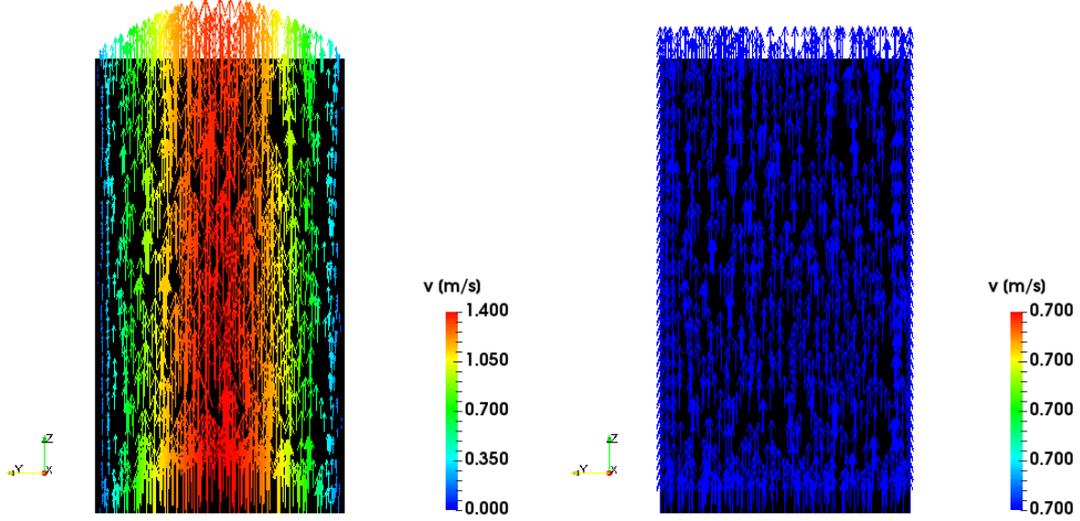
Figure 5.2: Velocity distribution on a slice of the cylindrical domain.

Results in valvular geometry

Both problems, called here as slip case and no slip case, represented by equations (5.1) and (3.22)&(3.26), was then computed on 6 different geometries. The geometries represent aortic valves, firstly without stenosis (or with 0% severity) and secondly with stenosis of 10%, 20%, 30%, 40% and 50% severity. Severity is given as a relation between the area of the stenotic and healthy part of the valve, see eq. (3.25). The meshes are shown in Fig. 5.3. Flow in these geometries, plotted as a velocity vectors on a slice of the domain, are shown in Fig. 5.4-5.9 at time of maximal velocity. Maximal velocity was set at time $t = 0.15\,\mathrm{s}$ to $0.65\frac{\mathrm{m}}{\mathrm{s}}$, see Fig. 3.8. Testing how the Nitsche's method satisfy the boundary condition $\mathbf{v} \cdot \mathbf{n} = 0$ on the walls, the integral $\int_{\Gamma_{wall}} (\mathbf{v} \cdot \mathbf{n})^2 \, dS$ was computed as an average over the SEP against the SEP-averaged integral $\int_{\Gamma_{wall}} \mathbf{v} \cdot \mathbf{v} \, dS$. This ratio was in order of 10^{-4} for all six valvular geometries and 10^{-6} for cylinder as it is shown in Tab. 5.1.

$\dfrac{\int_{\mathrm{SEP}} \int_{\Gamma_{wall}} (\mathbf{v}\cdot\mathbf{n})^2 \, dS\, dt}{\int_{\mathrm{SEP}} \int_{\Gamma_{wall}} \mathbf{v}\cdot\mathbf{v}\, dS\, dt}$	cylinder	0%	10%	20%	30%	40%	50%
SLIP	3.5e-06	2.1e-04	2.7e-04	3.2e-04	3.6e-04	4.1e-04	4.0e-04

Table 5.1: For slip case the satisfaction of the boundary condition $\mathbf{v} \cdot \mathbf{n} = 0$ was tested with respect to the flow magnitude on the walls.
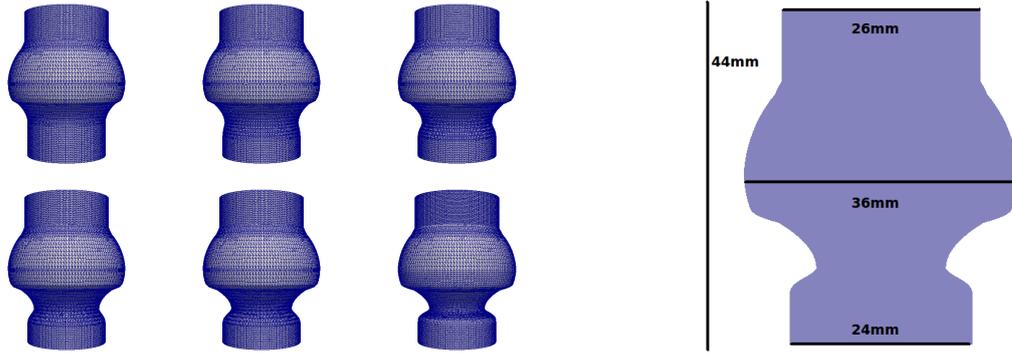
Figure 5.3: Computational meshes with 0%, 10%, 20%, 30%, 40% and 50% severity and their sizes.

NOSLIP 0% severity　　　　　　　　SLIP 0% severity
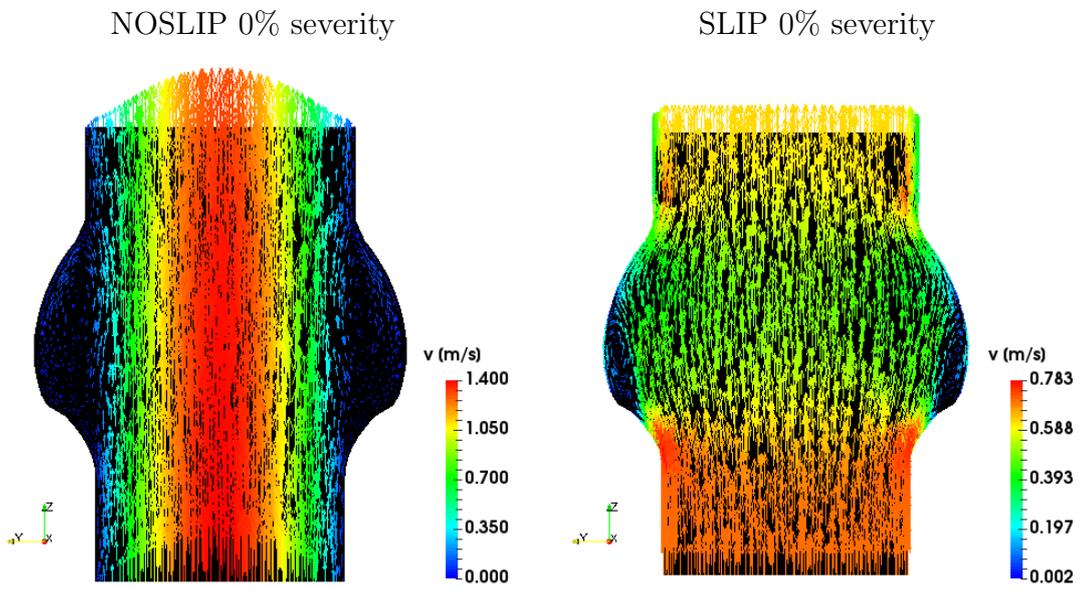
Figure 5.4: Velocity distribution on a slice of the valvular geometry without severity in time of maximal velocity ($t = 0.15\,\mathrm{s}$).

NOSLIP 10% severity — SLIP 10% severity
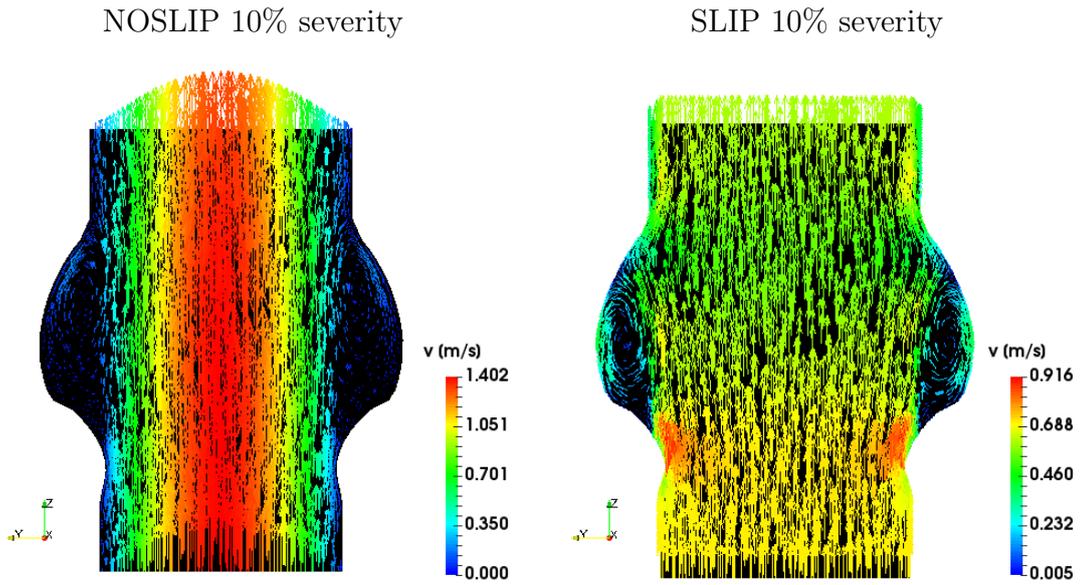
Figure 5.5: Velocity distribution on a slice of the valvular geometry with 10% severity in time of maximal velocity ($t = 0.15\,\mathrm{s}$).

NOSLIP 20% severity — SLIP 20% severity
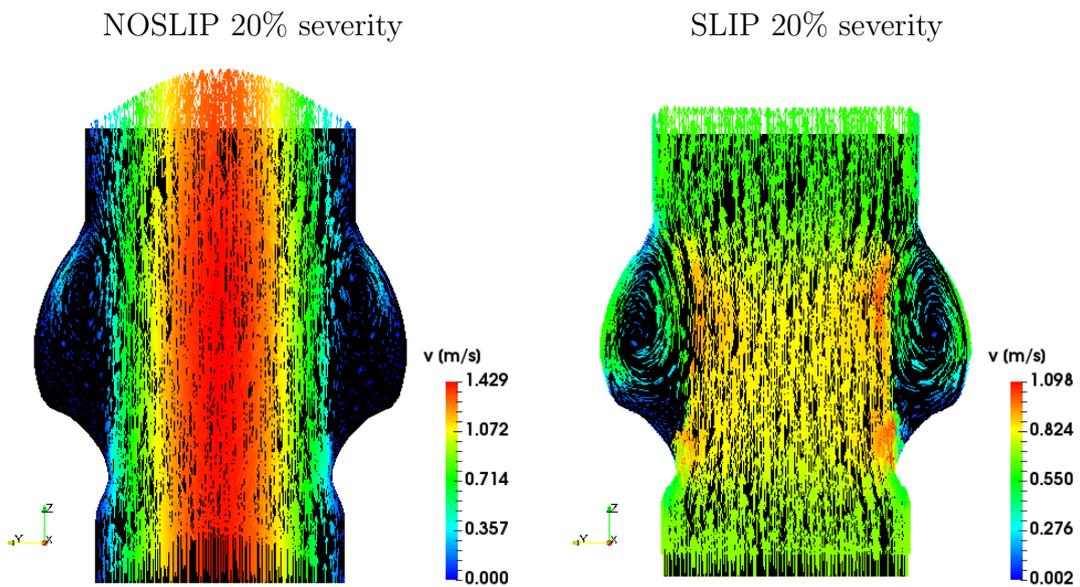
Figure 5.6: Velocity distribution on a slice of the valvular geometry with 20% severity in time of maximal velocity ($t = 0.15\,\mathrm{s}$).
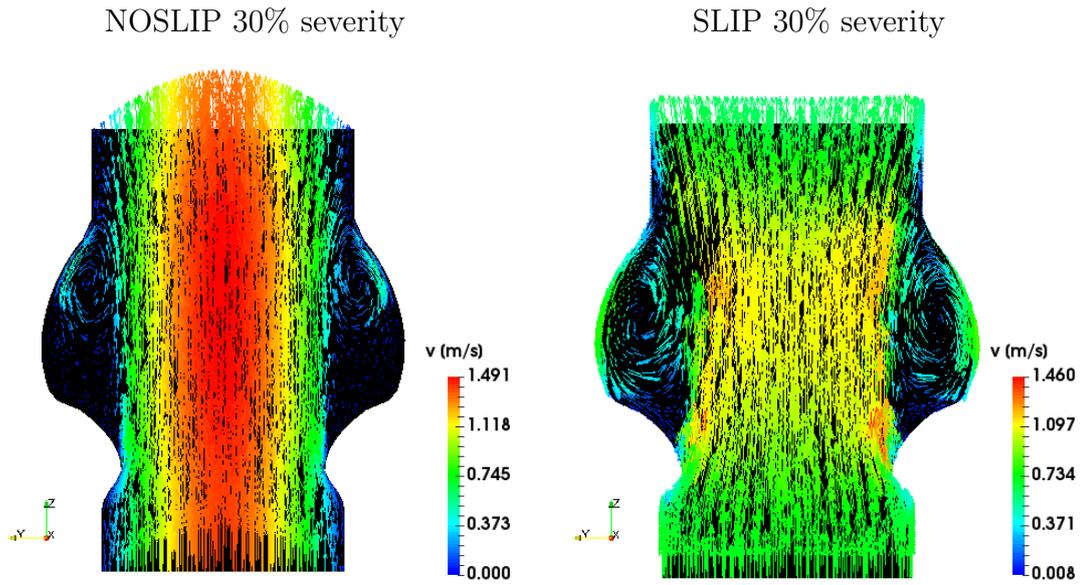
Figure 5.7: Velocity distribution on a slice of the valvular geometry with 30% severity in time of maximal velocity ($t = 0.15\,\mathrm{s}$).
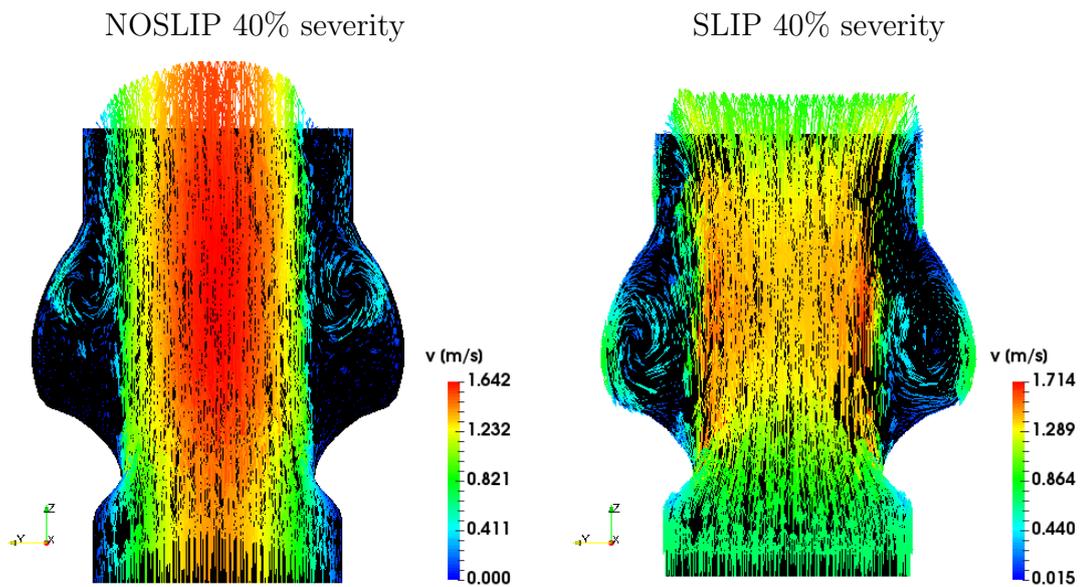
Figure 5.8: Velocity distribution on a slice of the valvular geometry with 40% severity in time of maximal velocity ($t = 0.15\,\mathrm{s}$).

NOSLIP 50% severity   SLIP 50% severity
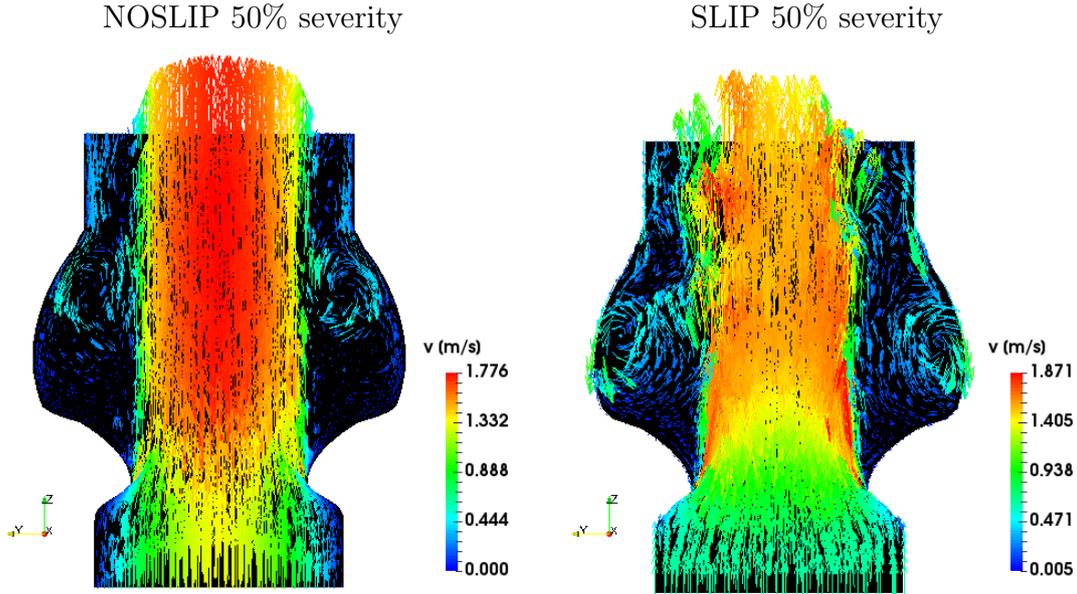
Figure 5.9: Velocity distribution on a slice of the valvular geometry with 50% severity in time of maximal velocity ($t = 0.15\,\mathrm{s}$).

As can be seen in Fig. 5.4-5.9, flow with slip boundary condition (and constant velocity profile) is highly different from that with no slip boundary condition (and parabolic inlet velocity profile). We would like to highlight that he computational geometry is short compared to the velocity magnitude (max $|\mathbf{v}_{in}| = 0.65\frac{\mathrm{m}}{\mathrm{s}}$, $length = 0.044\,\mathrm{m}$, see Fig. 5.3). The slip boundary condition leads to bigger vortices accompanied with higher velocity. On the other hand, noslip boundary condition leads to more straightforward flow and vortices are smaller with lower velocities. This results to the fact, that dissipation starts to be higher in slip case for stenotic cases. We summarize the dissipation, kinetic energy and pressure drop in Tab. 5.2 and plot them in Fig. 5.10. All variables are computed in Pascal to be easily compared, so the kinetic energy and pressure drop are computed as time averaged over the SEP and the rate of dissipation, $2\mu_*\mathbf{D}{:}\mathbf{D}$, is computed as an integral over the SEP. The conversion for pressure drop in mmHg is $1\,\mathrm{Pa} \approx -0.0075\,\mathrm{mmHg}$.

$\int_{\text{SEP}} \frac{\int_{\Omega} 2\mu_* |\mathbf{D}(\mathbf{v})|^2 \, dx}{volume} \, dt \; [\text{Pa}]$	0%	10%	20%	30%	40%	50%
NOSLIP	20.11	22.05	27.79	41.94	81.75	130.84
SLIP	11.67	24.21	63.38	138.84	194.75	257.95
$\frac{1}{|\text{SEP}|} \int_{\text{SEP}} \frac{\int_{\Omega} 0.5\rho_* |\mathbf{v}|^2 \, dx}{volume} \, dt \; [\text{Pa}]$	0%	10%	20%	30%	40%	50%
NOSLIP	118.97	122.35	129.36	142.53	166.38	176.47
SLIP	75.17	86.41	108.57	139.28	178.20	191.32
$\frac{1}{|\text{SEP}|} \int_{\text{SEP}} \frac{\int_{\Gamma_{in}} p \, dS}{\int_{\Gamma_{in}} dS} - \frac{\int_{\Gamma_{in}} p \, dS}{\int_{\Gamma_{in}} dS} \, dt \; [\text{Pa}]$	0%	10%	20%	30%	40%	50%
NOSLIP	8.61	17.16	33.01	84.18	204.29	384.07
SLIP	-4.61	17.72	46.72	119.87	320.44	527.75

Table 5.2: Dissipation, integrated over the SEP, and SEP-averaged kinetic energy and pressure drop in Pascal for prescribed slip and noslip boundary condition for 6 geometries with different level of severity.

energy dissipation [Pa]

kinetic energy [Pa]
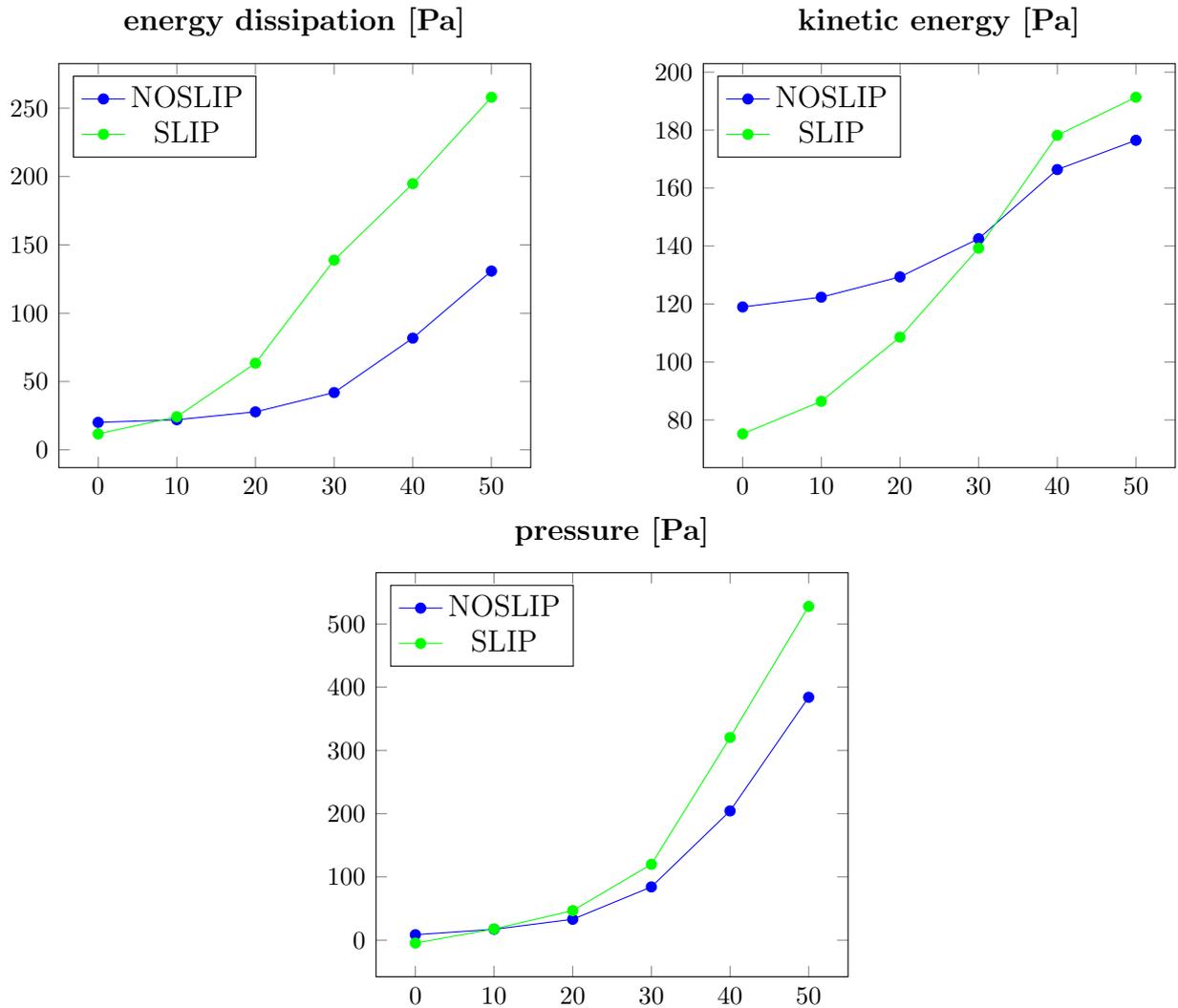
pressure [Pa]

Figure 5.10: Plotted data according to the Tab. 5.2. The x-axis reffers to the severity (0% severity means no stenosis), y-axis is always in Pascal.

Fig. 5.11 and 5.12 show the velocity magnitude, pressure, kinetic energy and energy dissipation in geometry of the valve with 50% stenosis averaged over the cross-sectional planes Γ, firstly at the time of maximum velocity ($t = 0.15\,\text{s}$), then averaged over the SEP (time interval between 0 and 0.3 s). Cross-sectional planes are planes perpendicular to the centerline with different z coordinate as can be seen in Fig. 3.11. The biggest difference between the two models can be seen in pressure drop and energy dissipation when the peak of energy dissipation in slip case is twice higher than in the noslip case.
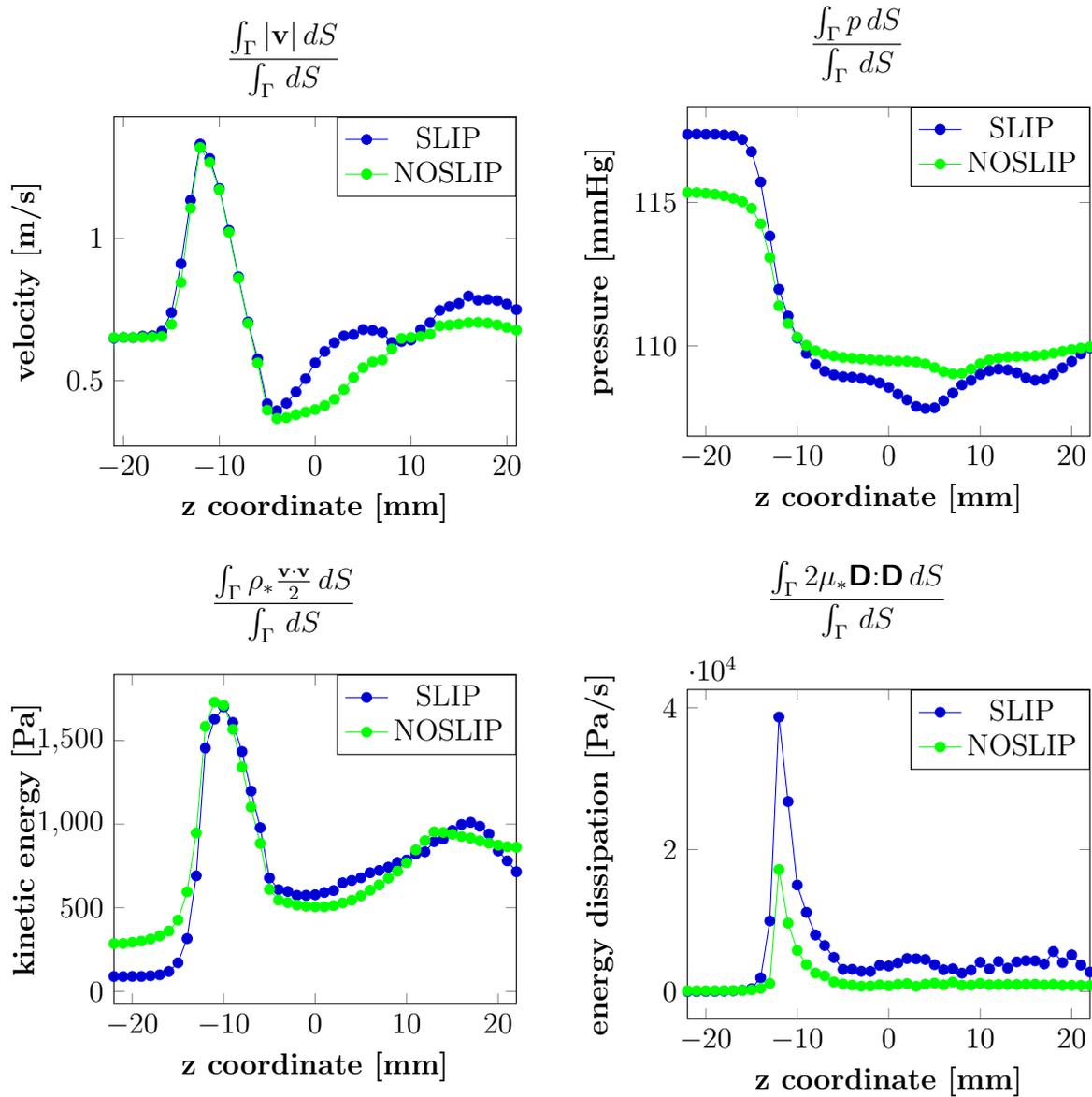
Figure 5.11: Velocity, pressure, kinetic energy and energy dissipation averaged over cross-sectional plane Γ for geometry representing 50% stenosis for prescribed slip and noslip boundary condition, varying as functions of the z coordinate (length), set at the time of maximum velocity ($t = 0.15\,\text{s}$).
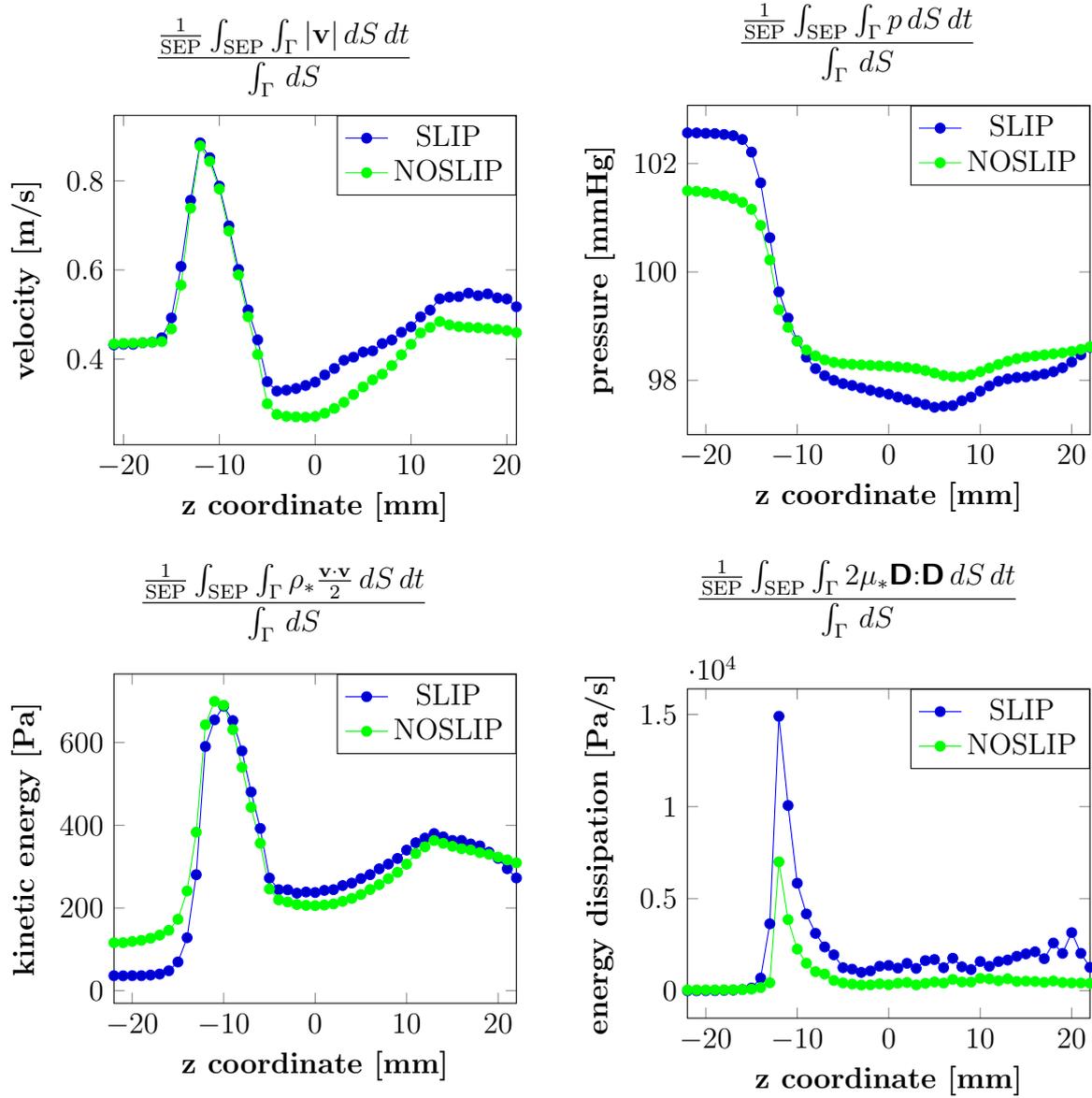
Figure 5.12: Velocity, pressure, kinetic energy and energy dissipation averaged over space (cross-sectional plane Γ and time (SEP) for geometry representing 50% stenosis for pre-scribed slip and noslip boundary condition, varying as functions of the z coordinate (length).

Integrals on boundary

Is section 3.2 we presented the set of assumptions leading to the Bernoulli relation (3.15) in case of similar $|\Gamma_{in}| \sim |\Gamma_{out}|$, namely

$$p^{in} - p^{out} = -\frac{1}{\omega^{in}|\Gamma_{in}|}\left(\frac{d}{dt}Ek(t) + Edis(t)\right). \tag{5.18}$$

These assumptions were following:

$$\mathbf{n}_{in} = (0,\ 0,\ -1),$$
$$\mathbf{n}_{out} = (0,\ 0,\ 1),$$
<div align="right">(A0)</div>

$$p(x, y, t) = p^{in}(t) \text{ on } \Gamma_{in},$$
$$p(x, y, t) = p^{out}(t) \text{ on } \Gamma_{out},$$
<div align="right">(A1)</div>

$$\mathbf{v} = (0,\ 0,\ \omega),$$
<div align="right">(A2)</div>

$$\omega(x, y, t) = \omega^{in}(t) \qquad \& \qquad \frac{\partial \omega}{\partial z} = 0 \qquad \text{on } \Gamma_{in},$$
$$\omega(x, y, t) = \omega^{out}(t) \qquad \& \qquad \frac{\partial \omega}{\partial z} = 0 \qquad \text{on } \Gamma_{out}.$$
<div align="right">(A3)</div>

Due to the recirculation, the assumptions (**A2**) and (**A3**) are not satisfied on the Γ_{out}. Incorporating only the first two assumptions, we ended with the relation (3.12), namely

$$-(p^{in} - p^{out}) \int_{\Gamma_{in}} \mathbf{v} \cdot \mathbf{n} \, dS + \frac{d}{dt} Ek(t) + Edis(t) =$$
$$= -\int_{\partial\Omega} \rho_* \frac{|\mathbf{v}|^2}{2} (\mathbf{v} \cdot \mathbf{n}) \, dS - \int_{\partial\Omega} 2\mu_* \mathbf{D}\mathbf{v} \cdot \mathbf{n} \, dS.$$
<div align="right">(5.19)</div>

There is a question how big are the integrals on the right hand side (RHS) in comparison with the values on the left hand side (LHS) appearing in Bernoulli equation (5.18). The integrals of RHS in all 6 valvular meshes are computed in Tab. 5.3.
Bernoulli equation would be satisfied if the values of the RHS would be zero. But in fact, the first term of the RHS is comparable with the values of the LHS. For example, for 50% stenosis in NOSLIP case,

$$-\int_{\text{SEP}} \int_{\partial\Omega} \rho_* \frac{|\mathbf{v}|^2}{2} (\mathbf{v} \cdot \mathbf{n}) \, dS \, dt \approx -|\text{SEP}| \cdot 0.065 = -0.0195$$

and

$$\int_{\text{SEP}} Edis(t) \, dt = \int_{\text{SEP}} \int_{\Omega} 2\mu_* |\mathbf{D}(\mathbf{v})|^2 \, dx \, dt \approx volume \cdot 130.84 = 0.0035$$

using the definition of $Edis(t)$, namely eq. (3.8), Tab. 5.2 and 5.3 and the fact that $|\text{SEP}| = 0.3\,\text{s}$ and $volume = 2.7 \cdot 10^{-5}\,\text{m}^3$.

$\frac{\int_{\text{SEP}} \int_{\partial\Omega} 2\mu_* \mathbf{D}\mathbf{v}\cdot\mathbf{n}\, dS\, dt}{\text{SEP}}$	cyl	0%	10%	20%	30%	40%	50%
NOSLIP	-3.8e-6	-5.6e-6	-6.6e-6	-9.9e-6	-1.7e-5	-2.2e-5	-2.6e-5
SLIP	-5.8e-15	-4.1e-4	-6.2e-4	-6.4e-4	-5.1e-4	-4.9e-4	-5.1e-4
$\frac{\int_{\text{SEP}} \int_{\partial\Omega} \frac{\rho_*}{2}|\mathbf{v}|^2(\mathbf{v}\cdot\mathbf{n})\, dS\, dt}{\text{SEP}}$	cyl	0%	10%	20%	30%	40%	50%
NOSLIP	-7e-3	-1.3e-2	-1.2e-2	-9.0e-3	1.2e-3	2.9e-2	6.5e-2
SLIP	-1.2e-14	-9.0e-3	-9.5e-3	-7.5e-3	4.7e-3	5.0e-2	8.5e-2

Table 5.3: SEP-averaged values of the surface integrals.

5.4 Conclusion

We presented the model describing the flow of Newtonian fluid in three-dimensional domain with free-slip boundary condition prescribed on the walls and treated by Nitsche's method. The problem was more challenging due to the geometry of the domain and high pressure prescribed on the outlet part of boundary. The domain represents the stenotic aortic valve where the flow starts at the circular inlet of diameter $0.024\,\text{m}$, then it is narrowed up to the diameter $0.012\,\text{m}$ and extended to the diameter $0.036\,\text{m}$. This results in the recirculation within the domain and, due to the short length of the geometry ($0.044\,\text{m}$), the recirculation on the outlet. This was solved using the backflow stabilization to prevent numerical instabilities. It was shown than the flow was highly different in slip case than in no-slip case, namely vortices were bigger with higher velocity in slip case. This can be also due to the velocity profile (constant flow in slip case in opposite to the parabolic profile in noslip case) and the shape of the domain. Then the energy dissipation was higher in slip case in stenotic valve geometry (but not in non-stenotic valve geometry).

The other contribution of this chapter was the computation of the surface integrals arising from the reformulation of Navier-Stokes equations in section 3.2. The conclusion was that the integral $\int_{\partial\Omega} \frac{\rho_*}{2}|\mathbf{v}|^2 (\mathbf{v}\cdot\mathbf{n})\, dS$ is not negligible next to the integrals appearing in Bernoulli equation (5.18).

Conclusion

We have studied the flows of incompressible Newtonian fluid in geometries relevant to biomechanical applications. All computations provided in the thesis were time-dependent and three-dimensional. The specification of the biomechanical modelling is patient-specific geometry, high velocity magnitudes in opposite to small diameters of the tubes, non-symmetry of the problems and inaccuracies in the data. The thesis incorporates all these topics in context of two biomechanical applications, flow in cerebral aneurysms and flow in stenotic valves.

The thesis can be divided in two bigger parts. The first part, presented in chapters 1 and 2, provides the introduction to the modelling flow in cerebral arteries, forming in Willis circles, affected by the aneurysm. The process of obtaining the computational meshes from medical imaging techniques was described and the meshes were used to get the distribution of velocity field, normal pressure and wall shear stress (WSS). The numerical model using the finite element method and Crank-Nicholson time discretization scheme was presented and tested against numerical benchmark. The study concerning a ruptured aneurysm with two inflows were also presented and the hemodynamic parameters were compared in the point of rupture. The main result of the chapter was concerned to the computation of hemodynamic parameters in twenty aneurysms located in middle cerebral artery. It was shown that the size of the aneurysm has more important role in WSS distribution than the aneurysm rupture status. The suggested approach was to compare volume matched pairs of ruptured and unruptured aneurysms.

There are three softwares used in the thesis, namely Fstrin, academic software developed by M. Mádlík in Charles University (Hron and Mádlík, 2007; Mádlík, 2010) and used in sections 2.4 and 2.5, Fluent 16.1 (ANSYS, Inc, Canonsburg PA), commercial software used in section 2.6 and FEniCS (Logg et al., 2012), opensource software for solving partial differential equations by finite element method, used in chapters 3-5.

The attention was also paid to the current methods of treatment for both applications, diagnostic of the aneurysm rupture potential and the stenosis evaluation. In the thesis we tried to have mathematical notation consistent in all chapters and to explain all the medical terms and abbreviations by providing schemes and figures. Sometimes using the non-medical terminology was inevitable. To obtain more medical background with more precise medical terms, we refer to the articles mentioned in the Introduction where doctors provided medical background.

In the second part of the thesis we studied the flow in stenotic valves as presented in chapters 3−5. In chapter 3, the focus is on the flow in highly narrowed tubes. We briefly recalled the models currently used in clinical practice and show their limitations by presenting the assumptions involved in the derivation of Bernoulli's type equations. We

documented that these approaches are in fact very limited and provided minimal piece of information to real flow in aortic valves. We then presented the full time-dependent Newtonian model, using realistic three-dimensional geometry and physiologically relevant boundary conditions. The problem is challenging due to the high pressure on the outlet changing in time and short geometry resulting in the recirculation on the outflow boundary. The major improvement consists of boundary condition controling the recirculation of the flow on the outlet as analyzed in (Braack and Mucha, 2014) in theoretical study and used in (Bertoglio and Caiazzo, 2014). In this chapter it was shown that the methods based on Bernoulli equation give totally different pressure difference values than full continuum mechanics model. This was shown in section 3.2 and approved by numerical results in section 3.5 and also in section 5.3.

The chapter 4 is devoted to the backward problem, obtaining the pressure data directly from the velocity field. We presented the method which provides more accurate pressure approximation than commonly used Pressure Poisson Equation. This was tested in idealized geometries with symmetric and non-symmetric stenosis and also on patient-specific geometry of cerebral aneurysm. The velocity field was considered to be known in limited amount of points in geometry and all velocity vectors were modified to be affected by the error up to 10%. The fact that data are measured with error should be more precisely treated by stochastic methods, i.e. stochastic finite element method, where measured quantity is represented as a random field. But these approaches lead to much more complicated and larger problems than the one solved in the thesis.

Finally, we have presented the Nitsche's method for treating free-slip boundary condition on time dependent three-dimensional flow in narrowed pipe in chapter 5. The main result is concerned to comparison of no-slip boundary condition prescribed on the walls with free-slip boundary condition, which is provided on the geometries representing stenotic valves up to 50% narrowing. We have shown that differences between the no-slip and free-slip boundary condition prescribed on the walls might be remarkable. We would like to say that for blood flow in arteries it is common to suppose no-slip boundary condition on the wall. The study provided in chapter 5 should just provide warning that the different boundary conditions can lead to very different results.

Bibliography

Akins, C. W., Travis, B., and Yoganathan, A. P. (2008). Energy loss for evaluating heart valve performance. *The Journal of Thoracic and Cardiovascular Surgery*, 136(4):820–833.

Arnold, D. N., Brezzi, F., and Fortin, M. (1984). A stable finite element for the Stokes equations. *Calcolo*, 21(4):337–344.

Babuška, I. (1973). The finite element method with Lagrangian multipliers. *Numerische Mathematik*, 20(3):179–192.

Bade, R., Haase, J., and Preim, B. (2006). Comparison of fundamental mesh smoothing algorithms for medical surface models. In *In Simulation und Visualisierung*, pages 289–304.

Barbosa, H. J. and Hughes, T. J. (1991). The finite element method with Lagrange multipliers on the boundary: circumventing the BabuškaBrezzi condition. *Comput. Methods Appl. Mech. Eng.*, 85(1):109–128.

Baumgartner, H., Hung, J., Bermejo, J., Chambers, J. B., Evangelista, A., Griffin, B. P., Iung, B., Otto, C. M., Pellikka, P. A., and Quinones, M. (2009). Echocardiographic assessment of valve stenosis: EAE/ASE recommendations for clinical practice. *European Journal of Echocardiography*, 10(1):1–25.

Benk, J., Ulbrich, M., and Mehl, M. (2012). The Nitsche Method of the Navier-Stokes Equations for Immersed and Moving Boundaries. In *Seventh International Conference on Computational Fluid Dynamics*.

Bennett, L. (1967). Red cell slip at a wail in vitro. *Science*, 155(3769):1554–1556.

Berg, P., Roloff, C., Beuing, O., Voss, S., Sugiyama, S.-I., Aristokleous, N., Anayiotos, A. S., Ashton, N., Revell, A., Bressloff, N. W., Brown, A. G., Chung, B. J., Cebral, J. R., Copelli, G., Fu, W., Qiao, A., Geers, A. J., Hodis, S., Dragomir-Daescu, D., Nordahl, E., Suzen, Y. B., Khan, M. O., Valen-Sendstad, K., Kono, K., Menon, P. G., Albal, P. G., Mierka, O., Münster, R., Morales, H. G., Bonnefous, O., Osman, J., Goubergrits, L., Pallares, J., Cito, S., Passalacqua, A., Piskin, S., Pekkan, K., Ramalho, S., Marques, N., Sanchi, S., Schumacher, K. R., Sturgeon, J., Švihlová, H., Hron, J., Usera, G., Mendina, M., Xiang, J., Meng, H., Steinman, D. A., and Janiga, G. (2015). The Computational Fluid Dynamics Rupture Challenge 2013—Phase II: Variability of Hemodynamic Simulations in Two Intracranial Aneurysms. *Journal of Biomechanical Engineering*, 137(12):121008.

Berger, M., Berdoff, R. L., Gallerstein, P. E., and Goldberg, E. (1984). Evaluation of aortic stenosis by continuous wave Doppler ultrasound. *Journal of the American College of Cardiology*, 3(1):150–156.

Bertoglio, C. (2012). Forward and Inverse Problems in Fluid-Structure Interaction. Application to Hemodynamics. PhD. Thesis, Universit Pierre et Marie Curie-Paris VI, Paris.

Bertoglio, C. and Caiazzo, A. (2014). A tangential regularization method for backflow stabilization in hemodynamics. *Journal of Computational Physics*, 261:162–171.

Bolin, C. D. and Raguin, L. G. (2008). Methodology to estimate the relative pressure field from noisy experimental velocity data. *Journal of Physics: Conference Series*.

Braack, M. and Mucha, P. B. (2014). Directional Do-Nothing Condition for the Navier-Stokes Equations. *Journal of Computational Mathematics*, 32(5):507–521.

Bugliarello, G. and Hayden, J. W. (1963). Detailed characteristics of the flow of blood in vitro. *Transactions of the Society of Rheology*, 7(1):209–230.

Burwash, I. G., Forbes, A. D., Sadahiro, M., Verrier, E. D., Pearlman, A. S., Thomas, R., Kraft, C., and Otto, C. M. (1993). Echocardiographic volume flow and stenosis severity measures with changing flow rate in aortic stenosis. *American Journal of Physiology - Heart and Circulatory Physiology*, 265(5):H1734–H1743.

Cayco, M. E. and Nicolaides, R. A. (1986). Finite Element Technique for Optimal Pressure Recovery from Stream Function Formulation of Viscous Flows. *Mathematics of Computation*, 46(174):371.

Cebral, J. R. and Meng, H. (2012). Counterpoint: Realizing the Clinical Utility of Computational Fluid Dynamics–Closing the Gap. *American Journal of Neuroradiology*, 33(3):396–398.

Cebral, J. R., Mut, F., Weir, J., and Putman, C. (2010). Quantitative Characterization of the Hemodynamic Environment in Ruptured and Unruptured Brain Aneurysms. *American Journal of Neuroradiology*.

Cebral, J. R., Pergolizzi, R. S., and Putman, C. M. (2007). Computational Fluid Dynamics Modeling of Intracranial Aneurysms. *Academic Radiology*, 14(7):804–813.

Challenge (2013). *http : //www.uni − magdeburg.de/isut/LSS/CFD/CFD_Challenge. html*.

Charonko, J. J., King, C. V., Smith, B. L., and Vlachos, P. P. (2010). Assessment of pressure field calculations from particle image velocimetry measurements. *Measurement Science and Technology*.

Chien, A., Tateshima, S., Sayre, J., Castro, M., Cebral, J., and Viñuela, F. (2009). Patient-specific hemodynamic analysis of small internal carotid artery-ophthalmic artery aneurysms. *Surgical Neurology*, 72(5):444–450.

Chien, S., Usami, S., Taylor, H. M., Lundberg, J. L., and Gregersen, M. I. (1966). Effects of hematocrit and plasma proteins on human blood rheology at low shear rates. *Journal of Applied Physiology*, 21(1):81–87.

Ciarlet, P. G. (2002). *The Finite Element Method for Elliptic Problems (Classics in Applied Mathematics)*. SIAM: Society for Industrial and Applied Mathematics.

Currie, P. J., Seward, J. B., Reeder, G. S., Vlietstra, R. E., Bresnahan, D. R., Bresnahan, J. F., Smith, H. C., Hagler, D. J., and Tajik, A. J. (1985). Continuous-wave Doppler echocardiographic assessment of severity of calcific aortic stenosis: a simultaneous Doppler-catheter correlative study in 100 adult patients. *Circulation*, 71(6):1162–1169.

Dabiri, J. O., Bose, S., Gemmell, B. J., Colin, S. P., and Costello, J. H. (2014). An algorithm to estimate unsteady and quasi-steady pressure fields from velocity field measurements. *The Journal of Experimental Biology*, 217(3):331–336.

Dasi, L. P., Simon, H. A., Sucosky, P., and Yoganathan, A. P. (2009). Fluid Mechanics of Artificial Heart Valves. *Clinical and Experimental Pharmacology and Physiology*, 36(2):225–237.

Dhar, S., Tremmel, M., Mocco, J., Kim, M., Yamamoto, J., Siddiqui, A. H., Hopkins, L. N., and Meng, H. (2008). Morphology parameters for intracranial aneurysm rupture risk assessment. *Neurosurgery*, 63(2):185–197.

Dintenfass, L. (1985). *Blood Viscosity*. Springer.

Duan, G., Lv, N., Yin, J., Xu, J., Hong, B., Xu, Y., Liu, J., and Huang, Q. (2014). Morphological and hemodynamic analysis of posterior communicating artery aneurysms prone to rupture: a matched case–control study. *Journal of NeuroInterventional Surgery*, 8(1):47–51.

Fang, Q. and Boas, D. A. (2009). Tetrahedral mesh generation from volumetric binary and grayscale images. In *2009 IEEE International Symposium on Biomedical Imaging: From Nano to Macro*. Institute of Electrical and Electronics Engineers (IEEE).

Fischer, J. L., Haberer, T., Dickson, D., and Henselmann, L. (1995). Comparison of Doppler echocardiographic methods with heart catheterisation in assessing aortic valve area in 100 patients with aortic stenosis. *Heart*, 73(3):293–298.

Freund, J. and Stenberg, R. (1995). On weakly imposed boundary conditions for second order problems. In *Morandi Cecchi, M. (Ed.), Proceedings of the Ninth Int. Conf. Finite Elements in Fluids, Venice.*, pages 327–336.

Fukazawa, K., Ishida, F., Umeda, Y., Miura, Y., Shimosaka, S., Matsushima, S., Taki, W., and Suzuki, H. (2013). Using Computational Fluid Dynamics Analysis to Characterize

Local Hemodynamic Features of Middle Cerebral Artery Aneurysm Rupture Points. *World Neurosurgery*, 83(1):80–86.

Garcia, D., Kadem, L., Savéry, D., Pibarot, P., and Durand, L. (2006). Analytical modeling of the instantaneous maximal transvalvular pressure gradient in aortic stenosis. *Journal of Biomechanics*, 39(16):3036–3044.

Gorlin, R. and Gorlin, S. (1951). Hydraulic formula for calculation of the area of the stenotic mitral valve, other cardiac valves, and central circulatory shunts. I. *American Heart Journal*, 41(1):1–29.

Goubergrits, L., Schaller, J., Kertzscher, U., van den Bruck, N., Poethkow, K., Petz, C., Hege, H.-C., and Spuler, A. (2011). Statistical wall shear stress maps of ruptured and unruptured middle cerebral artery aneurysms. *Journal of The Royal Society Interface*, 9(69):677–688.

Guermond, J. L., Minev, P., and Shen, J. (2006). An overview of projection methods for incompressible flows. *Computer Methods in Applied Mechanics and Engineering*, 195(44-47):6011–6045.

Gurka, R., Liberzon, A., Hefetz, D., and Rubinstein, D. (1999). Computation of pressure distribution using PIV velocity data. In *Proceedings of the 3rd international workshop on particle image velocimetry—PIV'99*.

Gurtin, M. (1982). *An Introduction to Continuum Mechanics (Mathematics in Science and Engineering(158))*. Academic Press.

Hakki, A. H., Iskandrian, A. S., Bemis, C. E., Kimbiris, D., Mintz, G. S., Segal, B. L., and Brice, C. (1981). A simplified valve formula for the calculation of stenotic cardiac valve areas. *Circulation*, 63(5):1050–1055.

Hansen, C. D. and Johnson, C. R. (2011). *Visualization Handbook*. Academic Press.

Hatle, L., Brubakk, A., Tromsdal, A., and Angelsen, B. (1978). Noninvasive assessment of pressure drop in mitral stenosis by Doppler ultrasound. *Heart*, 40(2):131–140.

He, X. (1996). Pulsatile Flow in the Human Left Coronary Artery Bifurcation: Average Conditions. *Journal of Biomechanical Engineering*, 118(1):74.

Hejčl, A., Švihlová, H., Radovnický, T., Sejkorová, A., Adámek, D., Hron, J., Dragomir-Daescu, D., and Sameš, M. (2017). Computational fluid dynamics of a fatal ruptured anterior communicating artery aneurysm a case report. *Journal of Neurological Surgery Part A*. submitted.

Heys, J. J., Manteuffel, T. A., McCormick, S. F., Milano, M., Westerdale, J., and Belohlavek, M. (2010). Weighted least-squares finite elements based on particle imaging velocimetry data. *Journal of Computational Physics*, 229(1):107–118.

Himburg, H. A. (2004). Spatial comparison between wall shear stress measures and porcine arterial endothelial permeability. *AJP: Heart and Circulatory Physiology*, 286(5):H1916–H1922.

Hippelheuser, J. E., Lauric, A., Cohen, A. D., and Malek, A. M. (2014). Realistic non-Newtonian viscosity modelling highlights hemodynamic differences between intracranial aneurysms with and without surface blebs. *Journal of Biomechanics*, 47(15):3695–3703.

Hodis, S., Uthamaraj, S., Lanzino, G., Kallmes, D. F., and Dragomir-Daescu, D. (2013). Computational fluid dynamics simulation of an anterior communicating artery ruptured during angiography. *Case Reports*, 2013(1):bcr–2012–010596—bcr–2012–010596.

Hron, J. and Mádlík, M. (2007). Fluid-structure interaction with applications in biomechanics. *Nonlinear Analysis: Real World Applications*, 8(5):1431–1458.

Hron, J., Roux, C. L., Málek, J., and Rajagopal, K. (2008). Flows of Incompressible Fluids subject to Navier's slip on the boundary. *Computers & Mathematics with Applications*, 56(8):2128–2143.

Janiga, G., Berg, P., Sugiyama, S., Kono, K., and Steinman, D. A. (2014). The computational fluid dynamics rupture challenge 2013–phase i: Prediction of rupture status in intracranial aneurysms. *American Journal of Neuroradiology*, 36(3):530–536.

Jou, L.-D., Lee, D., Morsi, H., and Mawad, M. (2008). Wall Shear Stress on Ruptured and Unruptured Intracranial Aneurysms at the Internal Carotid Artery. *American Journal of Neuroradiology*, 29(9):1761–1767.

Jovanović, J. D. and Jovanović, M. L. (2010). Finite element modeling of the vertebra with geometry and material properties retrieved from CT-scan data. *Facta Universitatis, Series: Mechanical Engineering*, 8(1):19–26.

Juntunen, M. (2015). On the connection between the stabilized Lagrange multiplier and Nitscheś methods. *Numerische Mathematik*, 131(3):453–471.

Kosturakis, D., Goldberg, S. J., Allen, H. D., and Loeber, C. (1984). Doppler echocardiographic prediction of pulmonary arterial hypertension in congenital heart disease. *The American Journal of Cardiology*, 53(8):1110–1115.

Krittian, S. B. S., Lamata, P., Michler, C., Nordsletten, D. A., Bock, J., Bradley, C. P., Pitcher, A., Kilner, P. J., Markl, M., and Smith, N. P. (2012). A finite-element approach to the direct computation of relative cardiovascular pressure from time-resolved MR velocity data. *Medical Image Analysis*.

Ku, D. N., Giddens, D. P., Zarins, C. K., and Glagov, S. (1985). Pulsatile flow and atherosclerosis in the human carotid bifurcation. Positive correlation between plaque location and low oscillating shear stress. *Arteriosclerosis, Thrombosis, and Vascular Biology*, 5(3):293–302.

Kumar, D., Vinoth, R., Adhikari, R., and Shankar, C. S. V. (2017). Non-newtonian and newtonian blood flow in human aorta: A transient analysis. *Biomedical Research*, 28(7):3194–3203.

Lauric, A., Hippelheuser, J., Cohen, A. D., Kadasi, L. M., and Malek, A. M. (2013). Wall shear stress association with rupture status in volume matched sidewall aneurysms. *Journal of NeuroInterventional Surgery*, 6(6):466–473.

Liu, J., Xiang, J., Zhang, Y., Wang, Y., Li, H., Meng, H., and Yang, X. (2013). Morphologic and hemodynamic analysis of paraclinoid aneurysms: ruptured versus unruptured. *Journal of NeuroInterventional Surgery*, 6(9):658–663.

Liu, J.-G., Liu, J., and Pego, R. L. (2010). Stable and accurate pressure approximation for unsteady incompressible viscous flow. *Journal of Computational Physics*, 229(9):3428–3453.

Logg, A., Mardal, K. A., and Wells, G. N., editors (2012). *Automated Solution of Differential Equations by the Finite Element Method*, volume 84 of *Lecture Notes in Computational Science and Engineering*. Springer Berlin Heidelberg.

Lu, G., Huang, L., Zhang, X. L., Wang, S. Z., Hong, Y., Hu, Z., and Geng, D. Y. (2011). Influence of Hemodynamic Factors on Rupture of Intracranial Aneurysms: Patient-Specific 3D Mirror Aneurysms Model Computational Fluid Dynamics Simulation. *American Journal of Neuroradiology*, 32(7):1255–1261.

Maceira, A., Prasad, S., Khan, M., and Pennell, D. (2006). Normalized left ventricular systolic and diastolic function by steady state free precession cardiovascular magnetic resonance. *Journal of Cardiovascular Magnetic Resonance*, 8(3):417–426.

Mádlík, M. (2010). Interactions of a Fluid Flow with an Elastic Body. PhD. Thesis, Charles University, Prague.

Maria Denaro, F. (2003). On the application of the Helmholtz-Hodge decomposition in projection methods for incompressible flows with general boundary conditions. *International Journal for Numerical Methods in Fluids*, 43(1):43–69.

MedicineNet, Inc. (2017). Aortic valve stenosis. `http://www.medicinenet.com/aortic_stenosis/article.htm`.

Mekhlouf, R., Baggag, A., and Remaki, L. (2016). Assessment of Nitsches Method for Dirichlet Boundary Conditions Treatment. In *Proceedings of the 3rd International Conference on Fluid Flow, Heat and Mass Transfer (FFHMT'16).*, volume 176.

Meng, H., Tutino, V. M., Xiang, J., and Siddiqui, A. (2013). High WSS or Low WSS? Complex Interactions of Hemodynamics with Intracranial Aneurysm Initiation, Growth, and Rupture: Toward a Unifying Hypothesis. *American Journal of Neuroradiology*, 35(7):1254–1262.

Metaxa, E., Tremmel, M., Xiang, J., Kolega, J., Mandelbaum, M., Siddiqui, A., Mocco, J., and Meng, H. (2009). High Wall Shear Stress and Positive Wall Shear Stress Gradient Trigger the Initiation of Intracranial Aneurysms. In *ASME 2009 Summer Bioengineering Conference, Parts A and B*. ASME International.

Miura, Y., Ishida, F., Umeda, Y., Tanemura, H., Suzuki, H., Matsushima, S., Shimosaka, S., and Taki, W. (2012). Low Wall Shear Stress Is Independently Associated With the Rupture Status of Middle Cerebral Artery Aneurysms. *Stroke*, 44(2):519–521.

Mut, F., Raschi, M., Scrivano, E., Bleise, C., Chudyk, J., Ceratto, R., Lylyk, P., and Cebral, J. R. (2014). Association between hemodynamic conditions and occlusion times after flow diversion in cerebral aneurysms. *Journal of NeuroInterventional Surgery*, 7(4):286–290.

Naito, T., Miyachi, S., Matsubara, N., Isoda, H., Izumi, T., Haraguchi, K., Takahashi, I., Ishii, K., and Wakabayashi, T. (2012). Magnetic resonance fluid dynamics for intracranial aneurysms—comparison with computed fluid dynamics. *Acta Neurochir*, 154(6):993–1001.

Nitsche, J. A. (1971). Über ein Variationsprinzip zur Lösung von Dirichlet-Problemen bei Verwendung von Teilräiumen, die keinen Randbedingungen unterworfen sind. *Abhandlungen aus dem Mathematischen Seminar der Universität Hamburg*, 36:9–15.

Nubar, Y. (1971). Blood flow, slip, and viscometry. *Biophysical Journal*, 11(3):252–264.

Prohl, A. (2008). On pressure approximation via projection methods for nonstationary incompressible Navier-Stokes equations. *SIAM Journal of Numerical Analysis*, 47(1):158–180.

Qi, S., Li, Z., Yue, Y., van Triest, H. J., and Kang, Y. (2014). Computational fluid dynamics simulation of airflow in the trachea and main bronchi for the subjects with left pulmonary artery sling. *BioMedical Engineering OnLine*, 13(1):85.

Qian, Y., Takao, H., Umezu, M., and Murayama, Y. (2011). Risk Analysis of Unruptured Aneurysms Using Computational Fluid Dynamics Technology: Preliminary Results. *American Journal of Neuroradiology*, 32(10):1948–1955.

Rebergen, S. A., van der Wall, E. E., Doornbos, J., and de Roos, A. (1993). Magnetic resonance measurement of velocity and flow: Technique, validation, and cardiovascular applications. *American Heart Journal*, 126(6):1439–1456.

Richter, T. (2015). A monolithic geometric multigrid solver for fluid-structure interactions in ALE formulation. *International Journal for Numerical Methods in Engineering*, 104(5):372–390.

Rinkel, G. J., Djibuti, M., Algra, A., and van Gijn, J. (1998). Prevalence and risk of rupture of intracranial aneurysms: a systematic review. *Stroke*, 29(1):251–256.

Sejkorová, A., Dennis, K. D., Švihlová, H., Petr, O., Lanzino, G., Hejčl, A., and Dragomir-Daescu, D. (2016). Hemodynamic changes in a middle cerebral artery aneurysm at follow-up times before and after its rupture: a case report and a review of the literature. *Neurosurgical Review*, 40(2):329–338.

Shirokoff, D. and Rosales, R. R. (2011). An efficient method for the incompressible Navier–Stokes equations on irregular domains with no-slip boundary conditions, high order up to the boundary. *Journal of Computational Physics*, 230(23):8619–8646.

Shojima, M., Oshima, M., Takagi, K., Torii, R., Hayakawa, M., Katada, K., Morita, A., and Kirino, T. (2004). Magnitude and Role of Wall Shear Stress on Cerebral Aneurysm: Computational Fluid Dynamic Study of 20 Middle Cerebral Artery Aneurysms. *Stroke*, 35(11):2500–2505.

Smith, M. D., Kwan, O. L., and DeMaria, A. N. (1986). Value and limitations of continuous-wave Doppler echocardiography in estimating severity of valvular stenosis. *JAMA*, 255(22):3145–3151.

Song, S. M., Leahy, R. M., Boyd, D. P., Brundage, B. H., and Napel, S. (1994). Determining cardiac velocity fields and intraventricular pressure distribution from a sequence of ultrafast CT cardiac images. *IEEE Transactions on Medical Imaging*, 13(2):386–397.

Stenberg, R. (1995). On some techniques for approximating boundary conditions in the finite element method. *Journal of Computational and Applied Mathematics*, 63(1-3):139–148.

Sugiyama, S., Niizuma, K., Nakayama, T., Shimizu, H., Endo, H., Inoue, T., Fujimura, M., Ohta, M., Takahashi, A., and Tominaga, T. (2013). Relative Residence Time Prolongation in Intracranial Aneurysms. *Neurosurgery*, 73(5):767–776.

Švihlová, H. (2013). Aplikace metody konečných prvků na reálné problémy v hemodynamice. Master thesis, Charles University, Prague.

Švihlová, H., Hron, J., Málek, J., Rajagopal, K. R., and Rajagopal, K. (2016). Determination of pressure data from velocity data with a view toward its application in cardiovascular mechanics. Part 1. Theoretical considerations. *International Journal of Engineering Science*, 105:108–127.

Švihlová, H., Hron, J., Málek, J., Rajagopal, K. R., and Rajagopal, K. (2017). Determination of pressure data from velocity data with a view towards its application in cardiovascular mechanics. Part 2: A study of aortic valve stenosis. *International Journal of Engineering Science*, 113:37–50.

Takao, H., Murayama, Y., Otsuka, S., Qian, Y., Mohamed, A., Masuda, S., Yamamoto, M., and Abe, T. (2012). Hemodynamic Differences Between Unruptured and Ruptured Intracranial Aneurysms During Observation. *Stroke*, 43(5):1436–1439.

Tanoue, T., Tateshima, S., Villablanca, J. P., Vinuela, F., and Tanishita, K. (2011). Wall Shear Stress Distribution Inside Growing Cerebral Aneurysm. *American Journal of Neuroradiology*, 32(9):1732–1737.

The CGAL Project (2016). *CGAL User and Reference Manual*. CGAL Editorial Board, 4.9 edition.

Thurston, G. (1979). Rheological parameters for the viscosity viscoelasticity and thixotropy of blood. *Biorheology*, 16(3):149 – 162.

Warth, D. C., Stewart, W. J., Block, P. C., and Weyman, A. E. (1984). A new method to calculate aortic valve area without left heart catheterization. *Circulation*, 70(6):978–983.

Wikipedia (2017a). Cardiac cycle. `https://upload.wikimedia.org/wikipedia/commons/9/9a/Wiggers_Diagram.png`.

Wikipedia (2017b). Circle of willis. `https://en.wikipedia.org/wiki/Circle_of_Willis`.

Womersley, J. R. (1955). Method for the calculation of velocity, rate of flow and viscous drag in arteries when the pressure gradient is known. *The Journal of Physiology*, 127(3):553–563.

Woodcock, J. P. (1976). Physical properties of blood and their influence on blood-flow *Reports on Progress in Physics*, 39(1):65.

Xiang, J., Tremmel, M., Kolega, J., Levy, E. I., Natarajan, S. K., and Meng, H. (2011). Newtonian viscosity model could overestimate wall shear stress in intracranial aneurysm domes and underestimate rupture risk. *Journal of NeuroInterventional Surgery*, 4(5):351–357.

Yang, G.-Z., Kilner, P. J., Wood, N. B., Underwood, S. R., and Firmin, D. N. (1996). Computation of flow pressure fields from magnetic resonance velocity mapping. *Magnetic Resonance in Medicine*, 36(4):520–526.

Yeleswarapu, K., Kameneva, M., Rajagopal, K., and Antaki, J. (1998). The flow of blood in tubes: theory and experiment. *Mechanics Research Communications*, 25(3):257 – 262.

Yushkevich, P. A., Piven, J., Hazlett, H. C., Smith, R. G., Ho, S., Gee, J. C., and Gerig, G. (2006). User-guided 3d active contour segmentation of anatomical structures: Significantly improved efficiency and reliability. *NeuroImage*, 31(3):1116–1128.

Zamir, M. (2005). The Analysis of Composite Waveforms. In *The Physics of Coronary Blood Flow*, pages 145–175. Springer Nature.

Zhang, Y., Yang, X., Wang, Y., Liu, J., Li, C., Jing, L., Wang, S., and Li, H. (2014). Influence of morphology and hemodynamic factors on rupture of multiple intracranial aneurysms: matched-pairs of ruptured-unruptured aneurysms located unilaterally on the anterior circulation. *BMC Neurology*, 14(1).

List of Figures

List of Tables